

DETERMINING FORMATIVE WINDS THROUGH
GEOMORPHOLOGY: HERSCHEL CRATER,
MARS

By

CHRISTOPHER TERRY ADCOCK

Bachelor of Science

University of New Mexico

Albuquerque, New Mexico

1995

Submitted to the Faculty of the
Graduate College of the
Oklahoma State University
in partial fulfillment of
the requirements for
the Degree of
MASTER OF SCIENCE
December, 2004

DETERMINING FORMATIVE WINDS THROUGH
GEOMORPHOLOGY: HERSCHEL CRATER,
MARS

Thesis Approved:

Dr. Richard A. Marston

Dr. Richard A. Marston, Sun Chair Professor,
School of Geology. Thesis Advisor

Dr. Stanley T. Paxton

Dr. Stanley T. Paxton, Assistant Professor,
School of Geology.

Dr. Elizabeth J. Catlos

Dr. Elizabeth J. Catlos, Assistant Professor,
School of Geology.

Dr. Stephen J. Stadler

Dr. Stephen J. Stadler, Professor, Department of Geography.
State Geographer of Oklahoma.

Dr. A. Gordon Emslie

Dean of the Graduate College

ACKNOWLEDGEMENTS

Documents like this often give the impression that the work was a solo effort, when in fact a broad group of people are involved. I would like to thank my committee members for their time and support. Dr. Richard Marston always had a moment to answer a question or point me in the right direction. His lessons in geomorphology taught me that sometimes we allow the rocks to hide the mountain and stepping back from the hand lens can be very illuminating. Dr. Elizabeth Catlos inspired me to ask questions not only of those around me, but of myself. She then proceeded to provide people, such as Karen McBride and John Rummel of NASA, to question. Dr. Stanley Paxton took a genuine interest not only in my work but of Mars in general. Our discussions about the latest Mars images kept my often wandering mind focused on Mars – if not always exactly on my own project.

One member of my committee is not from my home department. I am honored to have Dr. Stephen Stadler from the Geography Department on my committee. I believe the future of science lies in interdisciplinary research. For too long the disciplines of science have focused on what separates them. A regret of mine is that the actual physical separation of our departments meant our discussions were too few. However, he was always available when I knocked on his door.

Dr. Denise Tillery, my soon to be wife, not only financed my first semester, but has kept a roof over our heads while I have been in school. I am sure there are few tasks harder than living with me while I have been in graduate school and she deserves praise. My parents, Larry and Terri Adcock, called nearly every week and always showed interest in my progress – both in school and in life in general.

I am blessed to have received a number of awards during my graduate study. I am most proud of being awarded the Rumsey Bissell Marston Scholarship which is given in the spirit of education and in honor of a lifetime educator. I also received an Oklahoma Space Grant Consortium NASA Fellowship which helped offset the cost of attending conferences and my attendance to the 2004 JPL Planetary Science Summer School. This allowed me to keep my planetary science views well rounded. Additionally, I received assistantship from the Department of English, the School of Geology, and the Arkansas-Oklahoma Center for Space and Planetary Sciences.

Finally I would like to mention a few more people or groups: Ben Stanley, Christopher Neel, Dale Splinter, Ogus Gogus, Lori Fenton, the late Grant Fowler, Dr. Peter Shull, Dr. Andrew Arena, Dr. Maya Elrick, Jim Connelly, Mike Spilde, Dr. Chip Shearer, The Sandia National Labs at California's electron microscopy group, The folks of the former Colorado Minerals Research Institute, my friends at the Institute of Meteoritics and all my friends in the School of Geology. I am sure the list is not complete and I apologize to those I have failed to mention.

TABLE OF CONTENTS

Chapter	Page
I. INTRODUCTION	1
PROBLEM STATEMENT AND SIGNIFICANCE	1
PURPOSE AND OBJECTIVES	3
STUDY AREA	3
II. LITERATURE REVIEW.....	8
DETERMINING WIND DIRECTION FROM EOLIAN FEATURES	8
MARTIAN EOLIAN STUDIES.....	24
GENERAL CIRCULATION MODELS.....	33
III. METHODOLOGY	35
DATA ACQUISITION	35
Image Data	35
Circulation Model Data.....	36
DATA INTERPRETATION	37
Map Generation and Wind Determinations	37
Changes in Eolian Features Over Time	39
General Circulation Comparisons.....	40
IV. RESULTS AND DISCUSSION.....	42
EOLIAN LANDFORMS CATALOG.....	42
MAP GENERATION AND WIND DETERMINATIONS	42
CHANGES IN EOLIAN FEATURES OVER TIME	45
GENERAL CIRCULATION COMPARISONS	47
V. CONCLUSIONS.....	49
USEFULNESS OF EOLIAN FEATURES IMAGES FOR INFERRING WIND DIRECTION	49
GENERAL CIRCULATION COMPARISONS	49
FUTURE WORK	50
REFERENCES	52
APPENDIX A – MOC NA IMAGES USED	56
APPENDIX B – DIRECTIONAL DATA FROM IMAGES	110
APPENDIX C - ANNOTATED MSSS MOC NA IMAGES.....	125

LIST OF TABLES

Table 1. Visible spectrum camera resolutions of selected missions to Mars showing advancement over time.....	26
Table 2. Data summary including number of measurements, mean wind direction and standard deviation by image analyzed..	45

LIST OF FIGURES

Figure 1. Sand encroachment over a retaining wall of a beach resort. C.T. Adcock image, Las Conchas, Mexico 2004.	2
Figure 2. Power pole in southern California with metal sheath eroded through by abrasion (Greeley and Iversen, 1985, page 10). Original image by R. Greeley, December 1982.....	2
Figure 3. Annotated global map of Mars with selected mission information. PIGWAD base map.....	5
Figure 4. Planetary perspective of Herschel Crater location	6
Figure 5. Cropped Mars Orbital Camera (MOC) image of dune forms in Herschel Crater suitable for inferring wind directions. Field of view is 3 km wide. Original image from Malin Space Science Systems #E0200602.	7
Figure 6. A) A high obliquity aerial photograph of yardangs in the Lut Basin of Iran. B) The region and yardangs as seen in a Landsat image. Landsat field of view is approximately 190 Km. (Walker, 1986).....	10
Figure 7. Diagram showing the three principal modes of eolian transport (Greeley and Iversen, 1985, p. 17).....	11
Figure 8. Sand ripples. Wavelength is approxiamatley 10cm. Formative wind direction was from the right. Image: C. T. Adcock, 2004 Puerto Penasco, Mexico	12
Figure 9. Diagram of ripples in cross section along short axis.....	13
Figure 10. Ripples seen from a Mars Exploration Rover (MER) in Endurance crater, Mars. Image has been contrast enhanced. For scale, the ripple “field” in the image is roughly 30 meters across. Excerpted from Planetary Photojournal image PIA06276 (http://photojournal.jpl.nasa.gov/).....	14

Figure 11. Bright ripples overlain by darker eolian deposits in Herschel Crater. Formative wind direction for the ripples and overlain forms is dissimilar. Excerpted from MSSS MOC NA image R0500941 (http://www.msss.com/moc_gallery).....	14
Figure 12. Diagram of basic dune forms. Modified from (Thomas, 1989, p. 242)	15
Figure 13. Diagram of a barchan dune showing horns, formative wind direction, and slip face apex.....	16
Figure 14. Transformation of a barchan into a linear dune (Bagnold, 1941, p. 223)	18
Figure 15. Diagram of the Tsoar model of seif dune formation (Shao, 2000, p. 331)	18
Figure 16. Transverse component linear dune formation model (Greeley and Iversen, 1985, p. 170)	19
Figure 17. Linear dune formation model utilizing helical flow (Shao, 2000, p. 330).	19
Figure 18. Diagram of a hypothetical star dune and formative wind directions (arrows) in plan form.	22
Figure 19. Cross-section diagram of an echo dune.....	22
Figure 20. Small sand shadows formed behind shell fragments on a beach. Longest is <10 cm long and wind direction is toward the left. C. T. Adcock image Las Conchas, Mexico 2004.....	22
Figure 21. Martian crater streak from the Herschel region. Crater streak is roughly 5 km long. MSSS image E1000272 (http://www.msss.com/moc_gallery).....	23
Figure 22. Threshold friction speeds predicted for planetary bodies including Earth and Mars (Greeley and Iversen, 1985, p. 92)	25
Figure 23. Polar dust streaks on Mars in a MOC NA image. Crater in image is 1.4 km diameter for scale (Diniaga et al., 2003).....	27
Figure 24. Martian dust devil tracks in a MOC NA image. NASA image PIA 02376, Malin Space Science Systems Camera. (Whelley et al., 2003).	28

Figure 25. Screen capture of JMars layer manager showing high resolution MOC NA footprints. For scale, Herschel Crater (centered) is roughly 300 km in diameter.....	36
Figure 26. MSSS MOC NA image M23-0263 (cropped) with dune forms shown. Red arrows indicate predominate wind direction for barchan and barchanoidal ridges.	40
Figure 27. Wind map of Mars on a NASA PDS MDIM1 image of Herschel Crater. Arrows indicate formative wind directions inferred from eolian landforms in this study. Topographic influence on wind direction is evident as wind deflection near the crater rim. Red arrow indicates a determination that does not correspond with the rest of the data and may be localized wind effect.	44
Figure 28. Present-day seasonal average surface winds superimposed on a grayscale MOLA topographic map. Study area is outlined in red with Herschel crater near the center of the box. Diagrams on the right are redrawn to show local GCM predicted wind directions. Modified and redrawn from Fenton, 2003.	48
Figure A-1. SP2-36506 – Traverse north rim of Herschel Crater basin.....	57
Figure A-2. SP2-36507 – Low albedo dunes in Herschel Crater basin.....	58
Figure A-3. FHA-00437 - dark material on Herschel basin floor.....	59
Figure A-4. FHA-00583 - surface immediately north of Herschel Basin rim.....	60
Figure A-5. FHA-00914 - dark floor and central peak in crater on SW rim of Herschel Basin	61
Figure A-6. FHA-01381 - dark material and crater wall within Herschel Basin.....	62
Figure A-7. M00-00790 - Dark floor material within Herschel Basin	63
Figure A-8. M00-03222 - North edge of dark spot in eastern Herschel Crater	64
Figure A-9. M01-03831- Science Campaign A (Geodesy)	65
Figure A-10. M02-00612 - Dark material in Herschel Basin in contact with bright upland.....	66
Figure A-11. M02-01996 - Contact between dark and lighter-toned floor material SE Herschel.....	67

Figure A-12. M02-01998 - Sample terrain immediately N of Herschel rim	68
Figure A-13. M02-02819 - dark material at SW side of Herschel Basin floor.....	69
Figure A-14. M02-03305 - SE wall of Herschel Basin	70
Figure A-15. M03-02054 - Small bright ridges near Herschel	71
Figure A-16. M03-03634 - Traverse across crater rim that looks like small gullied mountain	72
Figure A-17. M04-02035 - Brighter materials in Herschel crater	73
Figure A-18. M04-03624 - dark floor of Herschel	74
Figure A-19. M07-02974 - Dune field in crater on SW rim of Herschel Basin	75
Figure A-20. M07-01919 - Sample dark surface in southeastern Herschel Basin.....	76
Figure A-21. M07-05959 - High resolution traverse across central Herschel Basin floor.....	77
Figure A-22. M08-03208 - Sample terrain along NE Herschel Basin rim	78
Figure A-23. M08-06611 - light/dark margin within Herschel Basin	79
Figure A-24. M09-00699 - North wall of Herschel Basin.....	80
Figure A-25. M10-01789 - Sample terrain off NE rim of Herschel Basin	81
Figure A-26. M11-02107 - Dark dunes on floor of crater adjacent to Herschel Basin	82
Figure A-27. M12-00672 - Rugged peak-ring mountains in E Herschel Basin	83
Figure A-28. M13-00630 - sample	84
Figure A-29. M14-00754 - traverse across cratered upland inside Herschel Basin	85
Figure A-30. M15-01486 - Short deep valley into crater immediately N of Herschel	86
Figure A-31. M18-00644 - Full-resolution sample crater among dark material in Herschel Basin	87
Figure A-32. M19-00489 - sample	88

Figure A-33. M20-01590 – sample.....	89
Figure A-34. M21-00018 - Dark dunes in SW Herschel Basin.....	90
Figure A-35. M22-02419 – sample.....	91
Figure A-36. M23-00263 - Dunes in W Herschel Basin	92
Figure A-37. M23-00825 - Intracrater dune field at 16.5 S 231.8 W	93
Figure A-38. E01-01967 - Herschel Basin survey traverse across west side	94
Figure A-39. E01-02211 - Survey traverse across rugged SE Herschel rim and dark material	95
Figure A-40. E02-00602 - Dunes in Herschel Basin	96
Figure A-41. E02-02816 - Dark material in central Herschel Basin	97
Figure A-42. E09-02803 - Crater survey at 16.7 S231.8W	98
Figure A-43. E09-02804 - Northwestern Herschel Crater floor survey	99
Figure A-44. E10-00272 - Dunes in eastern Herschel Basin.....	100
Figure A-45. E10-01396 - Dark material in eastern Herschel Basin.....	101
Figure A-46. E11-00157 - Dunes in crater on southwest rim of Herschel Basin	102
Figure A-47. E11-00527 - Southeastern floor of Herschel Crater.....	103
Figure A-48. E11-01859 - Dark material in Herschel Basin	104
Figure A-49. E16-01318 - Light material and knobs on Herschel Crater floor.....	105
Figure A-50. R01-01236 - Stereo with M00-03222 Herschel Basin groove- surfaced dunes.....	106
Figure A-51. R03-00358 - Attempt repeat of image M02-00612 dunes in Herschel basin.....	107
Figure A-52. R04-00598 - Dune field in FHA-01381 in crater at 14.4 S 231.5 W	108
Figure A-53. R05-00941 - Grooved dunes in Herschel Basin.....	109
Figure C-1. MSSS MOC NA image SP36507 annotated	126

Figure C-2. MSSS MOC NA image FHA00473 annotated.....	127
Figure C-3. MSSS MOC NA image FHA01381 annotated.....	128
Figure C-4. MSSS MOC NA image M0000790 annotated.....	129
Figure C-5. MSSS MOC NA image M0003228 annotated.....	130
Figure C-6. MSSS MOC NA image M0200612 annotated.....	131
Figure C-7. MSSS MOC NA image M0201996 annotated.....	132
Figure C-8. MSSS MOC NA image M0201998 annotated.....	133
Figure C-9. MSSS MOC NA image M0202819 annotated.....	134
Figure C-10. MSSS MOC NA image M0203305 annotated.....	135
Figure C-11. MSSS MOC NA image M0303634 annotated.....	136
Figure C-12. MSSS MOC NA image M0701919 annotated.....	137
Figure C-13. MSSS MOC NA image M0702974 annotated.....	138
Figure C-14. MSSS MOC NA image M0705959 annotated.....	139
Figure C-15. MSSS MOC NA image M0806611 annotated.....	140
Figure C-16. MSSS MOC NA image M1102107 annotated.....	141
Figure C-17. MSSS MOC NA image M1200672 annotated.....	142
Figure C-18. MSSS MOC NA image M1300630 annotated.....	143
Figure C-19. MSSS MOC NA image M1400754 annotated.....	144
Figure C-20. MSSS MOC NA image M1800644 annotated.....	145
Figure C-21. MSSS MOC NA image M2100018 annotated.....	146
Figure C-22. MSSS MOC NA image M2300263 annotated.....	147
Figure C-23. MSSS MOC NA image M2300825 annotated.....	148
Figure C-24. MSSS MOC NA image E0200602 annotated.....	149

Figure C-25. MSSS MOC NA image E0202816 annotated	150
Figure C-26. MSSS MOC NA image E0902803 annotated	151
Figure C-27. MSSS MOC NA image E1000272 annotated	152
Figure C-28. MSSS MOC NA image E1100527 annotated	153
Figure C-29. MSSS MOC NA image E1101359 annotated	154
Figure C-30. MSSS MOC NA image E1601318 annotated	155
Figure C-31. MSSS MOC NA image R0500941 annotated	156

NOMENCLATURE

GCM	General (Global) Circulation Model(s)
GFDL	General Fluid Dynamic Laboratory
GIS	Geographic Information System
MER	Mars Exploration Rover
MGS	Mars Global Surveyor
MM5	Mesoscale Model 5
MOC	Mars Orbital Camera
MOLA	Mars Orbital Laser Altimeter
MPF	Mars Pathfinder mission
MSSS	Malin Space Science Systems Inc.
NA	Narrow Angle
NASA	National Aeronautics and Space Administration
PDS	Planetary Data System
WA	Wide Angle

CHAPTER I

INTRODUCTION

Problem Statement and Significance

The Viking and Pathfinder landers provide the only direct measurements of surface winds on Mars, and the data collected are limited to mission landing sites. Wind is the dominate geologic process currently at work on the surface of Mars (Greeley and Williams, 1994). An improved understanding of surface winds, even in limited areas, can provide additional data for use in and validation of Global Circulation Models (GCM). A better knowledge of the wind regimes on Mars may provide valuable insight to surface processes on other planetary bodies including Earth. Additionally, this is of significant value to the planning and development of manned and long-term unmanned surface missions to Mars. Problems associated with migrating sand (Figure 1), abrasion (Figure 2), and static buildup and discharge, are well documented on Earth. Winds and the entrained particles within them can have the same detrimental impact on future equipment, structures, and visitors to Mars (Möller et al., 2002; Greeley and Thompson, 2003). The Russian probe *Mars 3*, for example, is thought to have been rendered inoperative by winds it encountered during landing (Sheehan, 1996). On the other hand, if we choose to establish long-term projects on Mars, winds of sufficient strength could be used to generate power for those missions. A comprehensive understanding of Martian surface winds is paramount to our future missions and our ability to understand Mars as a planet.



Figure 1. Sand encroachment over a retaining wall of a beach resort. C.T. Adcock image, Las Conchas, Mexico 2004.

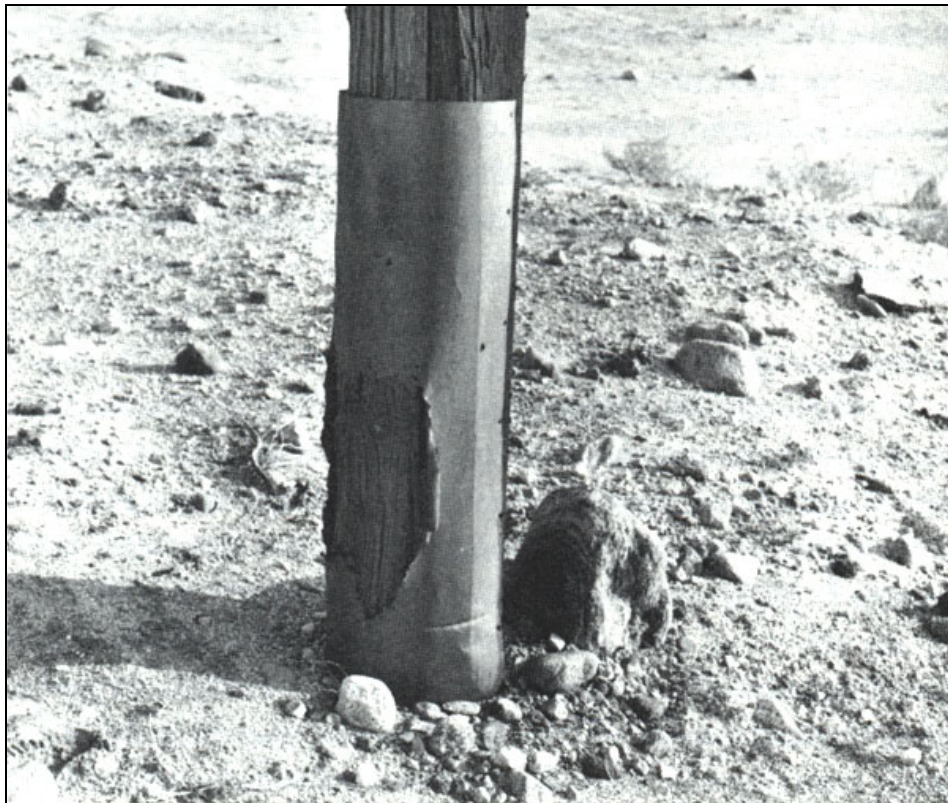


Figure 2. Power pole in southern California with metal sheath eroded through by abrasion (Greeley and Iversen, 1985, page 10). Original image by R. Greeley, December 1982.

Purpose and Objectives

The goal of this study is to characterize the surface winds for a region of Mars by applying known relationships between wind and landforms observed on Earth. To address this purpose, the following objectives were pursued:

1. Identification of eolian (wind made) landforms in the Herschel Crater region of Mars, including wind streaks, dunes and yardangs, found in remotely sensed data.
2. Production of a “wind map” using analogy of terrestrial eolian landforms to infer the direction(s) of formative Martian surface winds at Herschel Crater.
3. Attempt to determine evolution of landforms through time (such as the movement of dunes) at Herschel Crater.
4. Comparison of the compiled wind direction results to an existing computer generated GCM of Martian surface winds (Fenton, 2003).

Study Area

Herschel Crater is a 300 km diameter impact crater located in the southern highlands of Mars east-northeast of Hellas Basin (Figure 3). The Martian coordinate system is similar to Earth’s with the prime meridian running through Terra Meridiani at the equator. Traditionally, longitude increases to the west in the Martian coordinate system (Caplinger and Malin, 2003). Under this coordinate system, Herschel Crater is centered at approximately 230°W. longitude and 15°S. latitude. Some research uses longitude delineated from the east. As a result, Herschel is sometimes noted by

researchers as located at the equivalent 130°E. longitude. The series of insets in Figure 4 give a planetary perspective of the Herschel Crater region.

In regard to age, the interior of Herschel Crater contains material classified as the Ridged Plains unit dating back to the early Hesperian epoch of Mars (Greeley and Guest, 1987). Absolute age models for the unit based on impact flux and lunar data estimate a latest age for emplacement of 3.1 billion years before present (Tanaka et al., 1992). Herschel Crater predates the emplacement of the Ridged Plains unit and as such is older than 3.1 billion years.

The area was chosen for study after a preliminary search of data revealed that at least some high resolution remote sensed imagery of the location contained eolian features, in the form of low albedo dunes, suitable for inferring wind direction. A cropped example of one of these high resolution images is Figure 5. The choice of a crater provides a convenient boundary for the study area, although a few images just beyond the crater rim are examined. In terms of area, Herschel and the nearby surrounding area cover approximately 100,000 km², an area roughly the size of the island of Iceland. This size allows for an area manageable for this research but large enough to make some comparison to previously published general circulation models (GCM). The use of a crater as a study area is not without precedent. Proctor Crater (located at 48°S., 330.5°W.) is the focus of previous similar study (Fenton et al., 2002; Fenton, 2003; Fenton and Bandfield, 2003). The selection of a crater also allows investigation into wind interactions with the topographically significant walls of the rim.

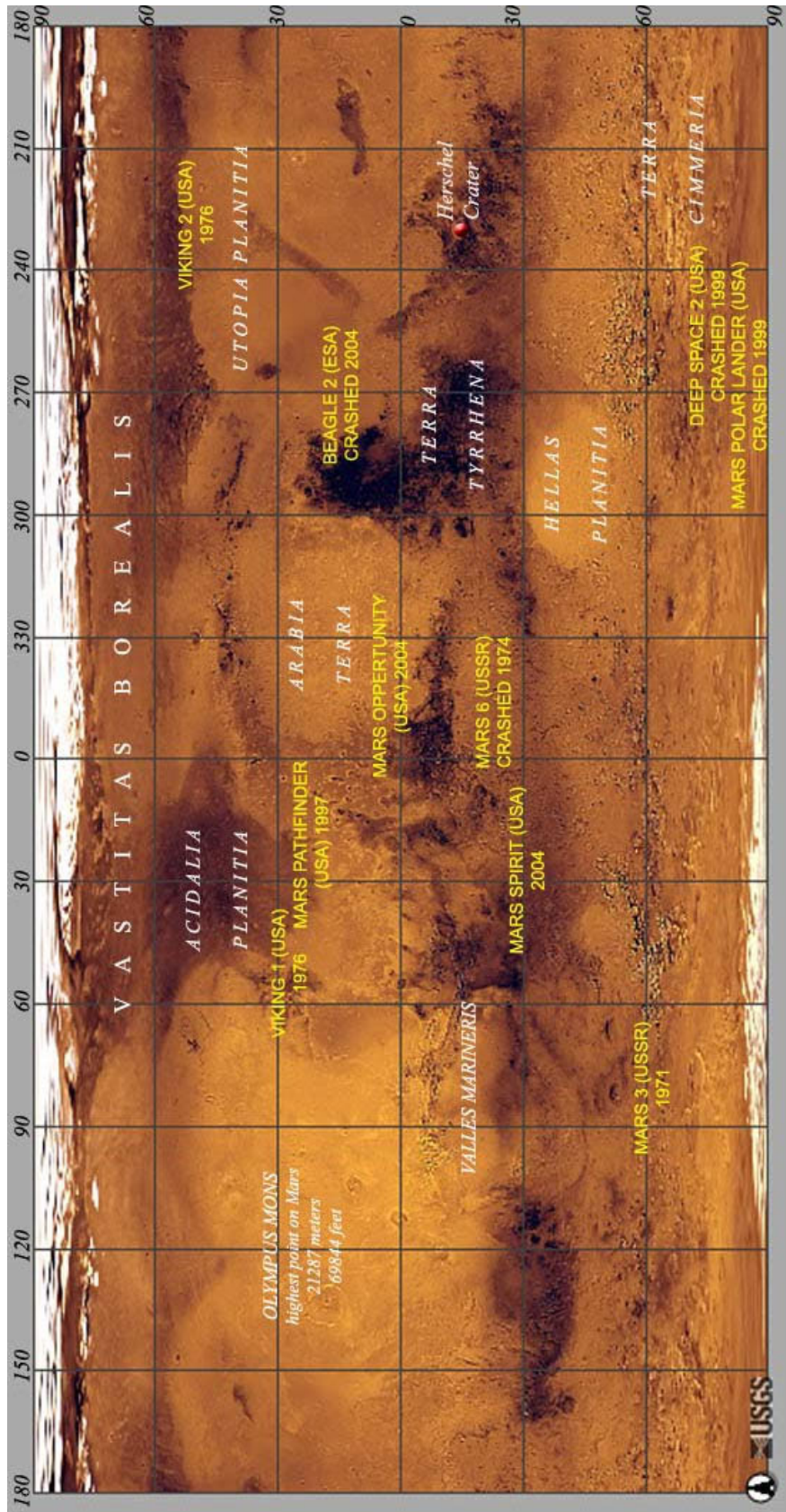


Figure 3. Annotated global map of Mars with selected mission information. PIGWAD base map

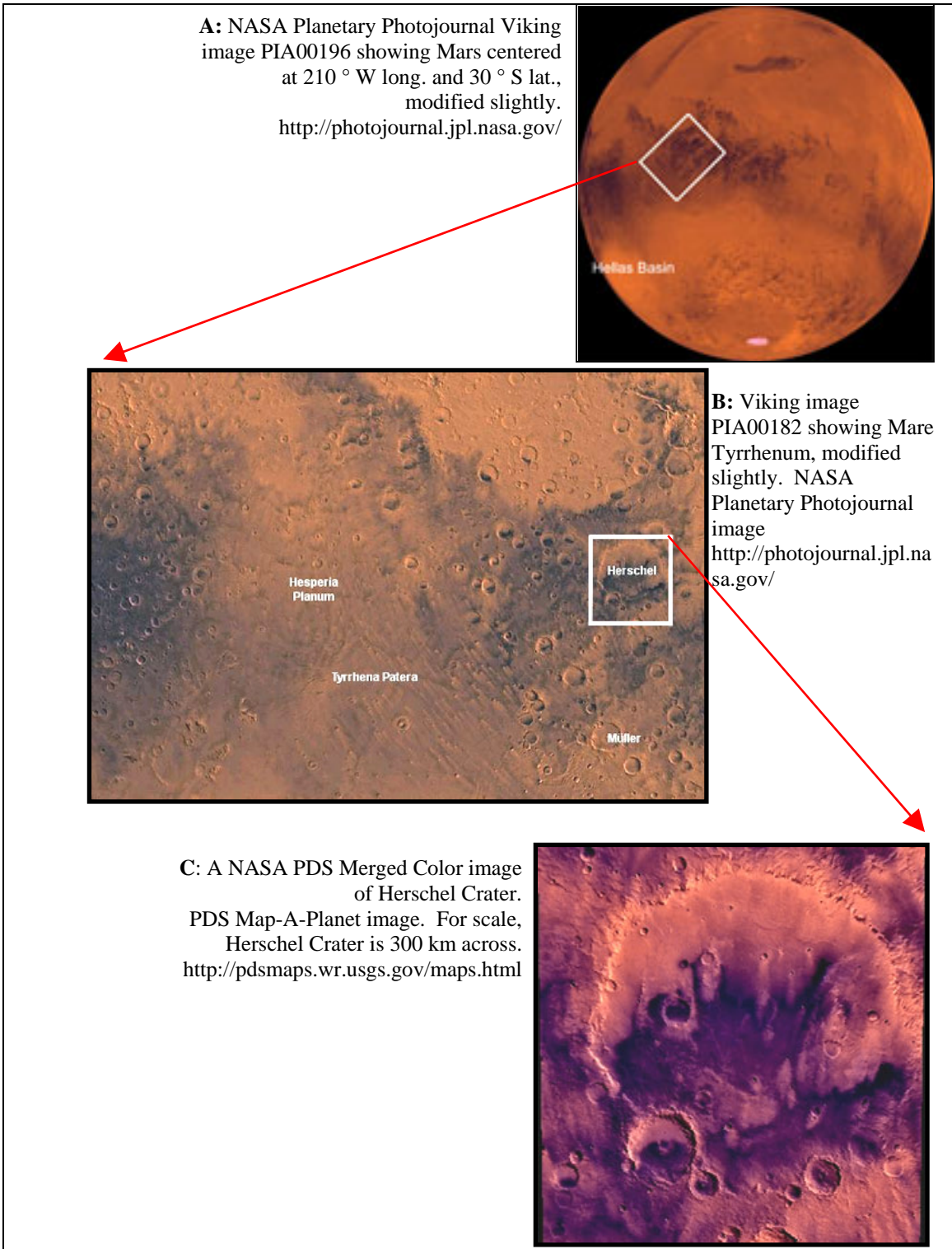


Figure 4. Planetary perspective of Herschel Crater location

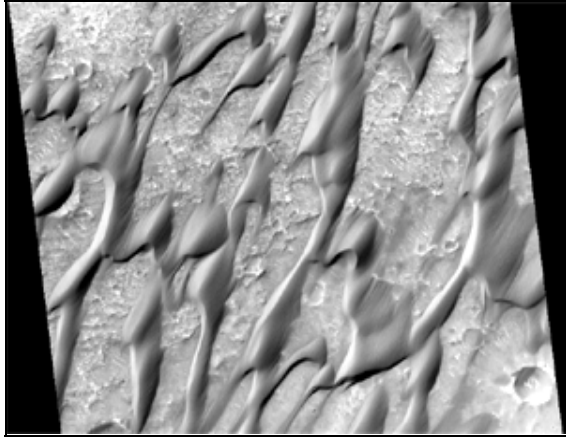


Figure 5. Cropped Mars Orbital Camera (MOC) image of dune forms in Herschel Crater suitable for inferring wind directions. Field of view is 3 km wide. Original image from Malin Space Science Systems #E0200602.

CHAPTER II

LITERATURE REVIEW

Determining Wind Direction from Eolian Features

Publications on the subject of surface winds and eolian features on Earth date back to at least the middle 19th century (Easterbrook, 1993). Texts and articles on the subject are plentiful (Bagnold, 1941; Marrs and Gaylord, 1982; Thomas, 1989; Shao, 2000, and many others). Bagnold's 1941 book, *The Physics of Blown Sand and Desert Dunes*, details not only eolian landforms but the physics of the winds, materials, and material supplies required to create them. Bagnold described and explained a set of eolian landforms, including barchan and longitudinal dunes, sand shadows and sand drifts, and the conditions under which they are created. Later studies have built on and refined Bagnold's (1941) work, and it is still a foundation for modern studies. Comprehensive texts by Greeley and Iversen (1985), Lancaster (1995), and Shao (2000) are three examples that heavily cite Bagnold. These recent studies have relied on extensive field and wind tunnel observation to characterize eolian landforms. As we enter the 21st century our knowledge of eolian processes on Earth is relatively well developed.

Eolian landforms arise in response to a combination of local controlling factors. These controlling factors include wind, sand size, sand availability, moisture content, vegetation, and topographic influences (Marrs and Gaylord, 1982). In the case of erosional landforms, such as yardangs, resistance to erosion is also important (Breed et al., 1989). With the introduction of remote sensing from aircraft and satellite,

geomorphologists have bridged what is studied in the field with how it appears in aerial photography and from space. From either field or remotely sensed data, eolian landforms can be morphologically classified, from which it is possible to infer the eolian conditions under which they were created (Marrs and Gaylord, 1982). *Geomorphology from Space*, edited by Short and Blair (1986), details the usefulness of remotely sensed imagery to the geomorphologist and makes comparisons of aerial, field and satellite imagery of a number of geomorphic features. The book is currently available online at <http://daac.gsfc.nasa.gov/www/geomorphology/>. Walker (1986), in *Geomorphology from Space*, compares examples of local eolian landforms observed in highly oblique aerial photography with a regional Landsat image (Figure 6). Remotely sensed data allows for the geomorphologist to study and classify eolian features and infer some of the formative conditions in an area without actually visiting the area. These interpretations are still based on prior field and experimental knowledge. One cannot, for instance, determine the formative wind direction of a remotely imaged dune field without first understanding how wind interacts with dunes. However, the use of remote sensing is a powerful tool when we wish to explore regions that are very large or not easily accessible for field study.

A large part of this research relies on inferring wind direction from eolian landforms. This warrants some broad discussion about how such determinations are made for various eolian landforms found on Earth. This discussion is not meant to be all inclusive, but focuses mainly on those eolian forms that have been observed on Mars.

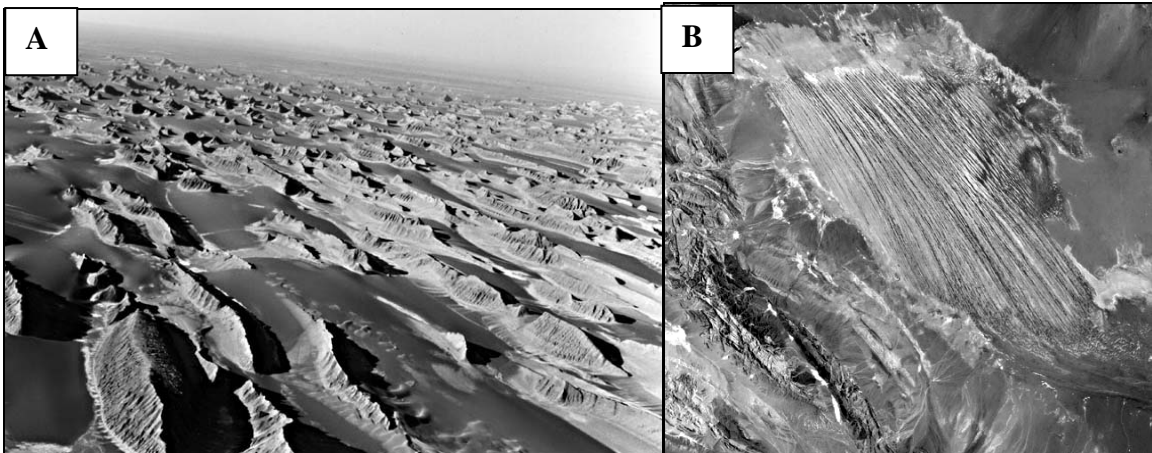


Figure 6. A) A high obliquity aerial photograph of yardangs in the Lut Basin of Iran. B) The region and yardangs as seen in a Landsat image. Landsat field of view is approximately 190 km. (Walker, 1986)

Eolian landforms can be classified into two wide categories, depositional and erosional. Depositional landforms include dust and loess deposits, sand ripples, dunes, and streaks. With the exception of dust and loess deposits, these landforms are generally composed of sand-sized particles (62 – 2000 μm) with a possible small fraction of pebble-sized grains (Greeley and Iversen, 1985). It is not by chance that the particle size is so constrained, as even if the original sediment source of a sand deposit was more poorly sorted, such as a mixed river deposit, the way in which wind transports particles render it an effective sorting mechanism (Greeley and Iversen, 1985). Particles much larger than sand sized will be left in place while sand is migrated out of an area. Particles that are smaller than sand are entirely carried away from the deposit all together.

Primarily, wind moves particles in three ways: suspension, saltation, and impact creep (Bagnold, 1941). In the saltation processes, surface shear stress exerted by wind causes a grain to lift vertically off the surface (Figure 7, point “A”). The grain is then

carried downwind with additional energy being added to its motion by the wind. Sand-sized particles are too large to be held in suspension, and upon impact with the ground can cause a number of processes to occur. The particle may simply bounce back into saltation, lift additional particles into saltation (Figure 7, point “D”), bounce off a larger particle (Figure 7, points “B” and “C”), or dislodge fine particles into suspension. Additionally, the particle may strike a larger grain and push it downwind a short distance in a mode of transport termed impact creep.

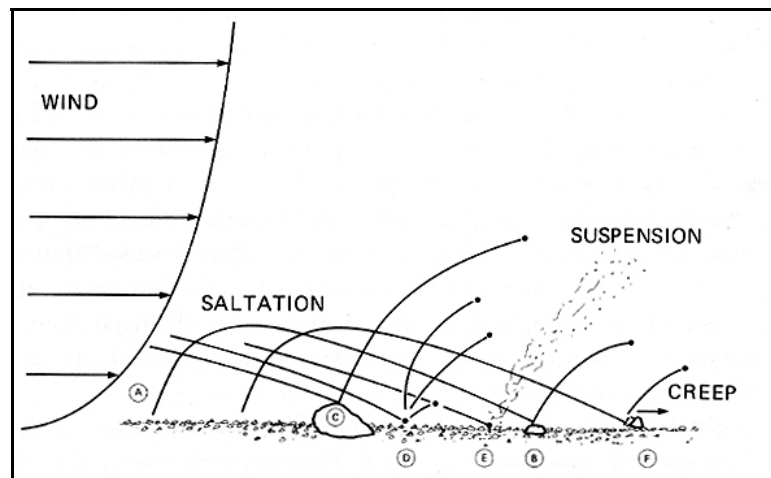


Figure 7. Diagram showing the three principal modes of eolian transport (Greeley and Iversen, 1985, p. 17).

Particles small enough to stay in suspension (silts and clays) are carried away from the main deposit. These particles may be laid down in a localized region creating a dust or loess deposit (Greeley and Iversen, 1985) just downwind from the parent sand body (Bagnold, 1941). Particles too large “...to be moveable either by the direct pressure of the wind or by the impact of other moving grains” (Bagnold, 1941, page 6) will be left in place as the wind transports the rest of the deposit away. The end result of this is a lag deposit of the larger particles (Greeley and Iversen, 1985) with a migrating deposit of sand-sized particles downwind. The processes of saltation and impact creep combine to

sculpt bedforms or landforms out of the resulting sand deposit. From these resulting eolian sculpted forms and an understanding of how they are created, wind directions can be inferred.



Figure 8. Sand ripples. Wavelength is approximately 10 cm. Formative wind direction was from the right. Image: C. T. Adcock, 2004 Puerto Penasco, Mexico

Sand ripples are one of the smaller eolian bedforms (Figure 8). They generally consist of regularly spaced “waves” of sand ranging in wavelength from 1 cm to a couple of tens of meters with heights up to 25 cm (Greeley and Iversen, 1985). They form with the crest perpendicular to the wind direction and a lee side slope, or slip face, somewhat steeper than the stoss slope. Slip faces constitute a reliable marker of wind direction as they nearly always dip downwind (Fenton et al., 2003). This allows for formative wind direction determinations to be made easily (Figure 9). Ripples can be formed or mobilized in ideal conditions in a few minutes and as such they are considered a “snapshot” of current or recent sediment transport and wind direction in a localized area. While small scale ripples do not generally appear in images acquired from orbit, they

have been seen on Mars by surface missions (Figure 10). Bright mega-ripples have been observed on Mars in orbital imagery (Thomas et al., 1999). Whether or not these should be classified as ripples or dunes is still unclear, and they are referred to sometimes as dunes (Thomas et al., 1999) or simply as transverse eolian ridges (Bourke et al., 2003). They are not well understood, and often other local eolian forms overlie them and indicate a different formative wind direction (Thomas et al., 1999). Figure 11 is an example of this from Herschel Crater. Darker sand deposits overlie the bright ripples indicating that the bright ripples are older. The more recent eolian forms indicate formative winds from the north, but the ripples indicate winds from the southwest or northeast. For this reason, bright mega-ripples are not used to infer wind directions in this study as they appear to be the product of an older wind regime.

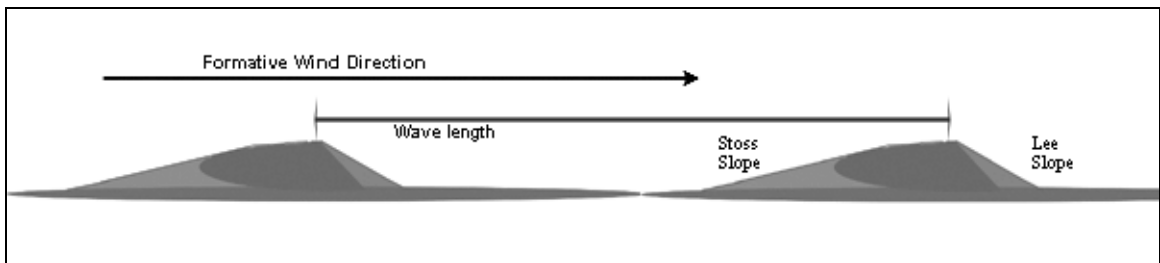


Figure 9. Diagram of ripples in cross section along short axis.

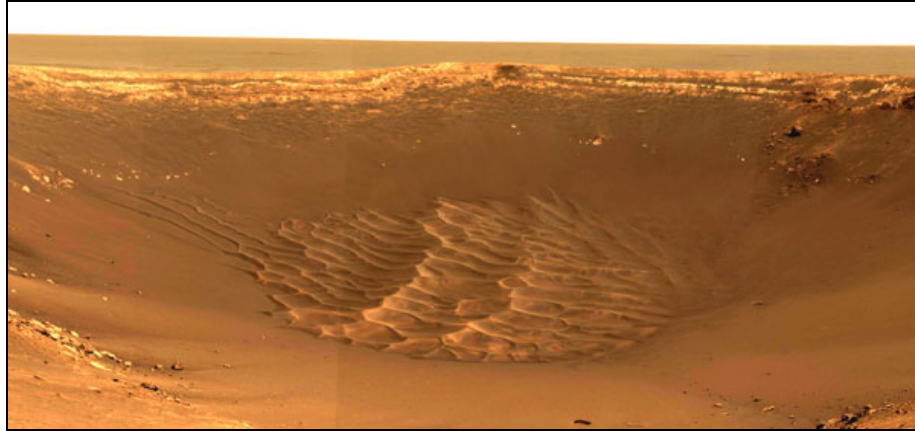


Figure 10. Ripples seen from Mars Exploration Rover (MER) Opportunity in Endurance crater, Mars. Image has been contrast enhanced. For scale, the ripple “field” in the image is roughly 30 meters across. Excerpted from Planetary Photojournal image PIA06276 (<http://photojournal.jpl.nasa.gov/>).

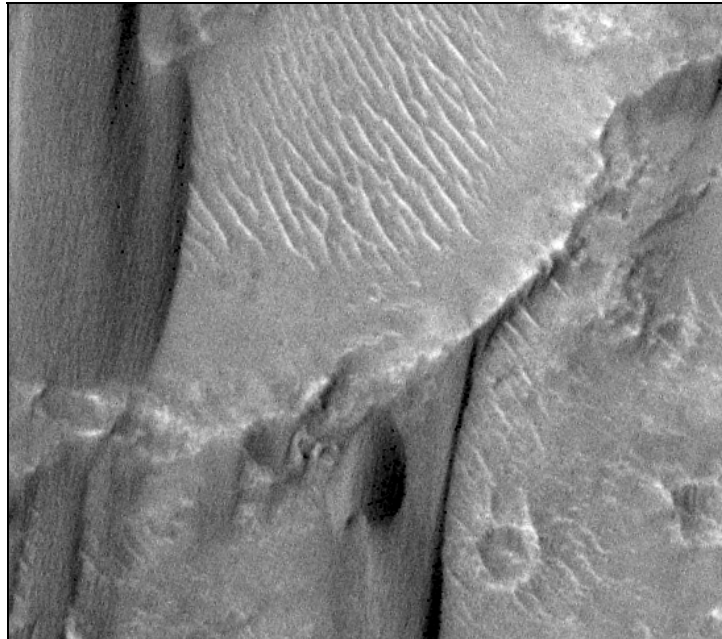


Figure 11. Bright ripples overlain by darker eolian deposits in Herschel Crater. Formative wind direction for the ripples and overlain forms is dissimilar. Image field of view is 830 km. Excerpted from MSSS MOC NA image R0500941 (http://www.msss.com/moc_gallery).

Dunes are much larger than sand ripples. They appear in many different morphologies ranging from simple and symmetric to complex and highly asymmetric

(Figure 12). Perhaps the simplest dune forms to infer wind direction from are those classified as *transverse dunes*.

Transverse dunes, like sand ripples, form with the crest perpendicular to the prevailing wind direction. Like sand ripples they have a lee slope or slip face that is much steeper than the stoss side slope. Often the lee slope is at the critical angle of repose (~34 degrees for dry sand). Three main types of transverse dunes are recognized: barchans, barchanoid ridges, and transverse ridges (Figure 12).


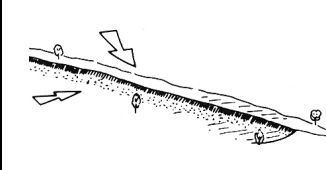



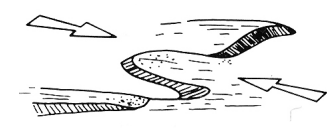
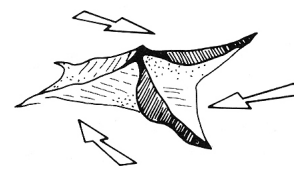
Dune Type	Form	Number of Slip Faces	Dune Type	Form	Number of Slip Faces
Transverse Dunes			Linear Dunes		
Barchan Dune		1	Linear Ridge		1 - 2
Barchanoid Ridge		1			
Transverse Ridge		1	Seif Dune		2
Additional Dunes					
Reversing Dune		2	Star Dune		3+

Figure 12. Diagram of basic dune forms. Modified from (Thomas, 1989, p. 242)

Barchan dunes tend to form in areas where sand supply and vegetation are limited and wind is relatively unidirectional and moderate in strength. In plan view barchans are crescentic in shape and tend to be uni-axially symmetric (Figures 13). Typically, barchan

dunes are small with a horn-to-horn width in the 40 meter range (Greeley and Iversen, 1985) and heights <10 meters (Shao, 2000). Where they exist, barchans clearly signify formative wind direction as the horns and the apex of the interior slip face are oriented toward the downwind direction. Asymmetry in plan view of a barchan (one horn is longer than the other) is attributed to limited variation in wind direction, asymmetric sand supply, or topographic effects (Lancaster, 1995).

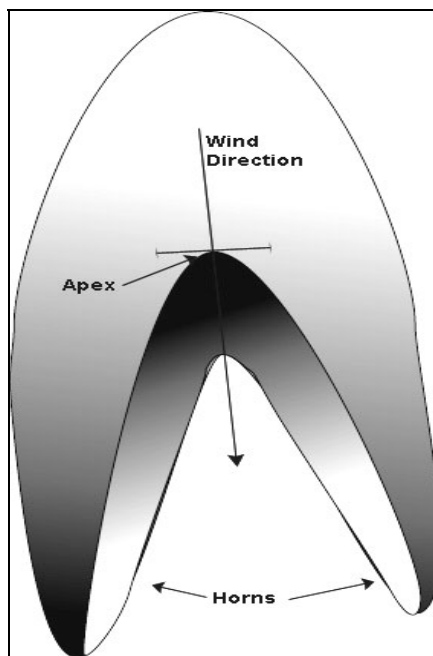


Figure 13. Diagram of a barchan dune showing horns, formative wind direction, and slip face apex.

With increased sand supplies, barchanoid ridge dunes can form (Figure 12). These transverse dune types are characterized by long crescentic ridges. Here, determining wind direction is somewhat more difficult than with simple barchans, but can be obtained generally from measuring a few directions based on the apex of slip faces and averaging them.

These barchanoid ridges themselves can transition into what are formally called transverse ridge dunes. The main morphological difference being a straighter ridgeline oriented perpendicular to formative winds (Greeley and Iversen, 1985). This straighter ridge eliminates some of the difficulties in wind direction determination from barchanoid ridges.

Another broad class of dunes called linear (sometimes called longitudinal) dunes includes those forms in which the slopes of the dune run parallel to the formative wind direction or parallel to the average of formative winds. These dune forms are more difficult from which to derive wind regime.

Two general categories of linear dunes exist: those that have curving crests, called seif dunes, and those that have straighter crests, called linear ridge dunes. Part of the difficulty in determining formative wind direction comes from the numerous hypotheses and controversy around the exact mechanisms of formation (Greeley and Iversen, 1985). One concept was originally put forth by Bagnold (1941) in which a seif type linear dune could be formed from a barchan dune (Figure 14). In Figure 14, the dune form progresses from “a” to “e” through time. The original formative wind direction is noted by “g” and has formed a simple barchan. Strong, episodic winds coming from the direction of “s” begin to elongate one of the horns. In Bagnold’s concept, the “s” winds are from storm events and may contribute more sand to the dune form. The end result is a seif linear dune elongated along the average wind vector and possessing slip faces along one side and slip face apexes oriented mainly downwind.

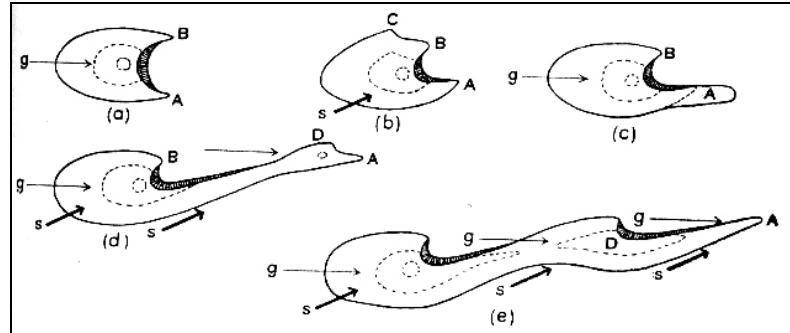


Figure 14. Transformation of a barchan into a linear dune (Bagnold, 1941, p. 223)

Bagnold's concept is still considered applicable, but the Tsoar model is another that is commonly discussed (Thomas, 1989; Lancaster, 1995; Shao, 2000). In this model wind approaches the linear dune at an oblique angle. The winds overshoot the crest of the dune and get deflected "down-dune" on the lee side (Figure 15). According to this model, winds of up to 40 degrees deviant from parallel can be at work. It is possible that in different locations one model is more accurate than the other. Regardless, without additional supporting data such as nearby barchan dunes, inferring wind direction from these types of dune forms is tenuous.

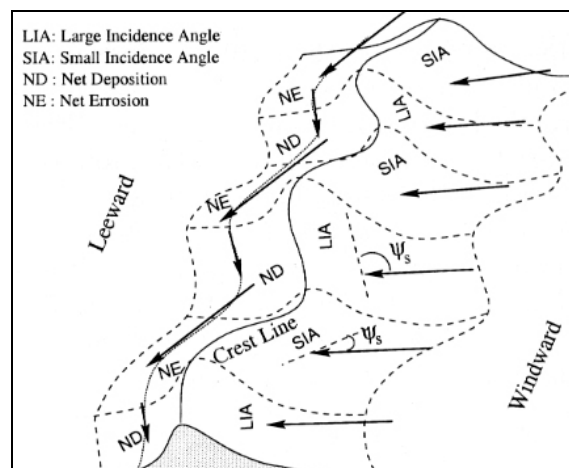


Figure 15. Diagram of the Tsoar model of seif dune formation (Shao, 2000, p. 331)

Linear dunes that do not exhibit the seif morphology tend to have straight ridge lines. One model of formation describes a dominant wind direction that is parallel to the ridge line with occasional, weaker transverse winds maintaining dune form (Figure 16). Another model employs helical flow between dune ridges with a net flow parallel to the ridgeline (Figure 17). In both models the net predominate flow is longitudinal to the dune ridge. These dune forms may converge, creating “Y” junctions that open upwind allowing for an overall wind direction to be inferred (Lancaster, 1995).

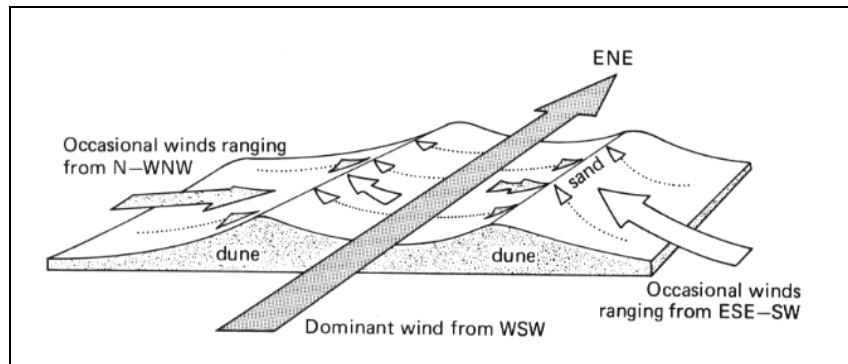


Figure 16. Transverse component liner dune formation model (Greeley and Iversen, 1985, p. 170)

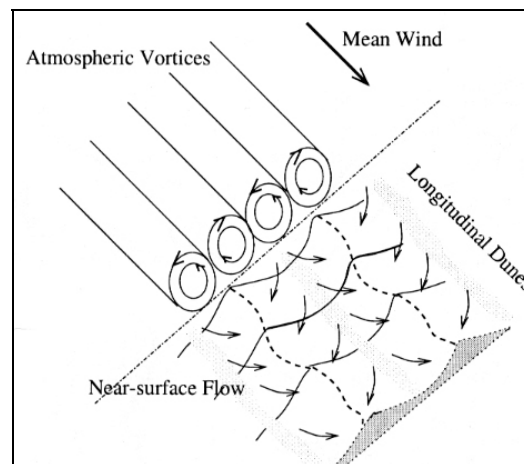


Figure 17. Linear dune formation model utilizing helical flow (Shao, 2000, p. 330).

Other dune forms develop that are not discussed above because they involve interaction with vegetation (i.e. parabolic and coppice) or in the case of some complex and “mega” dune forms (i.e. mega-barchans, feather dunes) the techniques for wind direction determinations are similar to those mentioned above. Three additional dune forms are of note however. Star dunes are complex dunes that form in multidirectional winds. They can appear pinwheel shaped (Figure 18). They are important in terms of wind direction in that they indicate no single dominate wind direction at work. Echo dunes occur when a dune forms or migrates toward a steep scarp (Figure 19). The formative winds coming off the crest of the dune get deflected back (or “echoed”) into the slip face forming a “moat” between the dune and scarp (Greeley and Iversen, 1985). Finally, reversing dunes are a type of complex dune that arise when directly opposing formative winds exists. They are characterized by a ridge with slip faces on both sides. The opposing winds are generally not equal and a slope side dominated by slip faces indicates the direction of the stronger wind.

While dunes can be good indicators of wind direction, wind streaks and sand shadows are obvious indicators. Unlike most dune forms, streaks and shadows are generally anchored to an object and dependant on it to exist (Bagnold, 1941), though in some cases streaks can be independent (Greeley and Iversen, 1985). The difference in the terms when applied to terrestrial geomorphology is one of formation. Sand shadows are deposits that form in the wind shadow zone on the lee side of an obstruction. The term wind streak refers to material being eroded from a landform and streaked downwind. Both may change orientation, but are usually anchored to an obstruction. When referring to Mars, the terms get confused and the term streak is often applied to

forms that may be depositional. The reason for this may lie in the fact that similar looking eolian forms on Mars can be formed in different ways. Greeley and Iversen (1985) compiled wind tunnel experiment data from their previous studies that show material from inside a crater can be deposited as a tail or streak, or under different conditions material could be deflated from the lee side of the crater to produce a streak. Additionally, it is possibly that the tails observed on craters are produced by the erosion of material outside the wind shadow zone of the crater, leaving behind differently colored material as a tail. Generally, the tails seen on the lee side of craters in orbital imagery of Mars are referred to as “crater streaks”, regardless of formation processes, and the term sand shadow is reserved for obvious shadows in lander and rover images. Regardless of the mode of formation, they are obvious indicators of wind direction. Where present, the formative wind direction is coincident to the streak or shadow with the anchor end upwind. The scale of wind streaks and sand shadows is highly variable from centimeter to kilometer ranges (see Figures 20 and 21). They are present in the Herschel Crater region (Figure 21).

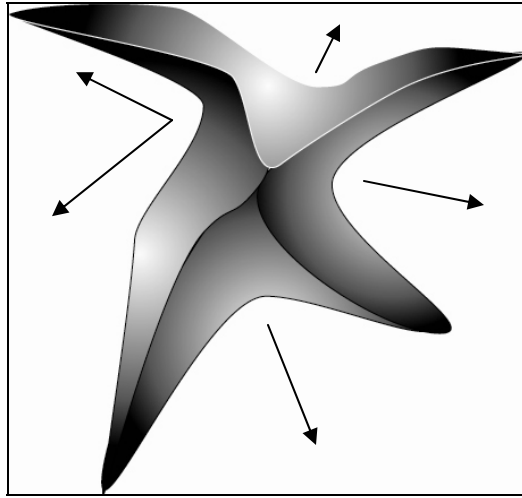


Figure 18. Diagram of a hypothetical star dune and formative wind directions (arrows) in plan form.

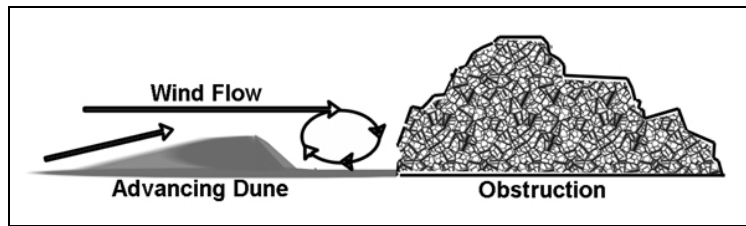


Figure 19. Cross-section diagram of an echo dune.



Figure 20. Small sand shadows formed behind shell fragments on a beach. Longest is <10 cm long and wind direction is toward the left. C. T. Adcock image Las Conchas, Mexico 2004.



Figure 21. Martian crater streak from the Herschel region. Crater streak is roughly 5 km long. MSSS image E1000272 (http://www.msss.com/moc_gallery).

Eolian landforms created by erosion include ventifacts, desert pavement, lag deposits, blowouts, and yardangs. Ventifacts are rocks that have been grooved, fluted, pitted, and or polished by windblown abrasives. They can be used to determine wind direction if found in situ. Obviously the relatively small size of them limits their utilization in this study. Desert pavement, lag deposits and blowouts represent landforms where wind has removed material. As direction indicators they are of little use without additional landforms, such as ripples or a downwind sand deposit observably present. Yardangs offer more promise as wind indicators. They can be large enough to be viewed in orbital imagery (Figure 6). They are bodies of bedrock that have been streamlined by wind erosion and thus are elongate parallel to the formative wind direction. In plan view, yardangs tend to “tail off” on the downwind side as an indicator of wind direction.

Martian Eolian Studies

Planetary scientists have begun to study the eolian environments other planets, such as Mars, through *comparative planetary geology* (Greeley and Iversen, 1985). Studying the eolian environments of other planets offers a unique set of problems. For instance, differences in gravity and atmospheric pressure have a dramatic effect on eolian processes. On Earth, the threshold friction speed, or wind speed at the surface required to lift a sand particle and initiate saltation under typical conditions is about 0.2 m/s (Figure 22). For Mars, the threshold friction speed is predicted as an order of magnitude higher (2 m/s). The values for Earth have the benefit of confirmation through field study and direct measurement. Direct measurements of other planets are rare and field studies are currently out of the question. Manned missions to other planets are likely decades away and the dangers associated with such missions require as much foreknowledge as possible. Probes offer an opportunity to gather data with much reduced risk to human life, and Mars is the most studied of terrestrial planets in this manner. The types of probe missions we have sent to Mars fall into two basic classes, those that land and those that do not. Landing missions consist of a stationary lander and or a mobile rover. The advantage of these types of mission is that they can take direct measurements and close up images. The disadvantage is that they can only cover limited areas and are often positioned to land in areas of high landing success probability rather than scientific importance. In contrast, flyby missions make a single or just a few passes around the planet without landing, while orbiter missions establish long term orbits. Flyby and orbiter missions can cover large regions of Mars, if not the entire planet, but at much reduced image spatial resolutions. As an example, our current rovers can collect images

with resolutions of less than 1 mm/pixel while our best orbiter can attain 1.5 m/pixel resolution. The different mission types have strengths that can be applied depending on the mission objectives.

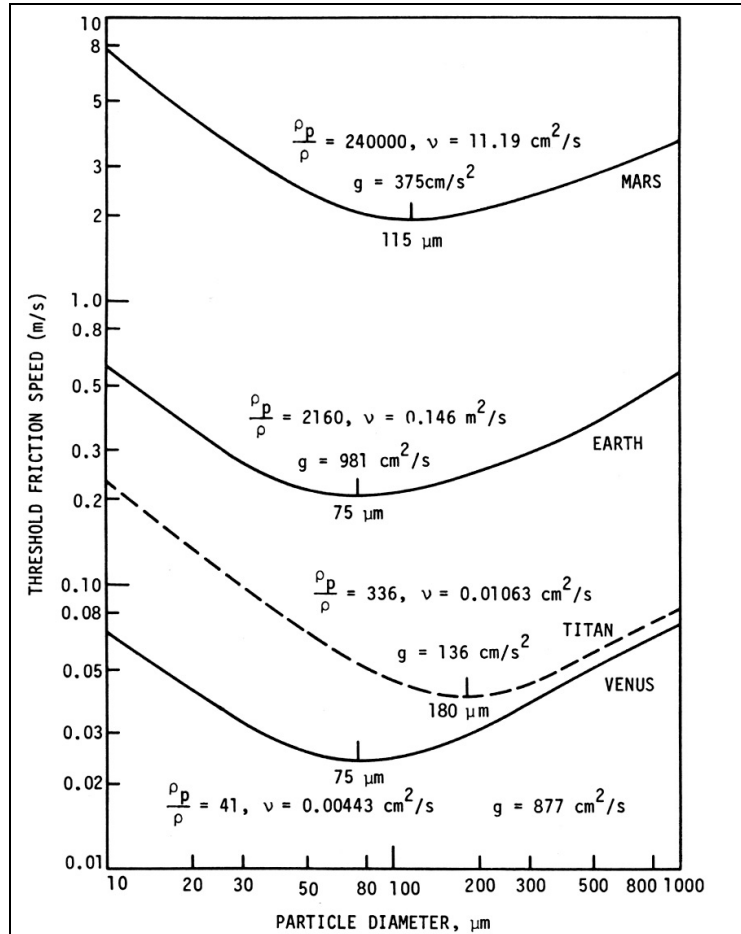


Figure 22. Threshold friction speeds predicted for planetary bodies including Earth and Mars (Greeley and Iversen, 1985, p. 92)

Probes have grown considerably in sophistication over the decades and each successive mission yields more useful data both in quality and quantity. Our current Martian orbital image catalog consists of well over 250,000 images from about a dozen successful orbiter missions with resolutions ranging from hundreds of kilometers to 1.5

meters. Table 1 shows the improvements that have been made in image resolution for both landing and orbiting mission since our space program began.

Table 1. Visible spectrum camera resolutions of selected missions to Mars showing advancement over time.

Flybys and Orbiters		
Mission	Year of First Operation	Best Resolution
Mariner 4	1965	730 meters
Mariner 6 and 7	1969	100 meters
Mariner 9	1971	40 meters
Viking Orbiters	1976	10 meters
Mars Global Surveyor	1998	1.4 meters
Mars Reconnaissance Orbiter	Scheduled late 2005	<0.3 meters
Landers and Rovers		
Mission	Year of First Operation	Best Resolution
Viking Landers	1976	2 mm
Pathfinder	1997	2 mm
Mars Exploration Rovers	2004	<1 mm

Probes are not perfect tools. The success rate for probe missions to Mars is approximately 50%. A truly objective success/failure ratio is difficult to define because countries tend not to release information on failed missions (Sheehan, 1996) and some successes are arguable (e.g. the USSR's Mars 3 Lander only operated for a few seconds after landing). Even the most liberal determinations reveal that we have managed less than two dozen successful missions. Further, each probe sent is equipped with a limited set of tools designed to collect very specific data. They have little flexibility in changing the objective of a mission. However, those missions that have succeeded have provided a

wealth of data, much of which can be applied to studying the Martian eolian environment. The number of studies that focus on the Martian eolian environment is not nearly that of those for Earth, but is growing. A few of these are briefly discussed.

Studies that involve the interpretation of surface wind direction from wind streaks in the polar regions of Mars have been published (Neakrase and Greeley, 2002; Diniega et al., 2003). Diniega et al. (2003) looked at “frost streaks” that form when polar ice melts and exposes sediments to surface winds (Figure 23). The streaks are actually made of the sediments exposed during melting and “streaked” onto the surface of surrounding ice. They give a clear indication of the prevailing wind direction at the time of formation. They are also seasonal and many are erased during Martian winter. This means they are currently active and not preserved indicators of long past, possibly dissimilar winds.

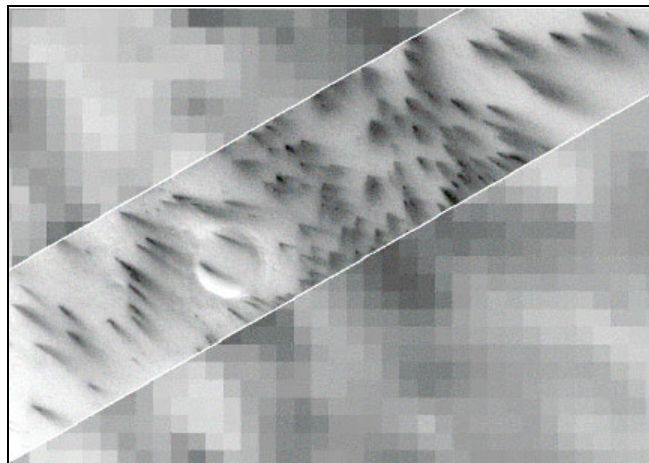


Figure 23. Polar dust streaks on Mars in a MOC NA image. Crater in image is 1.4 km diameter for scale (Diniega et al., 2003).

Other studies focus on dust devils and the streaks that they leave behind (Biener et al., 2002; Ringrose and Zarnecki, 2002; Greeley and Thompson, 2003; Metzger, 2003; Whelley et al., 2003). Dust devils on the surface of Mars were confirmed by the Mars

Pathfinder mission. They have also been captured in Martian orbital imagery. When a dust devil moves across a surface on Mars it picks up surface material and exposes fresh material. The fresh material is of a different color than the older material and thus dust devil paths can be observed from orbit (Figure 24). The axes of these dust devil paths or tracks are thought to be coincident with the prevailing wind direction at the time of formation (Greeley and Thompson, 2003). In Figure 24 this would indicate a wind direction generally from the north-northeast or south-southwest. Without knowing which end of the dust devil streak is the starting point, the exact wind direction cannot be determined. Greeley and Thompson (2003) were able to use them as supporting wind direction evidence in a study that included investigating proposed Mars Exploration Rover (MER) landing sites. At Isidis Planitia, they determined that dune forms indicated winds from the northwest. They supported this determination with dust devil streaks that trended northwest/southeast.

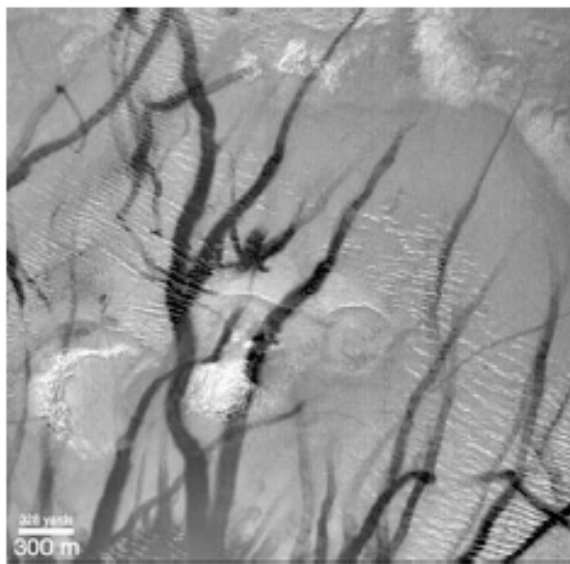


Figure 24. Martian dust devil tracks in a MOC NA image. NASA image PIA 02376, Malin Space Science Systems Camera. (Whelley et al., 2003).

One of the confounding factors in studying eolian features through orbital or surfaced based imagery is knowing if the observed features are indicators of recent or long past wind regimes. Studies of the Mars Pathfinder (MPF) landing site offer a perfect example. Greeley et al. (1999) studied the MPF site and found that dunes, ripples, and sand tails (sand shadows) indicated a formative wind direction from the northeast. This direction correlated with streaks seen in Viking orbital imagery near the site. The direction also correlated with that of the strongest predicted wind in the area in a global circulation model (discussed in more detail below). These determinations did not correlate with ventifacts observed in rocks at the MPF site. The ventifacts indicated a formative direction from the east. Greeley et al. (1999) noted that the rocks the ventifacts were on could have shifted through time but concluded that they are more likely the product of a previous wind regime. Kuzman et al. (2001) followed up the study with an investigation of small eroded craters in and around the MPF site. Winds passing over a crater exert the most shear stress on the leeward rim and tend to erode or modify it faster than the rest of the crater rim. The result is that one can infer wind direction from an eroded crater. Kuzman et al. (2001) found that wind directions inferred from the eroded craters match those of the ventifacts at the MPF site. Both ventifacts and crater erosion take a significant amount of time to develop when compared to depositional eolian forms such as dunes and ripples. Additionally, they are not easily modified or erased after creation. This supported the conclusion that the ventifacts had not been shifted, but were indicators of a past wind regime at the MPF site and the more easily modified depositional forms represent the current formative wind direction.

Crater streaks are abundant on Mars and have been studied as well as modeled in wind tunnels since before the Viking missions (Greeley et al., 1974). They were first seen in Mariner 9 imagery and termed *variable features* (Thomas et al., 1981). As mentioned previously, they can be the product of erosion or deposition and are excellent indicators of wind direction. There has also been research that investigates the movement of dunes or other surface changes on Mars (Geissler et al., 2002; Fenton, 2003; Williams et al., 2003). These studies typically compare temporally different but spatially overlapping images to determine if change has occurred. None of the above studies were able to confirm dune movement. The fact that movement of dunes has not been seen does not mean that surface changes have not been observed. As previously mentioned, seasonal changes in wind streaks have been observed (Thomas and Veverka, 1979; Diniega et al., 2003) and mass movement events are also apparent in the form of dust avalanches (Sullivan et al., 2001; Aharonson et al., 2003) along ridges. Thomas and Veverka, (1979) studied crater and other streak orientation on Mars globally and noted that some of the streaks change in orientation and length through time. Using Viking orbiter data taken over a span of 1.5 Martian years, they were able to correlate changes to seasons and concluded that most changes occur during the period between late southern hemisphere spring and early southern hemisphere fall. This is the time when Mars is at perihelion and receives the highest amount of energy from the Sun.

Part of the problem with studies of dune movement is a lack of overlapping imagery of sufficient resolution. Malin Space Science Systems, the operator of the Mars Orbital Camera (MOC) on the Mars Global Surveyor (MGS), states on their MOC target request web site “The MOC narrow angle camera has only covered about 3% of the

martian surface. Your suggestion must be for a new place on Mars, not previously imaged by MOC“ (<http://www.msss.com/plan/intro>). Adding to the problem further is the time span available for overlapping images. The MOC camera has only been collecting images for about 3 Martian years. With a best resolution of 1.4 meters/pixel, a dune would have to move a considerable distance, possibly over 6 meters, for the movement to be observable. The author’s own field experience near Puerto Penasco, Mexico suggests that, even in the presence of daily formative winds, dunes move slowly. Edgett and Malin, (2000) in a study that includes an investigation of current eolian activity on Mars, point out that in some terrestrial settings migration of dunes may occur on the scale of centuries.

Of particular interest to this study, Edgett and Malin (2000) studied the activity and inactivity of eolian landforms on Mars. Specifically they noted that grooves and ridges can be seen on dunes in some of the high resolution imagery of Herschel Crater. They interpreted this to mean the dunes are lithified or indurated and are experiencing abrasion and plucking. This is discussed in more detail in the results and discussion of Chapter IV.

Perhaps most similar to work done for this research is that of Lori K. Fenton, much of which is compiled in her Ph.D. dissertation (Fenton, 2003). Fenton used geomorphic interpretation of dunes in Proctor Crater from high resolution MOC imagery to infer wind direction. Proctor Crater is ~150km in diameter and sits in the southern highlands of Mars east of Hellas Basin. The crater contains dark dune forms similar in albedo to those observed in Herschel Crater and thought to be composed of basaltic material with a minor andesitic or weathered basalt component (Fenton et al., 2003). The

similarities in dune albedo between Proctor and Herschel Craters may be an indication of a similar dune composition in Herschel. Fenton (2003) found that Proctor Crater lies in a region of multi-directional formative winds from 239°, 110° and 79° by inferring wind direction from dune geomorphology. In comparison, the Herschel Crater study area is relatively large, about 4 times the area (approximately 100,000 km²) of the Proctor Crater region investigated by Fenton. At this size, regional differences in wind direction should be evident. Also, the area lies within the zone of 25°N. to 25°S. latitude and this region should experience dramatic seasonal shifts in wind direction due to Martian axial obliquity, introducing another confounding factor into linking eolian forms with dominant wind direction.

General Circulation Models

Image analysis/interpretation alone is not the only approach to studying winds. The general circulation of surface winds on both Earth and Mars has been modeled (Blumberg and Greeley, 1996; Joshi et al., 1997; Haberle et al., 1999; Fenton, 2003; Haberle et al., 2003). These computer generated general circulation models (GCM) use the “primitive equations of meteorology” (Joshi et al., 1997) to predict the global circulation of a planet. Blumberg and Greeley (1996) used a Goddard Laboratory of Atmospheric Sciences GCM to compare modeled wind directions with sand drift and dune orientations on Earth. They found that wind direction indicated by dune morphology agreed with the GCM for arid regions in five out of seven study regions. In regions where the GCM and observations did not correlated, geographic complexities such as topography and nearby large bodies of water combined with the coarse spatial

resolution of the GCM may have been a factor. Blumberg and Greeley (1996) suggest that eolian features can be used as verification of GCM and may be more useful than weather station verifications which are highly affected by local phenomena. This is advantageous when conducting similar studies of Mars as only three ground truth points exist but eolian landforms are relatively abundant. Martian GCM are often based on terrestrial models but modified for Martian conditions such as the CO₂ atmosphere, suspended dust opacity, surface albedo differences and in the more modern models, Mars Orbital Laser Altimeter (MOLA) data (Fenton, 2003). GCM models are not restricted to wind direction modeling alone. They are used to model wind speed and even predict surface temperatures (Lewis et al., 1997).

General circulation models (GCM) are not without problems. The spatial resolution (or cell size) of a GCM for Mars is typically 5° to 6°. This roughly corresponds to 100 km wide at the equator, or an area of 10,000 km² on Mars. MOLA topography is averaged over the cell size causing degradation in topography information and the base level for surface flow is often modeled well above ground level. Fenton's (2003) model for example has a base of 200 meters above the surface. Ground truth measurements are limited to the Viking and Pathfinder missions which represent only three data points on Mars, all of which are in the northern hemisphere. With little ground truth and relatively poor spatial resolution, GCM can at best be approximations. This is not to imply that GCM are not useful and powerful tools.

While the two approaches of computer modeling and geomorphic interpretation are very different, they can be used in conjunction (Fenton, 2003) or comparatively (Greeley et al., 1993; Greeley et al., 1999; Kuzman et al., 2001; Greeley and Thompson,

2003). Each approach has its advantages and disadvantages. GCM are global models and are not limited to formative wind interpretations of areas where eolian landforms exist. Further, they can model variables other than wind direction. On the other hand, geomorphic studies are not limited to 10,000 km² spatial resolutions and no GCM can be considered accurate if it cannot be generally validated. With the eventual goal of understanding the winds of Mars in mind, our final understanding will likely come from a combination of geomorphic observations described above and their use in cooperation with, and to refine GCM.

On the forefront of circulation models are “mesoscale models” or regional circulation models that have much higher spatial resolution than a typical GCM (Tiogo and Richardson, 2002; Greeley and Thompson, 2003). GCM are run for an entire planetary body. Mesoscale models use data from a GCM as initial values combined with higher resolution topography data to model specific regions at spatial resolutions better than 10 kilometers. At the time of this writing, no such model had been run for the study area. The author has corresponded with Dr. Tiogo about running the Mesoscale Model 5 (MM5) for Herschel. The MM5 is a terrestrial mesoscale model, but a version has been configured for Martian conditions (Tiogo and Richardson, 2002). Unfortunately, the model will not be run in time to include here.

CHAPTER III

METHODOLOGY

Data Acquisition

Image Data

Malin Space Science Systems (MSSS) is the primary data source for images used in this study (http://www.msss.com/moc_gallery/). MSSS manages the Mars Orbital Camera (MOC) package aboard the Mars Global Surveyor (MGS) currently in orbit around Mars. The MOC platform acquires MOC narrow angle (NA) images at resolutions as low as 1.4 m/pixel (Godwin, 2000), the highest resolution images of Mars and ideal for analyzing small surface features. MSSS makes these images available online for download at the MSSS website. MSSS files the images by date and broad land region, but locating images needed for study using their system is not ideal.

Two more suitable tools for locating images in a given Martian area include JMars (<http://jmars.asu.edu/>) and PIGWAD (<http://webgis.wr.usgs.gov/>). These are Mars centric geographic information system (GIS) tools that allow for quickly overlaying location outlines, called footprints, of available high resolution images on a context image of Herschel Crater (Figure 25). The footprints are linked to data sources (MSSS in this case) where an image can be downloaded for investigation. These tools utilize supporting data from other missions. These data may come from a variety of sources but likely originated or are available at the Planetary Data System (PDS) database

(<http://pds.jpl.nasa.gov/>). The data sets that JMars and PIGWAD use are not trusted to be complete as MGS is still acquiring images. Direct visits to the MSSS database are still necessary to gather any missing data, but are focused on only the most recent imagery. The MOC images used in this study were the highest available resolution, map projected, .gif format versions.

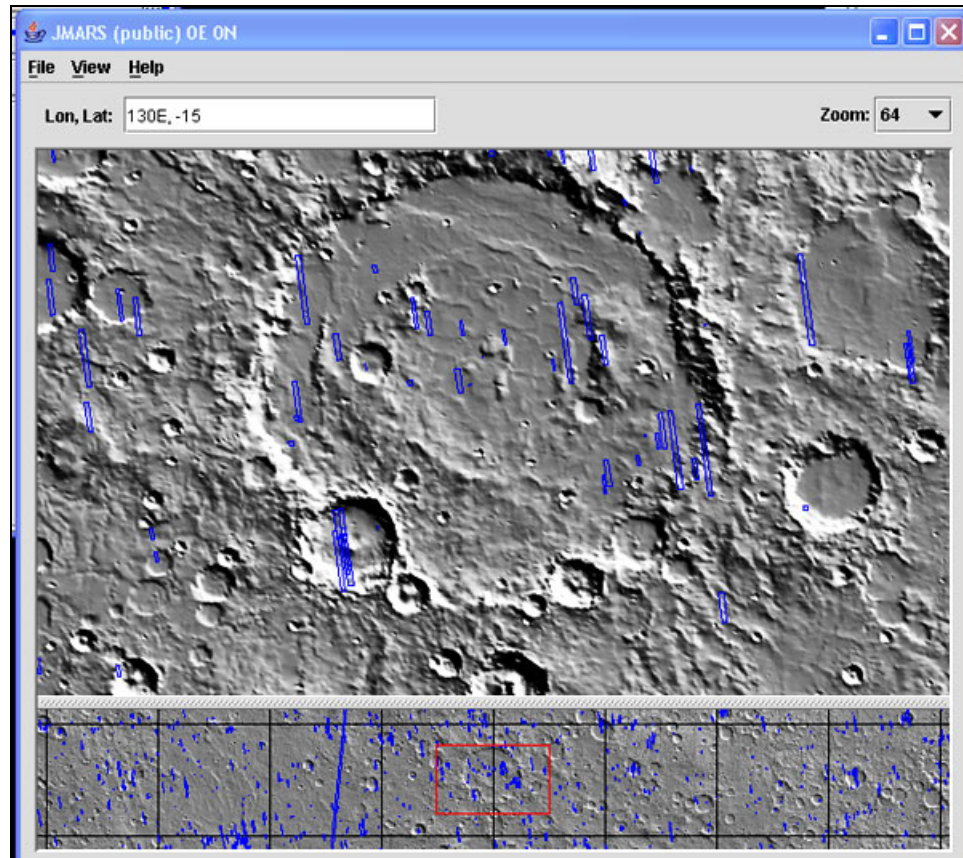


Figure 25. Screen capture of JMars layer manager showing high resolution MOC NA footprints. For scale, Herschel Crater (centered) is roughly 300 km in diameter.

Circulation Model Data

The two most widely used GCM for Mars are the NASA Ames Mars General Circulation Model (MGCM) (Joshi et al., 1997; Haberle et al., 1999) and the Geophysical Fluid Dynamics Laboratory model (GFDL) (Tiogo and Richardson, 2002; Fenton, 2003).

The complexity and expertise, required to generate a global circulation model for Mars, in house, makes it prohibitive for this study. Instead, data in this study come from a recently published model by Fenton (2003) based on the Geophysical Fluid Dynamics Laboratory (GFDL) model. The model is a terrestrial model that has been modified for Martian conditions including MOLA topography, CO₂ atmosphere and dust opacity.

Data Interpretation

Map Generation and Wind Determinations

After all available map projected imagery was located by GIS and downloaded from MSSS, it was electronically cataloged with metadata. Appendix A is the compiled catalog containing the 53 MOC NA images available in the study area. The image captions and metadata accompanying each image are those of Malin Space Science Systems and are not meant to be descriptive in this study. The images were then reviewed with the objective of inferring wind direction from landforms. Interpretations are based on terrestrial analogy to known wind formed structures on Earth as per the discussion in chapter 2 (Figure 12). For each image, wind direction was inferred from multiple objects and a mean was obtained (Figure 26). This was achieved through the use of Adobe Photoshop, a commercial grade imaging software package that allows for angular measurements as well as other image manipulations such as contrast enhancement. First, arrows were drawn on eolian objects to indicate the inferred wind direction. Depending on the type of object being investigated a different arrow color was used. With few exceptions, red arrows were used to denote directions inferred from dune

forms and blue arrows were used to demarcate other eolian forms such as streaks and shadows. Observer error was tested for by obtaining measurements of identical images from two different observers. Difference in wind direction interpretation between interpreters ranged from 1° in straightforward images to 7° in more complex images (Stanley et al., 2004). After determinations were made, Photoshop's measurement tool was used to measure the angle of the placed arrows. Photoshop measures angles in a manner that does not correspond to common azimuth bearings, so the raw measurements were converted. The average direction for the image was then calculated in azimuth.

MOC NA images are often of very high aspect ratio with the long axis oriented near North-South. This means that while an image may be a few kilometers in width, it can be many tens of kilometers in length and the north and south ends are far enough apart to experience different wind conditions. In some cases, this meant that the wind determinations in the northern region of an image were not representative of that in more southern regions. For example, in image M0000790, the streaks in the northern region of the image indicate a wind direction from about north-northeast while streaks in the southern region indicate winds from the north. When this occurred the images were split in half and treated as separate images so that averages were more representative of a specific region. A consistent deviation of inferred directions greater than 10° between northern and southern regions was used to determine if an image should be split. Data acquired from the images appears in Appendix B.

Once wind direction was determined for all of the images, a map of wind direction was created by symbolizing the results (as an arrow) from each image and placing them on a larger image of Herschel Crater. Specific location information was

derived by using JMars to display the MOC NA footprints on a larger image of Herschel Crater. Symbols were then placed at the center of their corresponding MOC NA footprint with Photoshop. If a footprint was not available in JMars, the original coordinates from MSSS for the center of the image were used. Any image data that were split were represented on the map by placing an arrow that corresponds generally to the region the data are derived from on the MOC NA footprint. Any outlying or anomalous results are revisited for confirmation and reinterpreted if needed. An example of an anomaly would be an inferred wind direction that directly opposes nearby determinations. Outlier data are still plotted on the overall map. Once the map was complete, the MOC NA footprints were removed so that the map was easier to read.

Changes in Eolian Features Over Time

Overlapping MOC NA images of the same location and different temporal aspects were closely inspected for evidence of change or landform movement. This was achieved by overlapping and animating (quickly flipping from one image view to the other) images with Adobe Photoshop and Macromedia Fireworks imaging software. This requires processing the images so they are as similar as possible in overall lighting, contrast and resolution. Resolution adjustments drop the higher resolution image to that of its lower resolution counterpart(s).

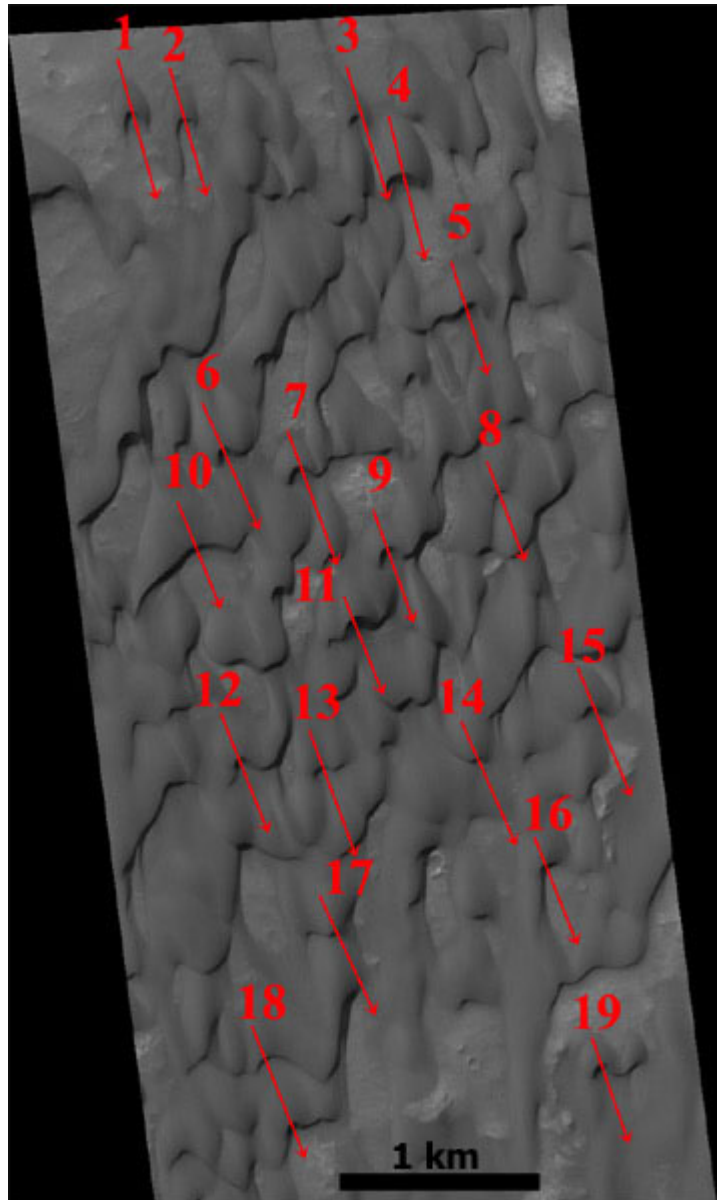


Figure 26. MSSS MOC NA image M23-0263 (cropped) with dune forms shown. Red arrows indicate predominate wind direction for barchan and barchanoidal ridges.

General Circulation Comparisons

Once the wind map was complete, the overall wind direction for Herschel Crater was calculated and compared to the selected GCM for correlation. The overall wind direction determination is comprised of the averages of the mapped wind directions. This

is not an average based on each individual landform measured as that would favor images or areas of high eolian landform density. Instead, the average calculated for each MOC NA image as a whole was used. The rationale for doing an overall average for Herschel Crater is that the GCM spatial resolution is not high enough to allow for comparison to the finer scale geomorphic determinations.

CHAPTER IV

RESULTS AND DISCUSSION

Eolian Landforms Catalog

The catalog generated in this study is located in Appendix A. It contains 53 MOC NA images acquired and listed as map projected in the Herschel area from June of 1998 thru August 2003. The catalog is organized by date of acquisition for ease of updating as new images are acquired and processed by MSSS. This makes it a useful tool for future studies of the area. Appendix B contains the numerical data collected from 432 features found in 31 of the MOC NA images. The data are presented with both the Adobe Photoshop raw angle measurements and the converted azimuth angle as well as some notes taken during image investigation. Appendix C contains the 31 annotated MOC NA images themselves.

Map Generation and Wind Determinations

Wind direction determinations inferred from eolian landforms in 31 MOC NA images are plotted on the map in Figure 27. The eolian landforms in the crater seem to be the product of mainly unidirectional winds for a given area. Wind streaks or shadows have only one tail emanating from their anchor object and most of the dunes observed were transverse types, both are indicators of unidirectional formative winds. Some images contain what appear to be seif dunes that have developed from barchan and

barchanoidal dunes which are also present in the image. This follows the Bagnold model of seif dune development which does have a second directional component, however; Bagnold's model suggests that this secondary direction is very similar to the primary formative wind direction and is episodic in nature. The end result is that measurements taken from these dune forms should still be very close to the primary formative wind direction.

The map shown in Figure 27 indicates that winds are being deflected inward by the crater rim on the western and southeastern sides. This could be the result of simple deflection or the rim walls may act as barriers that induce helical flow much like the winds that produce echo dunes. The rim deflection may also have the effect increasing atmospheric pressure in the southern part of Herschel Crater when winds are active. Along the outside of the northeast rim, wind appears to be deflected toward the southeast around the crater. To confirm this, additional imagery along other parts of Herschel's rim is required. An eroded or low spot in the northeast part of the rim may also be allowing an influx of wind into the crater towards the southwest.

Averaging the MOC NA overall image determinations produces an inferred wind direction generally from the north at 11° toward the south at 191° for the Herschel Crater area. One image produced results that appear anomalous (MSSS # M02-03305). After reanalyzing the image, the results did not change. This image was acquired over the southeast rim of Herschel (indicated as a red arrow in Figure 27) and the winds may be the product of a vortex effect that is reversing the wind direction just as it crests over the rim. Removing these results from the overall average still produces a direction generally from the North (7°). Table 2 summarizes the data collected. Suffixes added to MSSS

images numbers such as “a”, “b” or “c” indicates that the image was split and analyzed as a separate image.

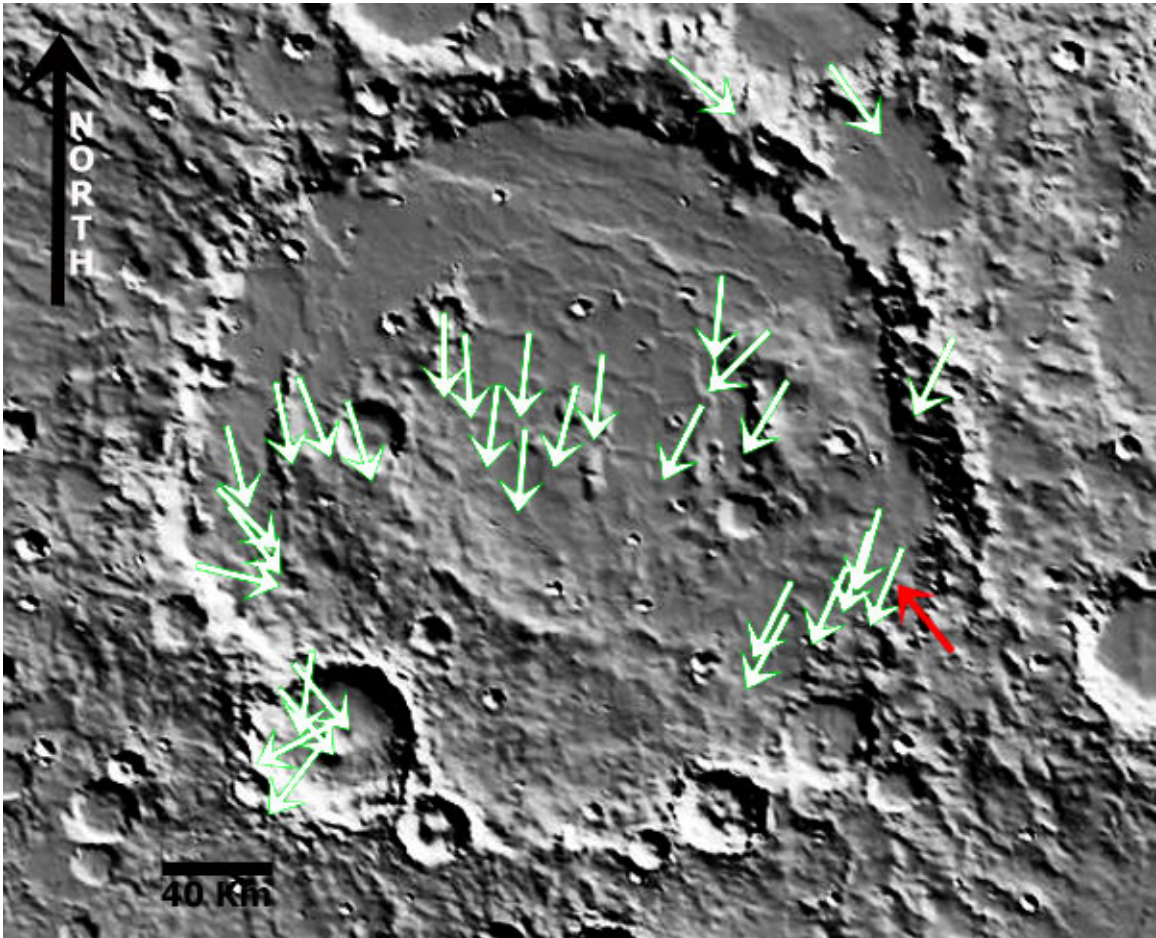


Figure 27. Wind map of Mars on a NASA PDS MDIM1 image of Herschel Crater. Arrows indicate formative wind directions inferred from eolian landforms in this study. Topographic influence on wind direction is evident as wind deflection near the crater rim. Red arrow indicates a determination that does not correspond with the rest of the data and may be localized wind effect.

Table 2. Data summary including number of measurements, mean wind direction and standard deviation by image analyzed.

MSSS#	Number of Measurements	Mean	Standard Deviation
SP36507	15	169.3	3.8
FHA00473	7	103.7	2.4
FHA03181	14	161.6	12.9
M0000790a	7	196.3	4.2
M0000790b	5	184.6	2.4
M003222	18	197.4	9.2
M0200612	7	185.5	1.8
M0201996	10	208.8	4.7
M0201998	12	129.7	4.3
M0202819	20	143.0	10.8
M0203305	19	320.8	5.7
M0303634	9	144.4	2.5
M07-02974	14	217.0	31.6
M07-01919	5	203.9	3.4
M07-05959	10	195.1	7.3
M08-06611	16	175.8	4.2
M11-02107a	12	187.5	43.3
M11-02107b	6	260.5	24.3
M12-00672	5	210.7	3.7
M13-00630	5	206.5	3.2
M14-00754	6	180.1	2.8
M18-00644	8	186.1	3.5
M21-00018a	13	165.5	21.0
M21-00018b	12	156.9	10.0
M21-00018c	14	140.8	9.6
M23-00263	32	158.5	3.9
M23-00825	21	225.9	41.7
E02-00602	17	206.2	2.5
E02-02816	6	207.3	4.0
E09-02803	13	242.6	12.5
E10-00272	20	195.5	4.5
E11-00527	13	202.3	6.0
E11-01859	16	185.1	10.9
E16-01318	17	225.6	7.9
R05-00941	8	187.4	1.2
<i>Overall</i>	432	190.5	

Changes in Eolian Features Over Time

Five sets of overlapping MOC NA images were available for the Herschel Crater area. When compared, movement of dunes could not be confirmed in any of them.

Images M2100018 and M0202819 are shown by JMars to overlap. When the images were retrieved no spatial reference could be made between them. It is possible that this is because dune movement has obscured landmarks. This would require a large amount of dune modification. It is also possible that the two images do not actually overlap and the GIS plotting of the footprint is simply incorrect. Whichever the case, movement could not be confirmed. MOC NA image pairs M2300263/SP236507, R0101236/M0003222, R0300358/M0200612 and FHA01381/R0400598 overlap and could be spatially referenced. They revealed no dune movement on the scale of the image resolution. This would tend to support the conclusion of Edgett and Malin (2000) that the dunes are lithified. However, other studies have failed to observe dune movement in similar resolution imagery and attribute it to insufficient time span for movement to be detected at the available resolution. For Herschel, the time span represents just over two Martian years. Not all of the dunes in Herschel Crater exhibit the grooved texture that Edgett and Malin (2000) use as evidence. Further, the crests of dunes are still sharp and none of the dunes appear to be cratered, indicating they are relatively young. The dunes are not mantled with dust, an indication that wind is still active in the area, and Edgett and Malin (2000) do not provide a possible mechanism for stabilizing the dunes in-situ. It is unlikely, for example, that the dunes are frozen given their proximity to the equator. This author speculates that it is possible that the dunes of Herschel in some areas are being exposed to winds capable of grooving the dunes over extended periods, but not competent enough to activate saltation over the entire dune. This may still qualify the dunes in question for the label of inactive, but Edgett and Malin (2000) point out that the terms active and inactive are ill defined. Whatever the status of the Herschel dunes, they

are still young features. Where grooves do exist, they are coincident with wind directions derived from the dunes themselves and do not effect the determinations made in this study.

General Circulation Comparisons

Herschel Crater lies in an area between the Martian tropic latitudes (25°N. - 25°S.). This means the subsolar point, the point on a planet at which the Sun is directly overhead, crosses over the location depending on the season. In a simple atmospheric model, the subsolar point causes a pressure low and winds flow toward it. Although a simple model ignores topography, a region that crosses the subsolar point should experience some multi-directional wind flow. Fenton's (2003) GCM reflects this (Figure 28). During Martian southern summer, the Fenton GCM indicates strong winds from the north or just west of north. This correlates with the findings inferred from the geomorphology of winds generally from the north (11°). Differences between the GCM and geomorphic determinations could be explained through topography interactions or the fact that the Fenton GCM is calculated for 200 meters above the surface. During the southern summer at Herschel, the GCM shows winds from the southeast in southern winter and opposing winds from the northwest. The geomorphology does not appear to reflect this direction wind. The fact that multi-directional winds are not reflected in the Herschel region geomorphology could have to do with wind strength. Mars is at perihelion and 17% closer to the Sun during southern summer (Hartmann, 1999). This added solar energy drives circulation and generally strengthens winds. This is indicated

in the GCM for Herschel Crater. In fact, southern summer is dust storm season on Mars. It may be that southern summer is the only time of year winds of formative strength in the Herschel region can occur and thus be reflected in the geomorphology.

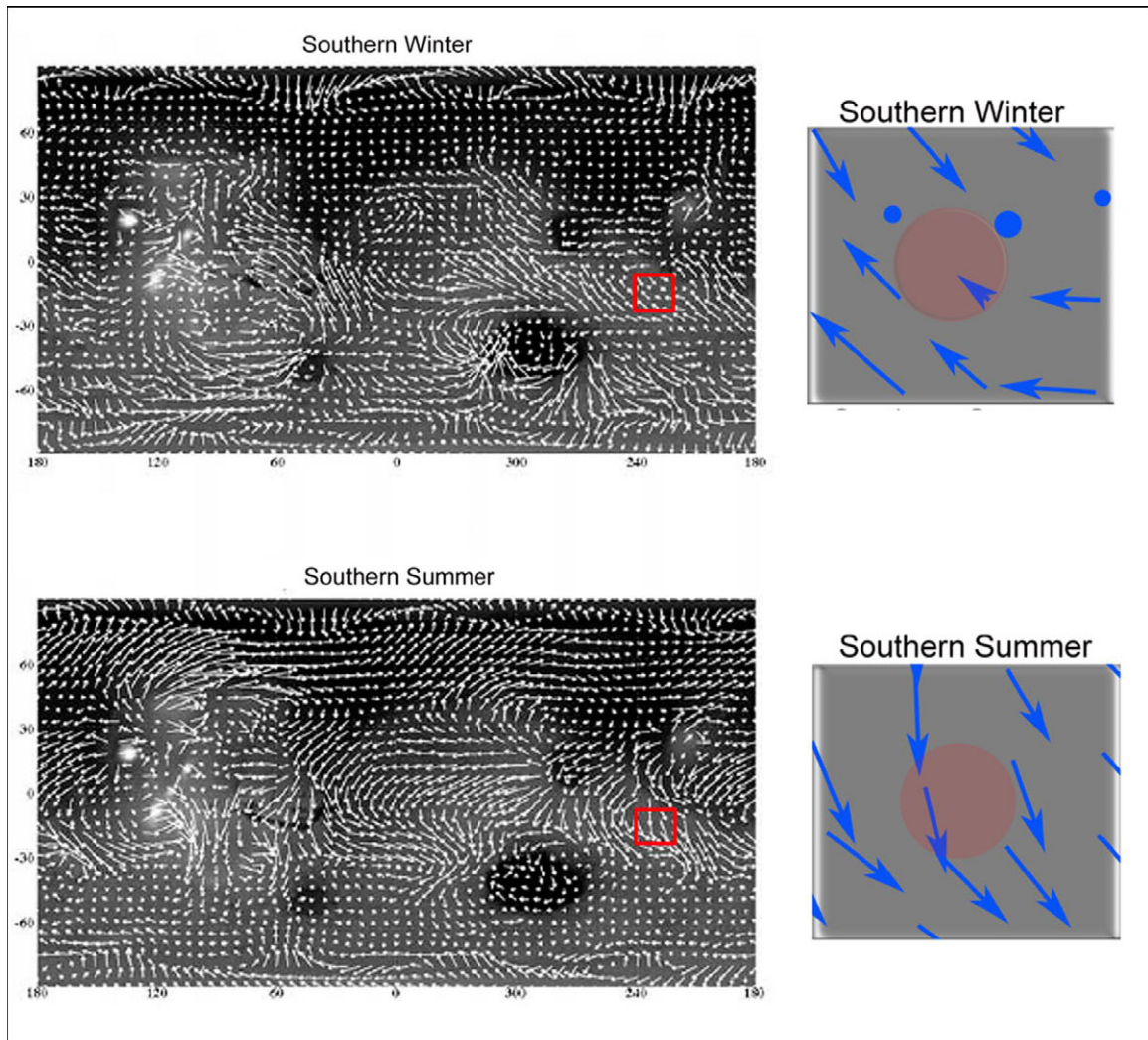


Figure 28. Present-day seasonal average surface winds superimposed on a grayscale MOLA topographic map. Study area is outlined in red with Herschel crater near the center of the box. Diagrams on the right are redrawn to show local GCM predicted wind directions. Modified and redrawn from Fenton, 2003.

CHAPTER V

CONCLUSIONS

Usefulness of Eolian Features Images for Inferring Wind Direction

Very little ground truth exists for Mars in terms of wind characteristics. When one considers that wind is dominate geologic surface process currently at work on Mars, a comprehensive understanding of Martian surface winds is paramount if we are to understand Mars as a planet. It is possible to use eolian features captured in remotely sensed imagery to infer formative wind directions. In this study, eolian features found in MOC NA imagery were used to create a map of formative wind circulation for the Herschel Crater region of Mars. The resulting map indicates formative winds generally from the North in the crater area with winds being deflected along the interior and exterior of the crater rim. This technique could be very useful in regions of Mars as a supplement to ground truth data. The technique assumes that the features measured are recent. An attempt to observe landform change over time could not confirm any. This could be an indication that the area is not being actively modified. However, the data set for studying changes in eolian features through time is small both spatially and temporally.

General Circulation Comparisons

One of the problems with general circulation models (GCM) is that so little ground truth exists for Mars to correlate or validate with. Geomorphic observations like

the ones in this study can supplement ground truth data and be used to validate or improve GCM. In the case of Herschel Crater, the inferred wind directions were compared to a recent GCM and do correlate with predictions for the Martian summer in the area. This correlation is bolstered by the fact that, during the Martian summer, Mars is at perihelion and should experience its strongest, thus formative, winds in the Herschel region. It is important to note that correlation in one region alone can not validate a global model, but does lend support to it.

Future Work

As with any research, investigation often yields further inquiry and insight. Though the MOC NA images represent the best resolution for this type of study, MOC wide angle images also contain eolian features and have greater spatial coverage, if somewhat lower resolution. Incorporating them into the data set would be useful. Future missions to Mars promise image resolution of up to 25 cm/pixel and with the increased time span achieved by comparing them to current mission imagery, dune movement may be detectable. Such movement or change would confirm that the geomorphology reflects current conditions on Mars and not those of the past. This would further validate the techniques used in this study as ground truth supplements.

During this study it was realized that the spatial resolutions of current GCM are not high enough for easy comparison to regions even on the size of Herschel Crater. Further, current global GCM do not incorporate topography effects on wind at a scale reflected in the geomorphology. The author has been in correspondence with Anthony Tiogo about running a Mars MM5 regional circulation model for Herschel Crater. The

improved spatial resolution of the MM5 and its incorporation of higher resolution topography data make it ideal for comparing to geomorphology studies like this one. In turn, studies like this could help in validating such high resolution models.

REFERENCES

- Aharonson, A., Schorghofer, N. and Gerstell, M.F., 2003. Slope streak formation and dust deposition rates on Mars. *Journal of Geophysical Research*, 108(E12): 12-1 - 12-9.
- Bagnold, R.A., 1941. *The Physics of Blown Sand and Desert Dunes*. Butler and Tanner Ltd, London, 265 pp.
- Biener, K.K., Geissler, P.E., McEwen, A.S. and Leovy, C., 2002. Observations of Martian Dust Devils in MOC Wide Angle Camera Images., *Lunar and Planetary Science Conference XXXIII*. Lunar and Planetary Institute, Houston, TX, #2004.
- Blumberg, D.G. and Greeley, R., 1996. A comparison of general circulation model predictions to sand drift and dune orientations. *Journal of Climate*, 9(12): 3248-3259.
- Bourke, M.C., Wilson, S.A. and Zimbelman, J.R., 2003. The Variability of Transverse Aeolian Ridges in Troughs on Mars, *Lunar and Planetary Science Conference XXXIV*. Lunar and Planetary Institute, League City, TX, #2090.
- Breed, C.S., McCauley, J.F. and Whitney, M.I., 1989. Wind erosion forms. In: D.S.G. Thomas (Editor), *Arid Zone Geomorphology*. Halsted Press, New York, pp. 371.
- Caplinger, M.A. and Malin, M.C., 2003. A New Map of Mars, *Lunar and Planetary Science Conference XXXIV*. Lunar and Planetary Institute, League City, TX, #1901.
- Diniega, S., Richardson, M.I., Ewald, S.P., Toigo, A.D. and Byrne, S., 2003. Martian Polar Wind Patterns Derived from Mapping of Seasonal Cap Dark Streaks. In: Lunar and Planetary Institute (Editor), *Lunar and Planetary Science Conference XXXIV*. Lunar and Planetary Institute, League City, TX. #2125.
- Easterbrook, D.J., 1993. *Surface Processes and Land Forms*. Prentice Hall, Upper Saddle River, 546 pp.
- Edgett, K.S. and Malin, M., 2000. New view of Mars eolian activity, materials, and surface properties: Three vignettes from Mars Global Surveyor Mars Orbital Camera. *Journal of Geophysical Research*, 105(E1): 1623-1650.
- Fenton, L.K., 2003. *Aeolian processes on Mars: Atmospheric modeling and GIS analysis*. PhD Dissertation Thesis, California Institute of Technology, Pasadena, 229 pp.

- Fenton, L.K., Bandfield, J.L. and Ward, W.A., 2003. Aeolian processes in Proctor Crater on Mars: Sedimentary history as analyzed from multiple data sets. *Journal of Geophysical Research*, 108(E12): 3-1 - 3-38.
- Fenton, L.K., Richardson, M.I. and Toigo, A.D., 2002. Sand Transport in Proctor Crater on Mars Based on Dune Morphology and Mesoscale Modeling, Lunar and Planetary Science Conference XXXIII. Lunar and Planetary Institute, Houston, TX, #1953.
- Geissler, P.E., McEwen, A.S., Leovy, C. and Biener, K., 2002. Identifying Surface Changes on Mars from Viking and MGS, Lunar and Planetary Science Conference. Lunar and Planetary, Houston, TX, #1982.
- Godwin, R. (Editor), 2000. Mars: The NASA Mission Reports. Space Series, 1. Apogee Books, Ontario, 424 pp.
- Greeley, R. and Guest, J.E., 1987. Geologic map of the eastern equatorial region of Mars, Atlas of Mars. USGS, Denver.
- Greeley, R. and Iversen, J.D., 1985. Winds as a geological process. Cambridge Planetary Science Series. Cambridge University Press, Cambridge, 333 pp.
- Greeley, R., Iversen, J.D., Pollack, J.B., Udovich, N. and White, B., 1974. Wind tunnel studies of Martian eolian processes. *Proceedings of the Royal Society of London. Series A, Mathematical and Physical Sciences*, 341(1626): 331-360.
- Greeley, R., Kraft, R., Sullivan, S., Wilson, G., Bridges, N., Herkenhoff, K., Kuzman, R.O., Malin, M. and Ward, W., 1999. Aeolian features and processes at the Mars Pathfinder landing site. *Journal of Geophysical Research*, 104(E4): 8573-8584.
- Greeley, R., Skyepeck, A. and Pollack, J.B., 1993. Martian aeolian features and deposits: Comparisons with general circulation model results. *Journal of Geophysical Research*, 98(E2): 3183-3196.
- Greeley, R. and Thompson, S.D., 2003. Mars: Aeolian features and wind predictions at the Terra Meridiani and Isidis Planitia potential Mars Exploration Rover landing sites. *Journal of Geophysical Research*, 108(E12): ROV 34-1 - ROV 34-10.
- Greeley, R. and Williams, S.H., 1994. Dust deposits on Mars: The "Parna" analog. *Icarus*, 110: 165-177.
- Haberle, R.M., Murphy, J.R. and Schaeffer, J., 2003. Orbital change experiments with a Mars general circulation model. *Icarus*, 161: 66-89.
- Haberle, R.M., Joshi, M.M., Murphy, J.R., Barnes, J.R., Schofield, J.T., Wilson, G., Lopez-Valverde, M., Hollingsworth, J.L., Bridger, A.F.C. and Schaeffer, J., 1999.

- General circulation model simulation of the Mars Pathfinder atmospheric structure investigation/meteorology data. *Journal of Geophysical Research*, 104(E4): 8957-8974.
- Hartmann, W.K., 1999. *Moons & Planets*. Wadsworth Publishing Company, Belmont, 428 pp.
- Joshi, M.M., Haberle, R.M., Barnes, J.R., Murphy, J.R. and Schaeffer, J., 1997. Low level jets in the NASA Ames Mars general circulation model. *Journal of Geophysical Research*, 102: 6511-6523.
- Kuzman, R.O., Greeley, R., Rafkin, S.C.R. and Haberle, R., 2001. Wind related modification of some small impact craters on Mars. *Icarus*, 153: 61-70.
- Lancaster, N., 1995. *Geomorphology of Desert Dunes*. Routledge Physical Environment Series. Routledge, New York, 290 pp.
- Lewis, S.R., Collins, M. and Read, P.L., 1997. Data assimilation with a Martian atmospheric GCM: An example of using thermal data. *Advances in Space Research*, 19(8): 1267-1270.
- Marrs, R.W. and Gaylord, D.R., 1982. Techniques for interpretation of windflow characteristics from eolian landform. In: R.W. Marrs and K.E. Kolm (Editors), *Interpretation of Windflow Characteristics from Eolian Landforms*. Geological Society of America, Boulder, pp. 109.
- Metzger, S.M., 2003. Promoting a Well Established Study Site for Mars Analog and Desert Process Studies, Lunar and Planetary Science Conference. Lunar and Planetary Institute, League City, TX, #2048.
- Möller, L.E., Kuhlman, K.R., Marshall, J.R. and Towner, M.C., 2002. The Snoopy Angle of Repose Experiment: Calibration of an Instrument to Determine the Angle of repose of Martian Dust, Lunar and Planetary Science Conference XXXIII. Lunar and Planetary Institute, Houston, TX, #2015.
- Neakrase, L.D.V. and Greeley, R., 2002. Mars Polar Wind Streaks as Sublimation-Aided Wind Indicators, Lunar and Planetary Science Conference XXXIII. Lunar and Planetary Institute, Houston, TX, #1378.
- Ringrose, T.J. and Zarnecki, J.C., 2002. Martian and Terrestrial Dust Devils, Lunar and Planetary Science Conference XXXIII. Lunar and Planetary Institute, Houston, TX, #1183.
- Shao, Y., 2000. *Physics and Modeling of Wind Erosion*. Kluwer Academic Publishers, Dordrecht, 393 pp.

- Sheehan, W., 1996. *The Planet Mars: A History of Observation and Discovery*. The University of Arizona Press, Tucson, 270 pp.
- Stanley, B.D., Adcock, C.T. and Marston, R.A., 2004. Interpretation of Wind Direction from Eolian Features: Herschel Crater, Mars, Lunar and Planetary Science Conference XXXV. Lunar and Planetary Institute, League City, TX, #1307.
- Sullivan, R., Thomas, P., Veverka, J., Malin, M. and Edgett, K.S., 2001. Mass movement slope streaks imaged by the Mars Orbital Camera. *Journal of Geophysical Research*, 106(E10): 23,607-23,633.
- Tanaka, K.L., Scott, D.H. and Greeley, R., 1992. Global Stratigraphy. In: H.H. Kieffer, B.M. Jokosky, C.W. Snyder and M.S. Matthews (Editors), *Mars. Space Science Series*. University of Arizona Press, Tucson, pp. 1498.
- Thomas, D.S.G., 1989. *Arid Zone Geomorphology*. Jon Wiley and Sons, New York, 372 pp.
- Thomas, P. and Veverka, J., 1979. Seasonal and secular variation of wind streaks on Mars: An analysis of Mariner 9 and Viking data. *Journal of Geophysical Research*, 84(B14): 8131-8146.
- Thomas, P., Veverka, J., Lee, S. and Bloom, A., 1981. Classification of wind streaks on Mars. *Icarus*, 45(1): 124-153.
- Thomas, P.C., Malin, M.C., Carr, M.H., Danielson, G.E., Davies, M.E., Hartmann, W.K., Ingersoll, A.P., James, P.B., McEwen, A.S., Soderblom, L.A. and Veverka, J., 1999. Bright dunes on Mars. *Nature*, 397: 592-594.
- Tiogo, A.D. and Richardson, M.I., 2002. A mesoscale model for the Martian atmosphere. *Journal of Geophysical Research*, 107(E7): 3-1 to 3-21.
- Walker, A.S., 1986. Eolian Landforms. In: N.M. Short and R.W. Blair (Editors), *Geomorphology From Space*. NASA.
- Whelley, P.L., Balme, M.R. and Greeley, R., 2003. Mars: Dust Devil Tracks in Hellas Basin and Argyre Planitia, Lunar and Planetary Science Conference XXXIV. Lunar and Planetary Institute, League City, TX, #1769.
- Williams, K.K., Greeley, R. and Zimbelman, J.R., 2003. Using Overlapping MOC Images to Search for Dune Movement and to Measure Dune Heights, Lunar and Planetary Science Conference XXXIV. Lunar and Planetary Institute, League City, TX, #1639.

APPENDIX A

MOC NA IMAGES USED

Catalog of images and meta-data from Malin Space Science Systems (MSSS). Image captions are from MSSS.

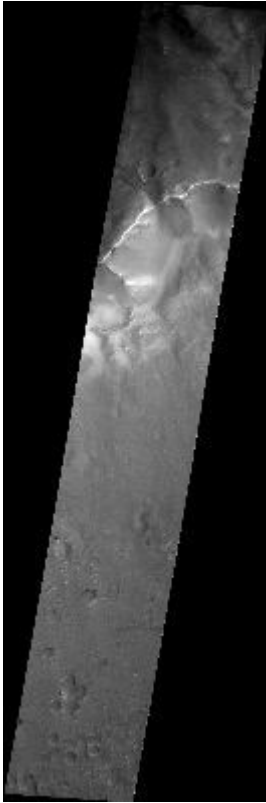


Figure A-1. SP2-36506 – Traverse north rim of Herschel Crater basin.

Ancillary data for MOC narrow-angle image SP2-36506

Acquisition parameters

Image ID (picno): SP2-36506
 Image start time: 1998-06-14T17:50:17.50 SCET
 Image width: 512 pixels
 Image height: 3200 pixels
 Line integration time: 4.8800 millisecc
 Pixel aspect ratio: 1.01
 Crosstrack summing: 1
 Downtrack summing: 1
 Compression type: PREDICTIVE-221
 Gain mode: CA (hexadecimal)
 Offset mode: 19 (decimal)

Derived values

Longitude of image center: 231.73°W
 Latitude of image center: 12.73°S
 Scaled pixel width: 10.37 meters
 Scaled image width: 5.30 km
 Scaled image height: 33.31 km
 Solar longitude (Ls): 344.62°
 Local True Solar Time: 7.77 decimal hours
 Emission angle: 26.08°
 Incidence angle: 65.62°
 Phase angle: 67.48°
 North azimuth: 266.02°
 Sun azimuth: 357.43°
 Spacecraft altitude: 2602.49 km
 Slant distance: 2758.60 km

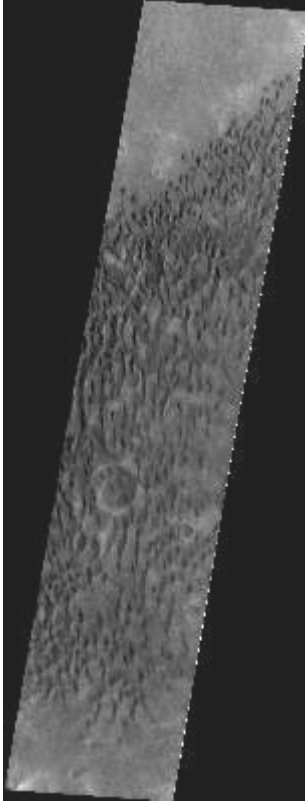


Figure A-2. SP2-36507 – Low albedo dunes in Herschel Crater basin.

Ancillary data for MOC narrow-angle image SP2-36507

Acquisition parameters

Image ID (picno): SP2-36507
 Image start time: 1998-06-14T17:51:04.80 SCET
 Image width: 512 pixels
 Image height: 2432 pixels
 Line integration time: 5.2400 millisecc
 Pixel aspect ratio: 1.03
 Crosstrack summing: 1
 Downtrack summing: 1
 Compression type: PREDICTIVE-221
 Gain mode: AA (hexadecimal)
 Offset mode: 20 (decimal)

Derived values

Longitude of image center: 232.02°W
 Latitude of image center: 14.33°S
 Scaled pixel width: 10.72 meters
 Scaled image width: 5.48 km
 Scaled image height: 26.22 km
 Solar longitude (Ls): 344.63°
 Local True Solar Time: 7.76 decimal hours
 Emission angle: 26.53°
 Incidence angle: 65.70°
 Phase angle: 67.30°
 North azimuth: 266.00°
 Sun azimuth: 356.71°
 Spacecraft altitude: 2689.28 km
 Slant distance: 2853.87 km



Figure A-3. FHA-00437 - dark material on Herschel basin floor

Ancillary data for MOC narrow-angle image FHA-00437

Acquisition parameters

Image ID (picno): FHA-00437
Image start time: 1999-03-09T03:06:17.75 SCET
Image width: 2048 pixels
Image height: 2048 pixels
Line integration time: 0.4821 millisecc
Pixel aspect ratio: 1.04
Crosstrack summing: 1
Downtrack summing: 1
Compression type: MOC-PRED-X-5
Gain mode: 0A (hexadecimal)
Offset mode: 14 (decimal)

Derived values

Longitude of image center: 232.54°W
Latitude of image center: 15.40°S
Scaled pixel width: 1.43 meters
Scaled image width: 2.93 km
Scaled image height: 3.04 km
Solar longitude (Ls): 107.32°
Local True Solar Time: 14.43 decimal hours
Emission angle: 0.07°
Incidence angle: 53.11°
Phase angle: 53.17°
North azimuth: 93.05°
Sun azimuth: 50.25°
Spacecraft altitude: 380.52 km
Slant distance: 380.52 km



Figure A-4. FHA-00583 - surface immediately north of Herschel Basin rim

Ancillary data for MOC narrow-angle image FHA-00583

Acquisition parameters

Image ID (picno): FHA-00583
 Image start time: 1999-03-11T04:08:51.94 SCET
 Image width: 1024 pixels
 Image height: 3840 pixels
 Line integration time: 0.4821 millisecond
 Pixel aspect ratio: 1.04
 Crosstrack summing: 1
 Downtrack summing: 1
 Compression type: MOC-PRED-X-5
 Gain mode: 0A (hexadecimal)
 Offset mode: 28 (decimal)

Eolian Features

Number of Features Analyzed:
 Average Wind Direction:
 Note:

Derived values

Longitude of image center: 228.65°W
 Latitude of image center: 12.98°S
 Scaled pixel width: 1.43 meters
 Scaled image width: 1.47 km
 Scaled image height: 5.71 km
 Solar longitude (Ls): 108.25°
 Local True Solar Time: 14.42 decimal hours
 Emission angle: 0.16°
 Incidence angle: 51.21°
 Phase angle: 51.36°
 North azimuth: 93.01°
 Sun azimuth: 48.86°
 Spacecraft altitude: 381.77 km
 Slant distance: 381.77 km



Figure A-5. FHA-00914 - dark floor and central peak in crater on SW rim of Herschel Basin

Ancillary data for MOC narrow-angle image FHA-00914

Acquisition parameters

Image ID (picno): FHA-00914
 Image start time: 1999-03-16T07:41:00.10 SCET
 Image width: 768 pixels
 Image height: 6528 pixels
 Line integration time: 0.4821 millisecc
 Pixel aspect ratio: 1.04
 Crosstrack summing: 2
 Downtrack summing: 2
 Compression type: MOC-PRED-X-5
 Gain mode: 0A (hexadecimal)
 Offset mode: 30 (decimal)

BAD IMAGE

Derived values

Longitude of image center: 231.91°W
 Latitude of image center: 16.64°S
 Scaled pixel width: 2.86 meters
 Scaled image width: 2.19 km
 Scaled image height: 19.42 km
 Solar longitude (Ls): 110.59°
 Local True Solar Time: 14.44 decimal hours
 Emission angle: 0.06°
 Incidence angle: 53.85°
 Phase angle: 53.90°
 North azimuth: 93.06°
 Sun azimuth: 50.22°
 Spacecraft altitude: 380.14 km
 Slant distance: 380.14 km

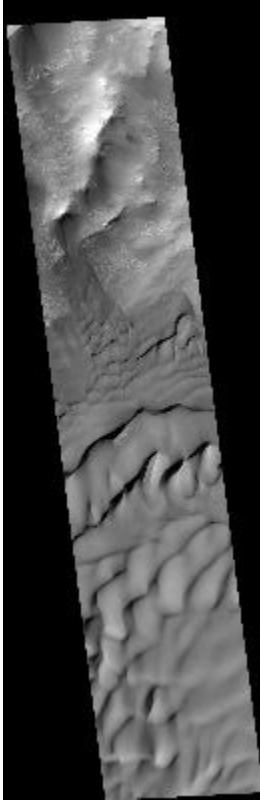


Figure A-6. FHA-01381 - dark material and crater wall within Herschel Basin

Ancillary data for MOC narrow-angle image FHA-01381

Acquisition parameters

Image ID (picno): FHA-01381
 Image start time: 1999-03-23T12:16:51.51 SCET
 Image width: 1024 pixels
 Image height: 3328 pixels
 Line integration time: 0.7231 millisecc
 Pixel aspect ratio: 1.56
 Crosstrack summing: 2
 Downtrack summing: 2
 Compression type: MOC-PRED-X-5
 Gain mode: 0A (hexadecimal)
 Offset mode: 14 (decimal)

Derived values

Longitude of image center: 231.74°W
 Latitude of image center: 14.44°S
 Scaled pixel width: 2.85 meters
 Scaled image width: 2.92 km
 Scaled image height: 14.85 km
 Solar longitude (Ls): 113.89°
 Local True Solar Time: 14.45 decimal hours
 Emission angle: 0.00°
 Incidence angle: 51.93°
 Phase angle: 51.93°
 North azimuth: 93.04°
 Sun azimuth: 48.45°
 Spacecraft altitude: 379.60 km
 Slant distance: 379.60 km



Figure A-7. M00-00790 - Dark floor material within Herschel Basin

Ancillary data for MOC narrow-angle image M00-00790

Acquisition parameters

Image ID (picno): M00-00790
 Image start time: 1999-04-06T21:26:32.56 SCET
 Image width: 1024 pixels
 Image height: 5632 pixels
 Line integration time: 0.4821 millisecc
 Pixel aspect ratio: 1.06
 Crosstrack summing: 2
 Downtrack summing: 2
 Compression type: MOC-PRED-X-5
 Gain mode: 0A (hexadecimal)
 Offset mode: 2 (decimal)

Derived values

Longitude of image center: 230.66°W
 Latitude of image center: 14.68°S
 Scaled pixel width: 2.82 meters
 Scaled image width: 2.89 km
 Scaled image height: 16.79 km
 Solar longitude (Ls): 120.58°
 Local True Solar Time: 14.48 decimal hours
 Emission angle: 0.21°
 Incidence angle: 51.47°
 Phase angle: 51.36°
 North azimuth: 93.10°
 Sun azimuth: 46.96°
 Spacecraft altitude: 375.38 km
 Slant distance: 375.38 km



Figure A-8. M00-03222 - North edge of dark spot in eastern Herschel Crater

Ancillary data for MOC narrow-angle image M00-03222

Acquisition parameters

Image ID (picno): M00-03222
 Image start time: 1999-05-05T15:45:42.92 SCET
 Image width: 1024 pixels
 Image height: 4480 pixels
 Line integration time: 0.7231 millisecc
 Pixel aspect ratio: 1.57
 Crosstrack summing: 1
 Downtrack summing: 1
 Compression type: MOC-PRED-X-5
 Gain mode: 0A (hexadecimal)
 Offset mode: 16 (decimal)

Derived values

Longitude of image center: 228.44°W
 Latitude of image center: 15.36°S
 Scaled pixel width: 1.42 meters
 Scaled image width: 1.45 km
 Scaled image height: 10.00 km
 Solar longitude (Ls): 134.32°
 Local True Solar Time: 14.55 decimal hours
 Emission angle: 0.12°
 Incidence angle: 50.21°
 Phase angle: 50.30°
 North azimuth: 93.04°
 Sun azimuth: 42.81°
 Spacecraft altitude: 377.57 km
 Slant distance: 377.57 km

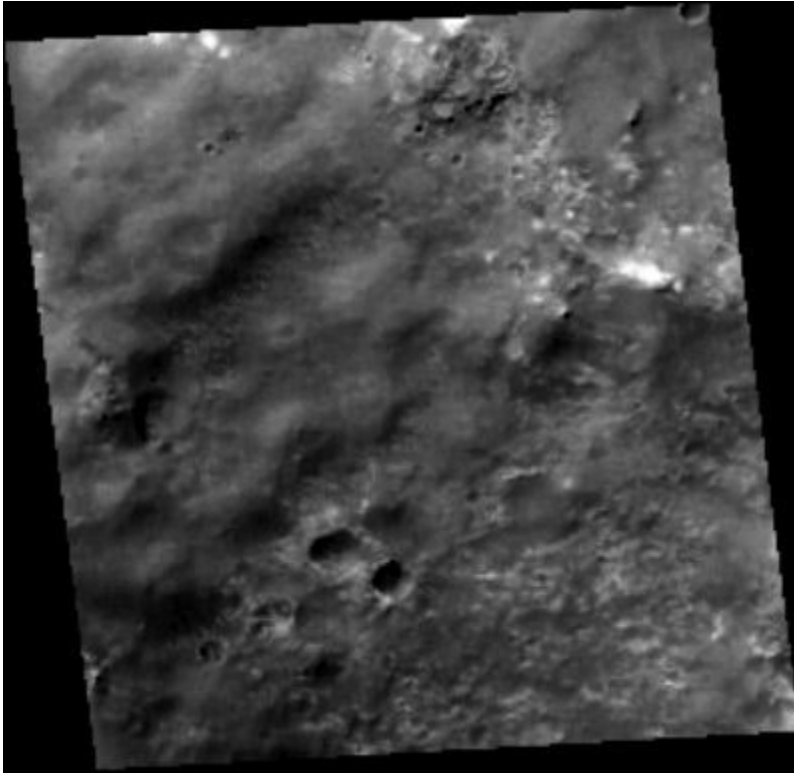


Figure A-9. M01-03831- Science Campaign A (Geodesy)

Ancillary data for MOC narrow-angle image M01-03831

Acquisition parameters

Image ID (picno): M01-03831
 Image start time: 1999-05-25T04:29:01.98 SCET
 Image width: 256 pixels
 Image height: 256 pixels
 Line integration time: 0.4821 millisecc
 Pixel aspect ratio: 1.05
 Crosstrack summing: 8
 Downtrack summing: 8
 Compression type: MOC-NONE
 Gain mode: 8A (hexadecimal)
 Offset mode: 26 (decimal)

Derived values

Longitude of image center: 231.21°W
 Latitude of image center: 14.72°S
 Scaled pixel width: 11.33 meters
 Scaled image width: 2.89 km
 Scaled image height: 3.04 km
 Solar longitude (Ls): 143.98°
 Local True Solar Time: 14.60 decimal hours
 Emission angle: 0.22°
 Incidence angle: 48.40°
 Phase angle: 48.26°
 North azimuth: 93.16°
 Sun azimuth: 38.56°
 Spacecraft altitude: 376.93 km
 Slant distance: 376.94 km

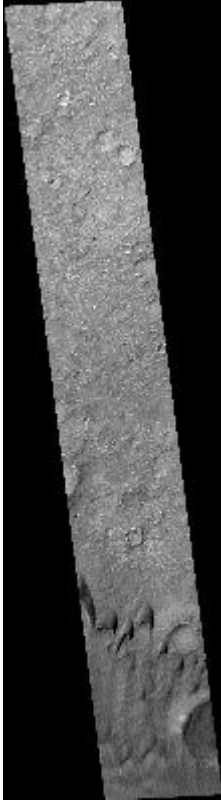


Figure A-10. M02-00612 - Dark material in Herschel Basin in contact with bright upland

Ancillary data for MOC narrow-angle image M02-00612

Acquisition parameters

Image ID (picno): M02-00612
 Image start time: 1999-06-08T13:38:36.15 SCET
 Image width: 1024 pixels
 Image height: 4480 pixels
 Line integration time: 0.7231 millisecc
 Pixel aspect ratio: 1.57
 Crosstrack summing: 1
 Downtrack summing: 1
 Compression type: MOC-PRED-X-5
 Gain mode: 0A (hexadecimal)
 Offset mode: 20 (decimal)

Derived values

Longitude of image center: 230.16°W
 Latitude of image center: 14.21°S
 Scaled pixel width: 1.42 meters
 Scaled image width: 1.45 km
 Scaled image height: 10.00 km
 Solar longitude (Ls): 151.29°
 Local True Solar Time: 14.63 decimal hours
 Emission angle: 0.25°
 Incidence angle: 47.00°
 Phase angle: 46.98°
 North azimuth: 93.11°
 Sun azimuth: 34.74°
 Spacecraft altitude: 377.74 km
 Slant distance: 377.74 km

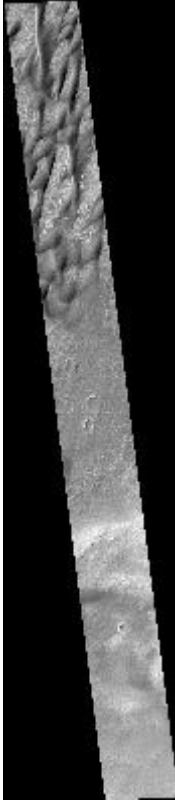


Figure A-11. M02-01996 - Contact between dark and lighter-toned floor material SE Herschel

Ancillary data for MOC narrow-angle image M02-01996

Acquisition parameters

Image ID (picno): M02-01996
 Image start time: 1999-06-15T18:11:24.84 SCET
 Image width: 768 pixels
 Image height: 5376 pixels
 Line integration time: 0.7231 millisecc
 Pixel aspect ratio: 1.58
 Crosstrack summing: 1
 Downtrack summing: 1
 Compression type: MOC-PRED-X-5
 Gain mode: 0A (hexadecimal)
 Offset mode: 20 (decimal)

Derived values

Longitude of image center: 229.04°W
 Latitude of image center: 15.87°S
 Scaled pixel width: 1.41 meters
 Scaled image width: 1.09 km
 Scaled image height: 12.01 km
 Solar longitude (Ls): 155.01°
 Local True Solar Time: 14.65 decimal hours
 Emission angle: 0.26°
 Incidence angle: 47.36°
 Phase angle: 47.37°
 North azimuth: 93.14°
 Sun azimuth: 34.18°
 Spacecraft altitude: 376.57 km
 Slant distance: 376.57 km



Figure A-12. M02-01998 - Sample terrain immediately N of Herschel rim

Ancillary data for MOC narrow-angle image M02-01998	
Acquisition parameters	Derived values
Image ID (picno): M02-01998	No DUNES
Image start time: 1999-06-15T18:12:36.97 SCET	Longitude of image center: 229.50°W
Image width: 1024 pixels	Latitude of image center: 12.16°S
Image height: 3968 pixels	Scaled pixel width: 1.42 meters
Line integration time: 0.7231 millisc	Scaled image width: 1.45 km
Pixel aspect ratio: 1.57	Scaled image height: 8.86 km
Crosstrack summing: 1	Solar longitude (Ls): 155.01°
Downtrack summing: 1	Local True Solar Time: 14.64 decimal hours
Compression type: MOC-PRED-X-5	Emission angle: 0.24°
Gain mode: 0A (hexadecimal)	Incidence angle: 45.39°
Offset mode: 42 (decimal)	Phase angle: 45.17°
	North azimuth: 93.10°
	Sun azimuth: 31.18°
	Spacecraft altitude: 378.00 km
	Slant distance: 378.01 km

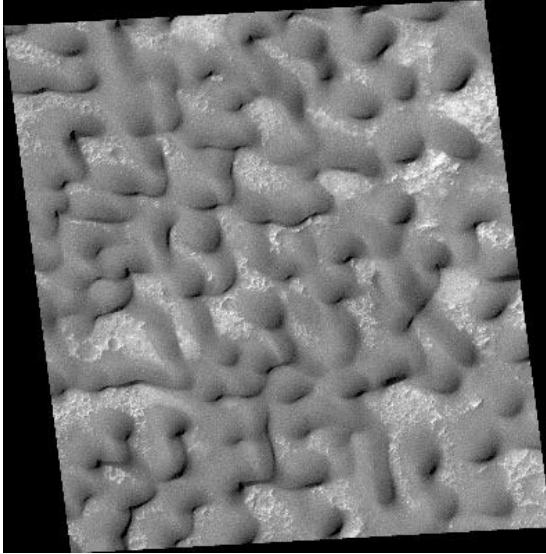


Figure A-13. M02-02819 - dark material at SW side of Herschel Basin floor

Ancillary data for MOC narrow-angle image M02-02819

Acquisition parameters

Image ID (picno): M02-02819
 Image start time: 1999-06-20T21:43:22.74 SCET
 Image width: 2048 pixels
 Image height: 2176 pixels
 Line integration time: 0.4821 millisecc
 Pixel aspect ratio: 1.05
 Crosstrack summing: 1
 Downtrack summing: 1
 Compression type: MOC-PRED-X-5
 Gain mode: 0A (hexadecimal)
 Offset mode: 8 (decimal)

Derived values

Longitude of image center: 232.48°W
 Latitude of image center: 15.12°S
 Scaled pixel width: 1.42 meters
 Scaled image width: 2.90 km
 Scaled image height: 3.24 km
 Solar longitude (Ls): 157.70°
 Local True Solar Time: 14.66 decimal hours
 Emission angle: 0.22°
 Incidence angle: 46.55°
 Phase angle: 46.42°
 North azimuth: 93.14°
 Sun azimuth: 32.23°
 Spacecraft altitude: 376.86 km
 Slant distance: 376.87 km

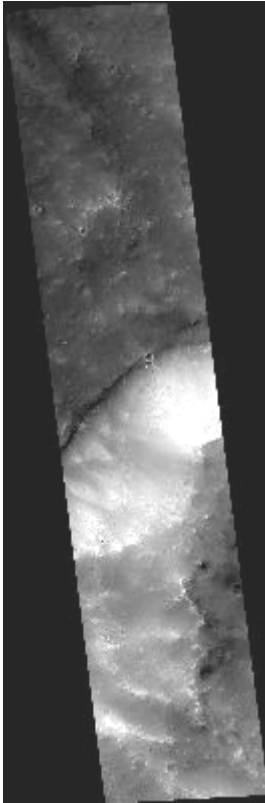


Figure A-14. M02-03305 - SE wall of Herschel Basin

Ancillary data for MOC narrow-angle image M02-03305

Acquisition parameters

Image ID (picno): M02-03305
 Image start time: 1999-06-22T22:44:17.52 SCET
 Image width: 1024 pixels
 Image height: 3200 pixels
 Line integration time: 0.7231 millisecc
 Pixel aspect ratio: 1.58
 Crosstrack summing: 2
 Downtrack summing: 2
 Compression type: MOC-PRED-X-5
 Gain mode: 2A (hexadecimal)
 Offset mode: 36 (decimal)

Derived values

Longitude of image center: 228.02°W
 Latitude of image center: 15.69°S
 Scaled pixel width: 2.83 meters
 Scaled image width: 2.90 km
 Scaled image height: 14.30 km
 Solar longitude (Ls): 158.78°
 Local True Solar Time: 14.67 decimal hours
 Emission angle: 0.21°
 Incidence angle: 46.68°
 Phase angle: 46.57°
 North azimuth: 93.12°
 Sun azimuth: 32.11°
 Spacecraft altitude: 376.89 km
 Slant distance: 376.90 km

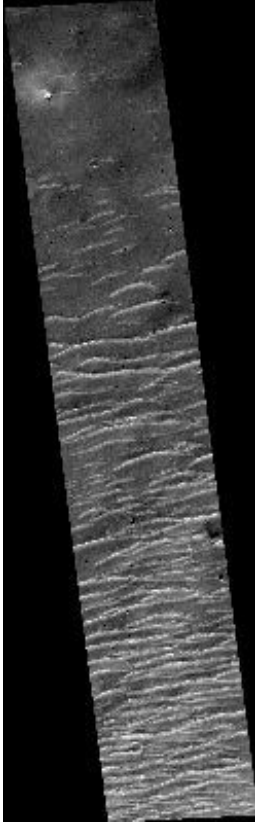


Figure A-15. M03-02054 - Small bright ridges near Herschel

Ancillary data for MOC narrow-angle image M03-02054

Acquisition parameters

Image ID (picno): M03-02054
 Image start time: 1999-07-12T11:22:13.21 SCET
 Image width: 1024 pixels
 Image height: 3584 pixels
 Line integration time: 0.7231 millisecc
 Pixel aspect ratio: 1.57
 Crosstrack summing: 1
 Downtrack summing: 1
 Compression type: MOC-PRED-X-5
 Gain mode: 2A (hexadecimal)
 Offset mode: 28 (decimal)

Eolian Features

Number of Features Analyzed: NONE
 Average Wind Direction: NONE
 Note: NONE

Derived values

Longitude of image center: 229.66°W
 Latitude of image center: 12.09°S
 Scaled pixel width: 1.42 meters
 Scaled image width: 1.45 km
 Scaled image height: 8.00 km
 Solar longitude (Ls): 169.25°
 Local True Solar Time: 14.69 decimal hours
 Emission angle: 0.24°
 Incidence angle: 43.55°
 Phase angle: 43.57°
 North azimuth: 93.05°
 Sun azimuth: 23.11°
 Spacecraft altitude: 378.20 km
 Slant distance: 378.21 km

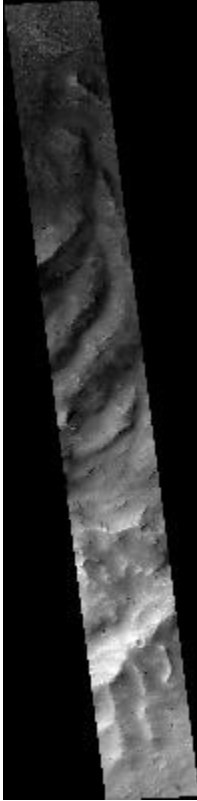


Figure A-16. M03-03634 - Traverse across crater rim that looks like small gullied mountain

Ancillary data for MOC narrow-angle image M03-03634

Acquisition parameters

Image ID (picno): M03-03634
 Image start time: 1999-07-19T15:54:30.19 SCET
 Image width: 1024 pixels
 Image height: 5632 pixels
 Line integration time: 0.7231 millisc
 Pixel aspect ratio: 1.57
 Crosstrack summing: 2
 Downtrack summing: 2
 Compression type: MOC-PRED-X-5
 Gain mode: 4A (hexadecimal)
 Offset mode: 38 (decimal)

Derived values

Longitude of image center: 228.49°W
 Latitude of image center: 12.25°S
 Scaled pixel width: 2.84 meters
 Scaled image width: 2.91 km
 Scaled image height: 25.15 km
 Solar longitude (Ls): 173.19°
 Local True Solar Time: 14.70 decimal hours
 Emission angle: 0.23°
 Incidence angle: 43.15°
 Phase angle: 43.05°
 North azimuth: 93.08°
 Sun azimuth: 20.95°
 Spacecraft altitude: 377.88 km
 Slant distance: 377.89 km

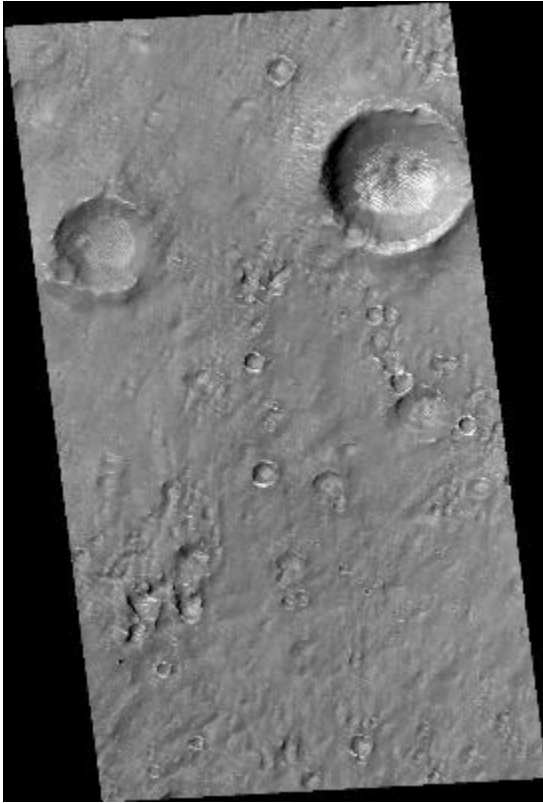


Figure A-17. M04-02035 - Brighter materials in Herschel crater

Ancillary data for MOC narrow-angle image M04-02035

Acquisition parameters

Image ID (picno): M04-02035
 Image start time: 1999-08-20T12:34:38.33 SCET
 Image width: 1024 pixels
 Image height: 1152 pixels
 Line integration time: 0.7231 millisecond
 Pixel aspect ratio: 1.58
 Crosstrack summing: 2
 Downtrack summing: 2
 Compression type: MOC-PRED-X-5
 Gain mode: 6A (hexadecimal)
 Offset mode: 28 (decimal)

Derived values

Longitude of image center: 231.60°W
 Latitude of image center: 13.44°S
 Scaled pixel width: 2.84 meters
 Scaled image width: 2.90 km
 Scaled image height: 5.16 km
 Solar longitude (Ls): 191.27°
 Local True Solar Time: 14.73 decimal hours
 Emission angle: 0.20°
 Incidence angle: 41.34°
 Phase angle: 41.27°
 North azimuth: 93.13°
 Sun azimuth: 11.30°
 Spacecraft altitude: 377.55 km
 Slant distance: 377.55 km

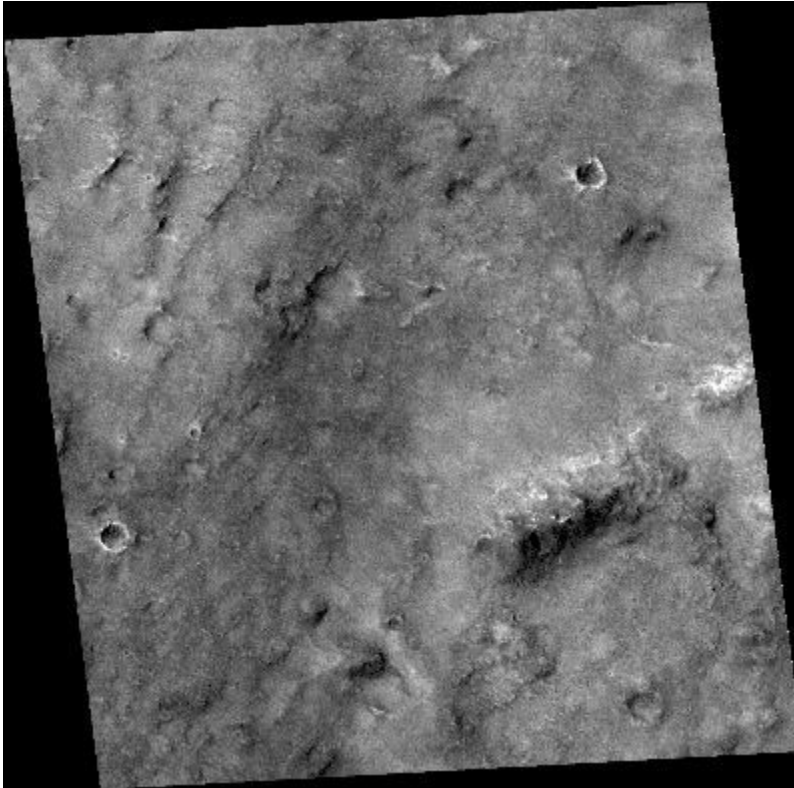


Figure A-18. M04-03624 - dark floor of Herschel

Ancillary data for MOC narrow-angle image M04-03624

Acquisition parameters

Image ID (picno): M04-03624
 Image start time: 1999-08-27T17:07:39.92 SCET
 Image width: 2048 pixels
 Image height: 1408 pixels
 Line integration time: 0.7231 millisecond
 Pixel aspect ratio: 1.58
 Crosstrack summing: 1
 Downtrack summing: 1
 Compression type: MOC-PRED-X-5
 Gain mode: 0A (hexadecimal)
 Offset mode: 24 (decimal)

Derived values

Longitude of image center: 230.55°W
 Latitude of image center: 14.72°S
 Scaled pixel width: 1.42 meters
 Scaled image width: 2.90 km
 Scaled image height: 3.14 km
 Solar longitude (Ls): 195.47°
 Local True Solar Time: 14.73 decimal hours
 Emission angle: 0.20°
 Incidence angle: 41.04°
 Phase angle: 40.97°
 North azimuth: 93.13°
 Sun azimuth: 10.19°
 Spacecraft altitude: 377.17 km
 Slant distance: 377.17 km

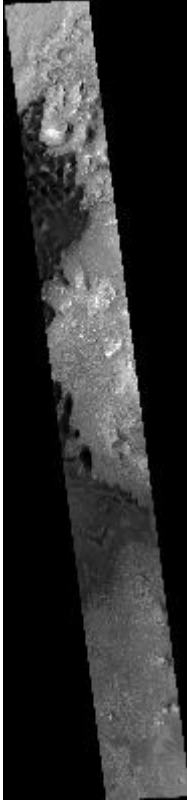


Figure A-19. M07-02974 - Dune field in crater on SW rim of Herschel Basin

Ancillary data for MOC narrow-angle image M07-02974	
Acquisition parameters	Derived values
Image ID (picno): M07-02974	Longitude of image center: 231.94°W
Image start time: 1999-09-16T05:45:47.11 SCET	Latitude of image center: 16.65°S
Image width: 672 pixels	Scaled pixel width: 4.24 meters
Image height: 6144 pixels	Scaled image width: 2.85 km
Line integration time: 0.4821 millisecc	Scaled image height: 27.46 km
Pixel aspect ratio: 1.05	Solar longitude (Ls): 207.13°
Crosstrack summing: 3	Local True Solar Time: 14.69 decimal hours
Downtrack summing: 3	Emission angle: 0.20°
Compression type: MOC-PRED-X-5	Incidence angle: 39.60°
Gain mode: 4A (hexadecimal)	Phase angle: 39.58°
Offset mode: 28 (decimal)	North azimuth: 93.11°
	Sun azimuth: 5.60°
	Spacecraft altitude: 376.50 km
	Slant distance: 376.51 km

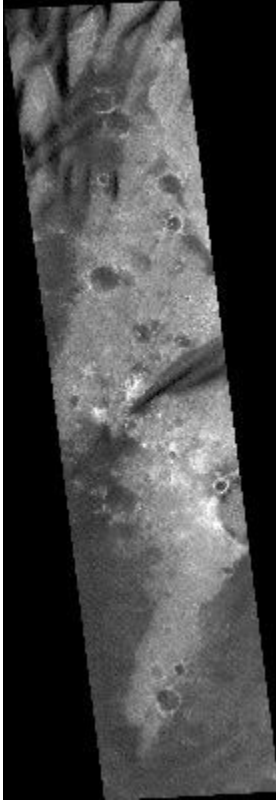


Figure A-20. M07-01919 - Sample dark surface in southeastern Herschel Basin

Ancillary data for MOC narrow-angle image M07-01919	
Acquisition parameters	Derived values
Image ID (picno): M07-01919	Longitude of image center: 228.66°W
Image start time: 1999-09-11T02:14:07.87 SCET	Latitude of image center: 15.60°S
Image width: 1024 pixels	Scaled pixel width: 1.42 meters
Image height: 4480 pixels	Scaled image width: 1.45 km
Line integration time: 0.4821 millisecc	Scaled image height: 6.67 km
Pixel aspect ratio: 1.05	Solar longitude (Ls): 204.03°
Crosstrack summing: 1	Local True Solar Time: 14.70 decimal hours
Downtrack summing: 1	Emission angle: 0.23°
Compression type: MOC-PRED-X-5	Incidence angle: 39.95°
Gain mode: 0A (hexadecimal)	Phase angle: 40.04°
Offset mode: 16 (decimal)	North azimuth: 93.07°
	Sun azimuth: 6.11°
	Spacecraft altitude: 377.08 km
	Slant distance: 377.08 km



Figure A-21. M07-05959 - High resolution traverse across central Herschel Basin floor

Ancillary data for MOC narrow-angle image M07-05959	
Acquisition parameters	Derived values
Image ID (picno): M07-05959	Longitude of image center: 230.43°W
Image start time: 1999-09-30T14:53:06.47 SCET	Latitude of image center: 14.34°S
Image width: 512 pixels	Scaled pixel width: 1.42 meters
Image height: 13824 pixels	Scaled image width: 0.72 km
Line integration time: 0.7231 millisecc	Scaled image height: 30.90 km
Pixel aspect ratio: 1.58	Solar longitude (Ls): 215.91°
Crosstrack summing: 1	Local True Solar Time: 14.63 decimal hours
Downtrack summing: 1	Emission angle: 0.25°
Compression type: MOC-PRED-X-5	Incidence angle: 38.20°
Gain mode: 0A (hexadecimal)	Phase angle: 38.37°
Offset mode: 26 (decimal)	North azimuth: 93.03°
	Sun azimuth: 357.75°
	Spacecraft altitude: 377.16 km
	Slant distance: 377.17 km

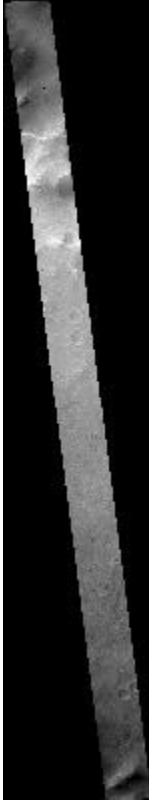


Figure A-22. M08-03208 - Sample terrain along NE Herschel Basin rim

Ancillary data for MOC narrow-angle image M08-03208	
Acquisition parameters	Derived values
Image ID (picno): M08-03208	Longitude of image center: 228.75°W
Image start time: 1999-10-15T00:00:00.38 SCET	Latitude of image center: 12.84°S
Image width: 512 pixels	Scaled pixel width: 2.84 meters
Image height: 8960 pixels	Scaled image width: 1.45 km
Line integration time: 0.4821 millisecc	Scaled image height: 26.69 km
Pixel aspect ratio: 1.05	Solar longitude (Ls): 224.82°
Crosstrack summing: 2	Local True Solar Time: 14.54 decimal hours
Downtrack summing: 2	Emission angle: 0.12°
Compression type: MOC-PRED-X-5	Incidence angle: 37.10°
Gain mode: 4A (hexadecimal)	Phase angle: 37.22°
Offset mode: 34 (decimal)	North azimuth: 93.02°
	Sun azimuth: 350.96°
	Spacecraft altitude: 377.84 km
	Slant distance: 377.84 km



Figure A-23. M08-06611 - light/dark margin within Herschel Basin

Ancillary data for MOC narrow-angle image M08-06611	
Acquisition parameters	Derived values
Image ID (picno): M08-06611	Longitude of image center: 231.00°W
Image start time: 1999-10-27T08:04:39.56 SCET	Latitude of image center: 14.20°S
Image width: 672 pixels	Scaled pixel width: 4.25 meters
Image height: 2432 pixels	Scaled image width: 2.86 km
Line integration time: 0.7231 millisecc	Scaled image height: 16.31 km
Pixel aspect ratio: 1.58	Solar longitude (Ls): 232.55°
Crosstrack summing: 3	Local True Solar Time: 14.46 decimal hours
Downtrack summing: 3	Emission angle: 0.17°
Compression type: MOC-PRED-X-5	Incidence angle: 35.70°
Gain mode: 6A (hexadecimal)	Phase angle: 35.73°
Offset mode: 38 (decimal)	North azimuth: 93.00°
	Sun azimuth: 348.81°
	Spacecraft altitude: 377.38 km
	Slant distance: 377.38 km

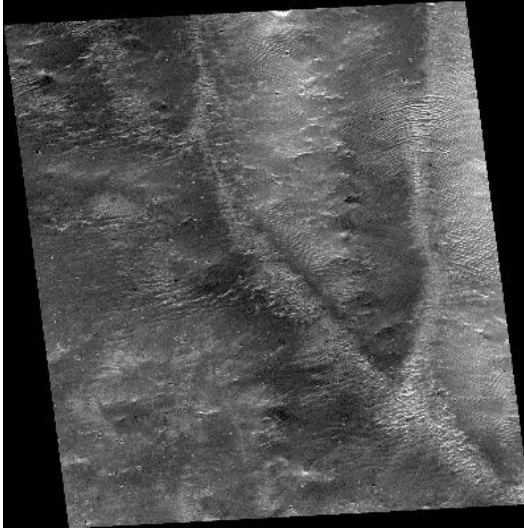


Figure A-24. M09-00699 - North wall of Herschel Basin

Ancillary data for MOC narrow-angle image M09-00699	
Acquisition parameters	Derived values
Image ID (picno): M09-00699	Longitude of image center: 230.30°W
Image start time: 1999-11-03T12:38:26.73 SCET	Latitude of image center: 12.27°S
Image width: 2048 pixels	Scaled pixel width: 1.42 meters
Image height: 2176 pixels	Scaled image width: 2.91 km
Line integration time: 0.4821 millisecc	Scaled image height: 3.24 km
Pixel aspect ratio: 1.05	Solar longitude (Ls): 237.08°
Crosstrack summing: 1	Local True Solar Time: 14.39 decimal hours
Downtrack summing: 1	Emission angle: 0.18°
Compression type: MOC-PRED-X-5	Incidence angle: 35.43°
Gain mode: 0A (hexadecimal)	Phase angle: 35.46°
Offset mode: 40 (decimal)	North azimuth: 93.02°
	Sun azimuth: 344.05°
	Spacecraft altitude: 378.25 km
	Slant distance: 378.25 km



Figure A-25. M10-01789 - Sample terrain off NE rim of Herschel Basin

Ancillary data for MOC narrow-angle image M10-01789	
Acquisition parameters	Derived values
Image ID (picno): M10-01789	Longitude of image center: 228.81°W
Image start time: 1999-12-14T14:55:43.68 SCET	Latitude of image center: 12.81°S
Image width: 768 pixels	Scaled pixel width: 1.42 meters
Image height: 3712 pixels	Scaled image width: 1.09 km
Line integration time: 0.4821 millisecond	Scaled image height: 5.53 km
Pixel aspect ratio: 1.05	Solar longitude (Ls): 263.13°
Crosstrack summing: 1	Local True Solar Time: 13.96 decimal hours
Downtrack summing: 1	Emission angle: 0.23°
Compression type: MOC-PRED-X-5	Incidence angle: 30.33°
Gain mode: 0A (hexadecimal)	Phase angle: 30.53°
Offset mode: 42 (decimal)	North azimuth: 93.03°
	Sun azimuth: 335.01°
	Spacecraft altitude: 378.13 km
	Slant distance: 378.13 km

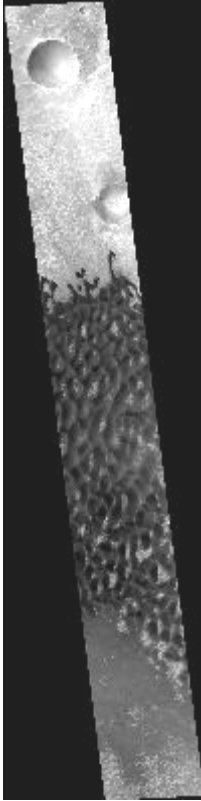


Figure A-26. M11-02107 - Dark dunes on floor of crater adjacent to Herschel Basin

Ancillary data for MOC narrow-angle image M11-02107	
Acquisition parameters	Derived values
Image ID (picno): M11-02107	Longitude of image center: 232.01°W
Image start time: 2000-01-15T11:36:55.01 SCET	Latitude of image center: 16.53°S
Image width: 1024 pixels	Scaled pixel width: 2.82 meters
Image height: 5248 pixels	Scaled image width: 2.89 km
Line integration time: 0.7231 millisecond	Scaled image height: 23.44 km
Pixel aspect ratio: 1.58	Solar longitude (Ls): 283.08°
Crosstrack summing: 2	Local True Solar Time: 13.62 decimal hours
Downtrack summing: 2	Emission angle: 0.21°
Compression type: MOC-PRED-X-5	Incidence angle: 24.14°
Gain mode: 4A (hexadecimal)	Phase angle: 24.18°
Offset mode: 38 (decimal)	North azimuth: 93.12°
	Sun azimuth: 339.84°
	Spacecraft altitude: 375.70 km
	Slant distance: 375.70 km

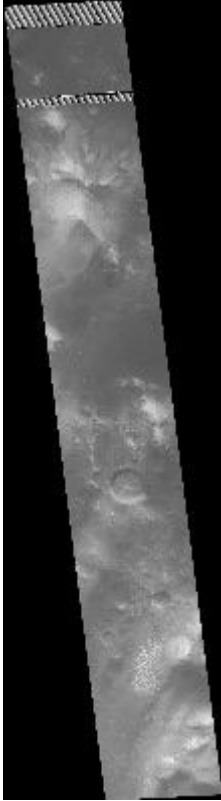


Figure A-27. M12-00672 - Rugged peak-ring mountains in E Herschel Basin

Ancillary data for MOC narrow-angle image M12-00672	
Acquisition parameters	Derived values
Image ID (picno): M12-00672	Longitude of image center: 229.04°W
Image start time: 2000-02-06T01:15:33.88 SCET	Latitude of image center: 14.50°S
Image width: 1024 pixels	Scaled pixel width: 2.84 meters
Image height: 4864 pixels	Scaled image width: 2.90 km
Line integration time: 0.7231 millisecc	Scaled image height: 21.73 km
Pixel aspect ratio: 1.57	Solar longitude (Ls): 296.26°
Crosstrack summing: 2	Local True Solar Time: 13.42 decimal hours
Downtrack summing: 2	Emission angle: 0.20°
Compression type: MOC-PRED-X-5	Incidence angle: 21.74°
Gain mode: 6A (hexadecimal)	Phase angle: 21.77°
Offset mode: 28 (decimal)	North azimuth: 93.07°
	Sun azimuth: 338.49°
	Spacecraft altitude: 377.39 km
	Slant distance: 377.39 km

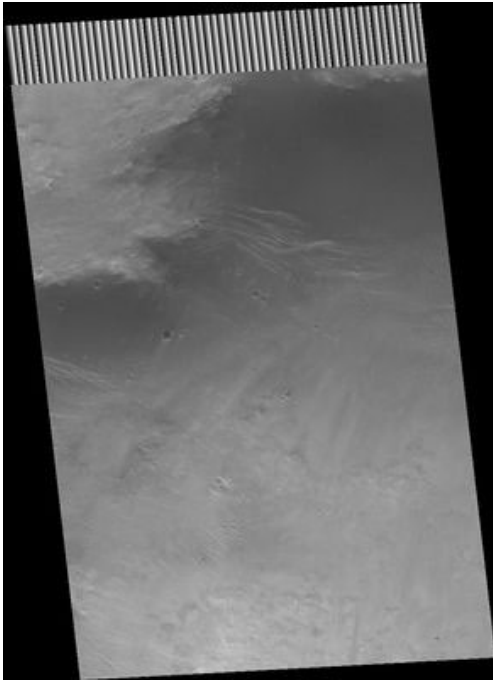


Figure A-28. M13-00630 - sample

Ancillary data for MOC narrow-angle image M13-00630

Acquisition parameters

Image ID (picno): M13-00630
Image start time: 2000-03-10T22:57:07.26 SCET
Image width: 768 pixels
Image height: 1536 pixels
Line integration time: 0.4821 millisecc
Pixel aspect ratio: 1.06
Crosstrack summing: 1
Downtrack summing: 1
Compression type: MOC-PRED-X-5
Gain mode: 0A (hexadecimal)
Offset mode: 38 (decimal)

Derived values

Longitude of image center: 227.91°W
Latitude of image center: 14.22°S
Scaled pixel width: 1.42 meters
Scaled image width: 1.09 km
Scaled image height: 2.30 km
Solar longitude (Ls): 316.22°
Local True Solar Time: 13.23 decimal hours
Emission angle: 0.39°
Incidence angle: 18.15°
Phase angle: 18.52°
North azimuth: 93.13°
Sun azimuth: 351.45°
Spacecraft altitude: 377.13 km
Slant distance: 377.14 km

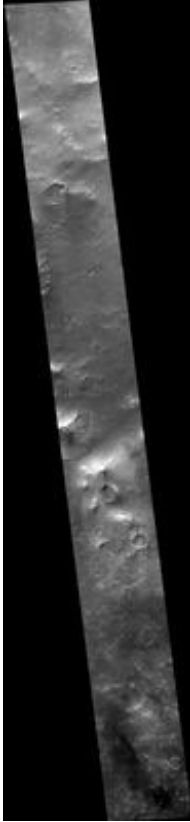


Figure A-29. M14-00754 - traverse across cratered upland inside Herschel Basin

Ancillary data for MOC narrow-angle image M14-00754

Acquisition parameters

Image ID (picno): M14-00754
Image start time: 2000-04-11T19:37:45.85 SCET
Image width: 512 pixels
Image height: 4736 pixels
Line integration time: 0.4821 millisecond
Pixel aspect ratio: 1.05
Crosstrack summing: 3
Downtrack summing: 3
Compression type: MOC-DCT-3
Gain mode: 4A (hexadecimal)
Offset mode: 40 (decimal)

Derived values

Longitude of image center: 231.15°W
Latitude of image center: 14.09°S
Scaled pixel width: 4.25 meters
Scaled image width: 2.17 km
Scaled image height: 21.15 km
Solar longitude (Ls): 334.00°
Local True Solar Time: 13.21 decimal hours
Emission angle: 0.20°
Incidence angle: 18.10°
Phase angle: 18.12°
North azimuth: 93.09°
Sun azimuth: 11.64°
Spacecraft altitude: 377.12 km
Slant distance: 377.12 km

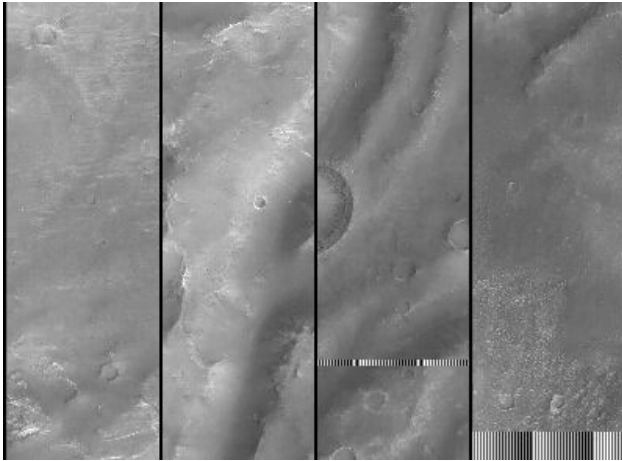


Figure A-30. M15-01486 - Short deep valley into crater immediately N of Herschel

Ancillary data for MOC narrow-angle image M15-01486

Acquisition parameters

Image ID (picno): M15-01486
 Image start time: 2000-05-22T21:52:50.92 SCET
 Image width: 672 pixels
 Image height: 8064 pixels
 Line integration time: 0.4821 millisecc
 Pixel aspect ratio: 1.05
 Crosstrack summing: 3
 Downtrack summing: 3
 Compression type: MOC-PRED-X-5
 Gain mode: 4A (hexadecimal)
 Offset mode: 40 (decimal)

Derived values

Longitude of image center: 229.20°W
 Latitude of image center: 12.17°S
 Scaled pixel width: 4.26 meters
 Scaled image width: 2.86 km
 Scaled image height: 36.09 km
 Solar longitude (Ls): 355.55°
 Local True Solar Time: 13.32 decimal hours
 Emission angle: 0.16°
 Incidence angle: 22.23°
 Phase angle: 22.17°
 North azimuth: 93.03°
 Sun azimuth: 29.02°
 Spacecraft altitude: 377.86 km
 Slant distance: 377.86 km

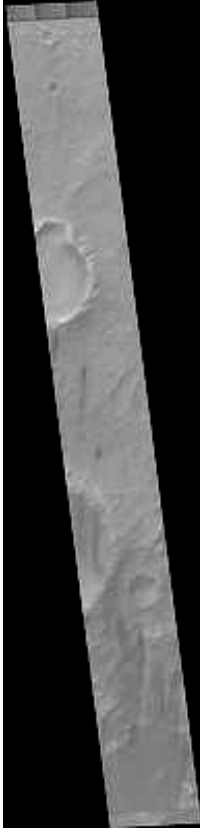


Figure A-31. M18-00644 - Full-resolution sample crater among dark material in Herschel Basin

Ancillary data for MOC narrow-angle image M18-00644	
Acquisition parameters	Derived values
Image ID (picno): M18-00644	Longitude of image center: 230.63°W
Image start time: 2000-08-11T01:27:13.03 SCET	Latitude of image center: 14.24°S
Image width: 768 pixels	Scaled pixel width: 1.42 meters
Image height: 7552 pixels	Scaled image width: 1.09 km
Line integration time: 0.4821 millisecond	Scaled image height: 11.25 km
Pixel aspect ratio: 1.05	Solar longitude (Ls): 33.86°
Crosstrack summing: 1	Local True Solar Time: 13.78 decimal hours
Downtrack summing: 1	Emission angle: 0.27°
Compression type: MOC-PRED-X-5	Incidence angle: 38.51°
Gain mode: 0A (hexadecimal)	Phase angle: 38.43°
Offset mode: 6 (decimal)	North azimuth: 93.16°
	Sun azimuth: 48.56°
	Spacecraft altitude: 377.59 km
	Slant distance: 377.60 km

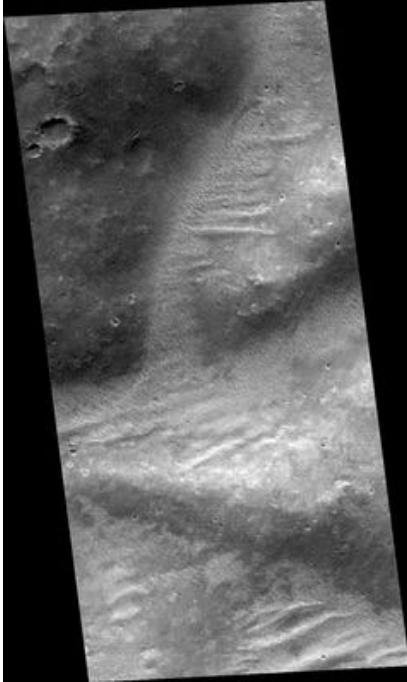


Figure A-32. M19-00489 - sample

Ancillary data for MOC narrow-angle image M19-00489	
Acquisition parameters	Derived values
Image ID (picno): M19-00489	Longitude of image center: 228.13°W
Image start time: 2000-09-08T19:44:59.02 SCET	Latitude of image center: 12.21°S
Image width: 768 pixels	Scaled pixel width: 1.42 meters
Image height: 1536 pixels	Scaled image width: 1.09 km
Line integration time: 0.4821 millisecc	Scaled image height: 2.29 km
Pixel aspect ratio: 1.05	Solar longitude (Ls): 46.78°
Crosstrack summing: 1	Local True Solar Time: 13.93 decimal hours
Downtrack summing: 1	Emission angle: 0.22°
Compression type: MOC-PRED-X-5	Incidence angle: 41.71°
Gain mode: 0A (hexadecimal)	Phase angle: 41.73°
Offset mode: 18 (decimal)	North azimuth: 93.02°
	Sun azimuth: 49.05°
	Spacecraft altitude: 378.66 km
	Slant distance: 378.66 km

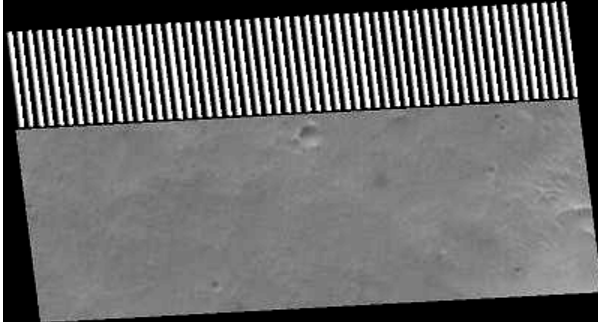


Figure A-33. M20-01590 – sample

Ancillary data for MOC narrow-angle image M20-01590	
Acquisition parameters	Derived values
Image ID (picno): M20-01590	Longitude of image center: 228.58°W
Image start time: 2000-10-27T02:48:18.54 SCET	Latitude of image center: 15.47°S
Image width: 768 pixels	Scaled pixel width: 1.42 meters
Image height: 1536 pixels	Scaled image width: 1.09 km
Line integration time: 0.4821 millisecond	Scaled image height: 2.29 km
Pixel aspect ratio: 1.05	Solar longitude (Ls): 68.00°
Crosstrack summing: 1	Local True Solar Time: 14.16 decimal hours
Downtrack summing: 1	Emission angle: 0.30°
Compression type: MOC-PRED-X-5	Incidence angle: 50.12°
Gain mode: 0A (hexadecimal)	Phase angle: 50.05°
Offset mode: 6 (decimal)	North azimuth: 93.15°
	Sun azimuth: 53.04°
	Spacecraft altitude: 377.93 km
	Slant distance: 377.93 km

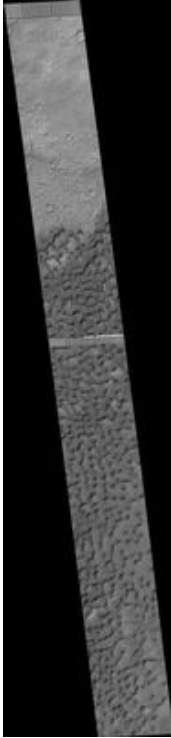


Figure A-34. M21-00018 - Dark dunes in SW Herschel Basin

Ancillary data for MOC narrow-angle image M21-00018	
Acquisition parameters	Derived values
Image ID (picno): M21-00018	Longitude of image center: 232.48°W
Image start time: 2000-11-01T06:22:13.47 SCET	Latitude of image center: 15.07°S
Image width: 672 pixels	Scaled pixel width: 4.26 meters
Image height: 6784 pixels	Scaled image width: 2.86 km
Line integration time: 0.4821 millisecond	Scaled image height: 30.32 km
Pixel aspect ratio: 1.05	Solar longitude (Ls): 70.25°
Crosstrack summing: 3	Local True Solar Time: 14.18 decimal hours
Downtrack summing: 3	Emission angle: 0.09°
Compression type: MOC-PRED-X-5	Incidence angle: 50.28°
Gain mode: 0A (hexadecimal)	Phase angle: 50.18°
Offset mode: 36 (decimal)	North azimuth: 92.95°
	Sun azimuth: 52.69°
	Spacecraft altitude: 378.00 km
	Slant distance: 378.00 km

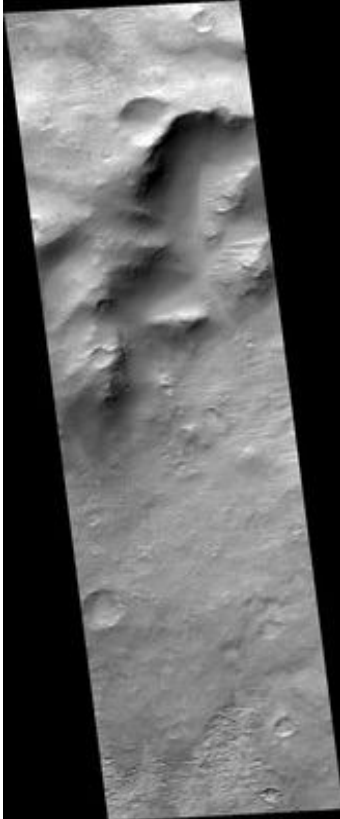


Figure A-35. M22-02419 – sample

Ancillary data for MOC narrow-angle image M22-02419

Acquisition parameters

Image ID (picno): M22-02419
Image start time: 2000-12-30T20:19:49.76 SCET
Image width: 672 pixels
Image height: 1792 pixels
Line integration time: 0.6026 millisecond
Pixel aspect ratio: 1.30
Crosstrack summing: 3
Downtrack summing: 3
Compression type: MOC-PRED-X-5
Gain mode: 4A (hexadecimal)
Offset mode: 34 (decimal)

Derived values

Longitude of image center: 228.09°W
Latitude of image center: 12.39°S
Scaled pixel width: 4.28 meters
Scaled image width: 2.87 km
Scaled image height: 10.00 km
Solar longitude (Ls): 96.42°
Local True Solar Time: 14.34 decimal hours
Emission angle: 0.22°
Incidence angle: 50.79°
Phase angle: 50.64°
North azimuth: 93.07°
Sun azimuth: 50.66°
Spacecraft altitude: 379.52 km
Slant distance: 379.52 km

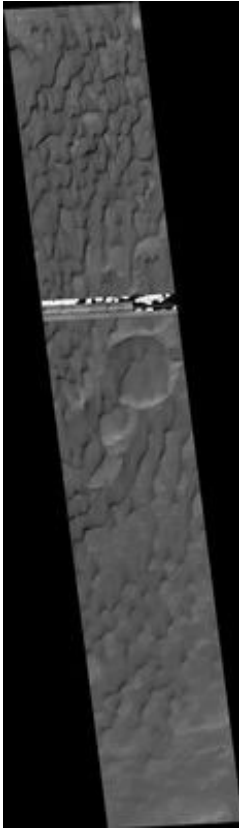


Figure A-36. M23-00263 - Dunes in W Herschel Basin

Ancillary data for MOC narrow-angle image M23-00263

Acquisition parameters

Image ID (picno): M23-00263
 Image start time: 2001-01-04T23:54:23.88 SCET
 Image width: 1024 pixels
 Image height: 3968 pixels
 Line integration time: 0.7231 millisecc
 Pixel aspect ratio: 1.57
 Crosstrack summing: 2
 Downtrack summing: 2
 Compression type: MOC-PRED-X-5
 Gain mode: 2A (hexadecimal)
 Offset mode: 26 (decimal)

Derived values

Longitude of image center: 232.02°W
 Latitude of image center: 14.47°S
 Scaled pixel width: 2.85 meters
 Scaled image width: 2.91 km
 Scaled image height: 17.76 km
 Solar longitude (Ls): 98.72°
 Local True Solar Time: 14.36 decimal hours
 Emission angle: 0.23°
 Incidence angle: 52.42°
 Phase angle: 52.26°
 North azimuth: 93.11°
 Sun azimuth: 51.44°
 Spacecraft altitude: 378.67 km
 Slant distance: 378.67 km

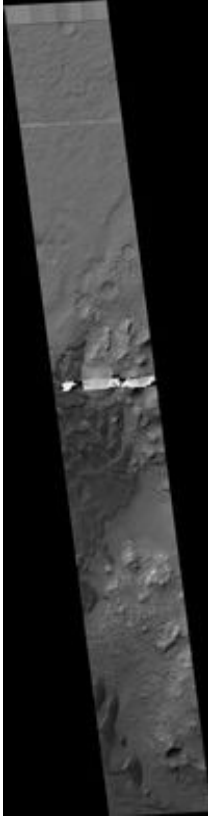


Figure A-37. M23-00825 - Intracrater dune field at 16.5 S 231.8 W

Ancillary data for MOC narrow-angle image M23-00825	
Acquisition parameters	Derived values
Image ID (picno): M23-00825	Longitude of image center: 231.96°W
Image start time: 2001-01-12T04:31:42.98 SCET	Latitude of image center: 16.51°S
Image width: 1024 pixels	Scaled pixel width: 2.84 meters
Image height: 5248 pixels	Scaled image width: 2.91 km
Line integration time: 0.7231 millisecc	Scaled image height: 23.44 km
Pixel aspect ratio: 1.57	Solar longitude (Ls): 101.94°
Crosstrack summing: 2	Local True Solar Time: 14.38 decimal hours
Downtrack summing: 2	Emission angle: 0.23°
Compression type: MOC-PRED-X-5	Incidence angle: 53.98°
Gain mode: 2A (hexadecimal)	Phase angle: 53.82°
Offset mode: 30 (decimal)	North azimuth: 93.16°
	Sun azimuth: 51.97°
	Spacecraft altitude: 377.97 km
	Slant distance: 377.98 km

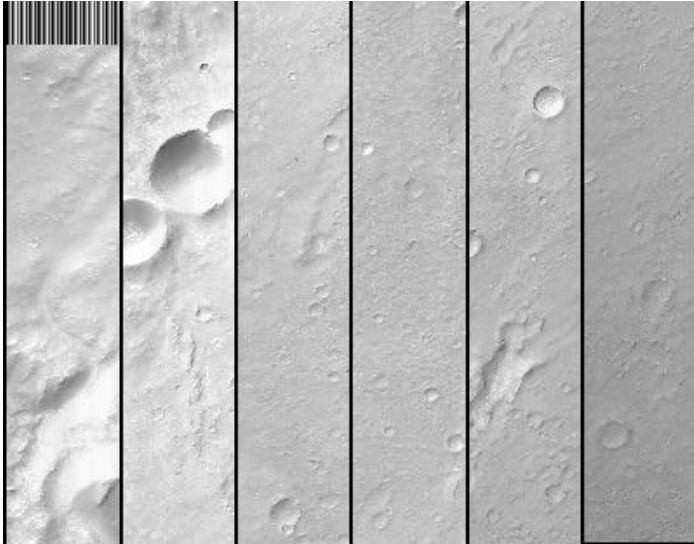


Figure A-38. E01-01967 - Herschel Basin survey traverse across west side

Ancillary data for MOC narrow-angle image E01-01967	
Acquisition parameters	Derived values
Image ID (picno): E01-01967	Longitude of image center: 231.84°W
Image start time: 2001-02-26T09:32:08.86 SCET	Latitude of image center: 14.51°S
Image width: 336 pixels	Scaled pixel width: 8.56 meters
Image height: 24832 pixels	Scaled image width: 2.87 km
Line integration time: 0.4821 millisecc	Scaled image height: 221.44 km
Pixel aspect ratio: 1.02	Solar longitude (Ls): 122.71°
Crosstrack summing: 6	Local True Solar Time: 14.47 decimal hours
Downtrack summing: 6	Emission angle: 0.14°
Compression type: MOC-PRED-X-5	Incidence angle: 50.96°
Gain mode: 6A (hexadecimal)	Phase angle: 50.96°
Offset mode: 22 (decimal)	North azimuth: 93.10°
	Sun azimuth: 46.43°
	Spacecraft altitude: 379.84 km
	Slant distance: 379.84 km

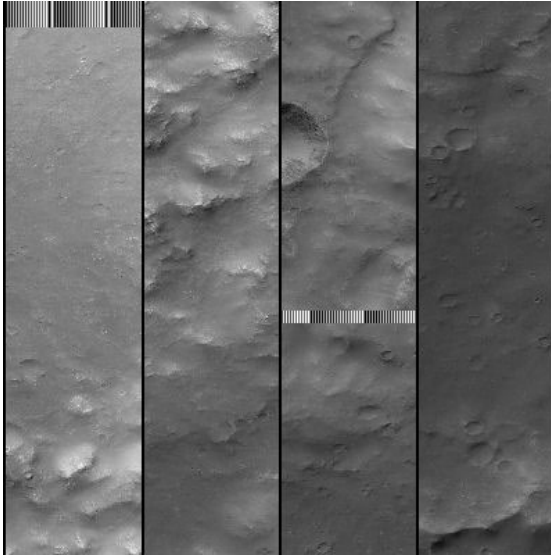


Figure A-39. E01-02211 - Survey traverse across rugged SE Herschel rim and dark material

Ancillary data for MOC narrow-angle image E01-02211

Acquisition parameters

Image ID (picno): E01-02211
 Image start time: 2001-02-28T10:35:49.87 SCET
 Image width: 672 pixels
 Image height: 11136 pixels
 Line integration time: 0.6026 millisecc
 Pixel aspect ratio: 1.32
 Crosstrack summing: 3
 Downtrack summing: 3
 Compression type: MOC-PRED-X-5
 Gain mode: 4A (hexadecimal)
 Offset mode: 28 (decimal)

Derived values

Longitude of image center: 227.92°W
 Latitude of image center: 15.46°S
 Scaled pixel width: 4.28 meters
 Scaled image width: 2.87 km
 Scaled image height: 62.89 km
 Solar longitude (Ls): 123.67°
 Local True Solar Time: 14.48 decimal hours
 Emission angle: 0.17°
 Incidence angle: 51.54°
 Phase angle: 51.53°
 North azimuth: 93.20°
 Sun azimuth: 46.76°
 Spacecraft altitude: 379.85 km
 Slant distance: 379.85 km

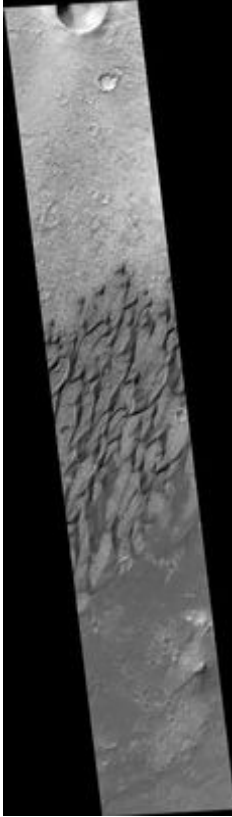


Figure A-40. E02-00602 - Dunes in Herschel Basin

Ancillary data for MOC narrow-angle image E02-00602	
Acquisition parameters	Derived values
Image ID (picno): E02-00602	Longitude of image center: 229.00°W
Image start time: 2001-03-07T15:17:32.93 SCET	Latitude of image center: 15.74°S
Image width: 1024 pixels	Scaled pixel width: 2.86 meters
Image height: 3968 pixels	Scaled image width: 2.92 km
Line integration time: 0.7231 millisecond	Scaled image height: 17.54 km
Pixel aspect ratio: 1.55	Solar longitude (Ls): 127.09°
Crosstrack summing: 2	Local True Solar Time: 14.50 decimal hours
Downtrack summing: 2	Emission angle: 0.27°
Compression type: MOC-PRED-X-5	Incidence angle: 51.33°
Gain mode: 0A (hexadecimal)	Phase angle: 51.24°
Offset mode: 40 (decimal)	North azimuth: 93.16°
	Sun azimuth: 45.80°
	Spacecraft altitude: 380.39 km
	Slant distance: 380.40 km

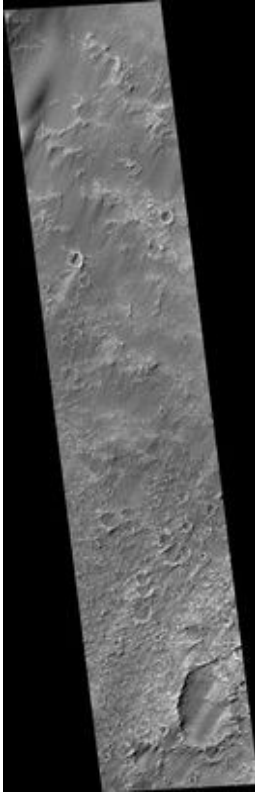


Figure A-41. E02-02816 - Dark material in central Herschel Basin

Ancillary data for MOC narrow-angle image E02-02816	
Acquisition parameters	Derived values
Image ID (picno): E02-02816	Longitude of image center: 229.60°W
Image start time: 2001-03-31T06:30:20.58 SCET	Latitude of image center: 14.51°S
Image width: 1024 pixels	Scaled pixel width: 1.43 meters
Image height: 3200 pixels	Scaled image width: 1.46 km
Line integration time: 0.7231 millisecc	Scaled image height: 7.14 km
Pixel aspect ratio: 1.56	Solar longitude (Ls): 138.56°
Crosstrack summing: 1	Local True Solar Time: 14.56 decimal hours
Downtrack summing: 1	Emission angle: 0.22°
Compression type: MOC-PRED-X-5	Incidence angle: 48.95°
Gain mode: 0A (hexadecimal)	Phase angle: 48.91°
Offset mode: 16 (decimal)	North azimuth: 93.16°
	Sun azimuth: 40.84°
	Spacecraft altitude: 380.37 km
	Slant distance: 380.37 km

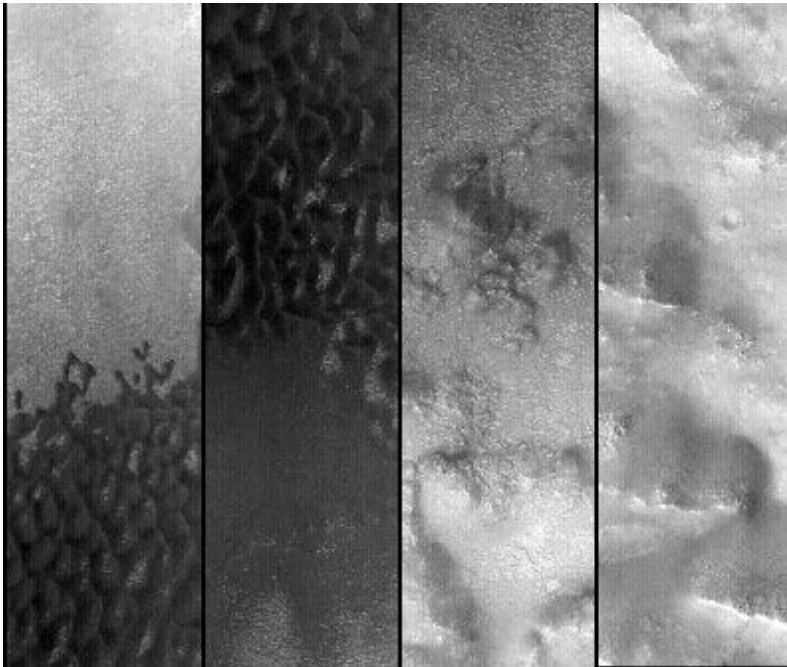


Figure A-42. E09-02803 - Crater survey at 16.7 S231.8W

Ancillary data for MOC narrow-angle image E09-02803

Acquisition parameters

Image ID (picno): E09-02803
 Image start time: 2001-11-01T00:35:30.24 SCET
 Image width: 672 pixels
 Image height: 9216 pixels
 Line integration time: 0.4821 millisecond
 Pixel aspect ratio: 0.99
 Crosstrack summing: 3
 Downtrack summing: 3
 Compression type: MOC-PRED-X-5
 Gain mode: 4A (hexadecimal)
 Offset mode: 46 (decimal)

Derived values

Longitude of image center: 232.00°W
 Latitude of image center: 16.72°S
 Scaled pixel width: 4.48 meters
 Scaled image width: 3.00 km
 Scaled image height: 41.05 km
 Solar longitude (Ls): 263.40°
 Local True Solar Time: 14.00 decimal hours
 Emission angle: 18.19°
 Incidence angle: 29.19°
 Phase angle: 38.66°
 North azimuth: 93.12°
 Sun azimuth: 341.56°
 Spacecraft altitude: 379.37 km
 Slant distance: 397.17 km

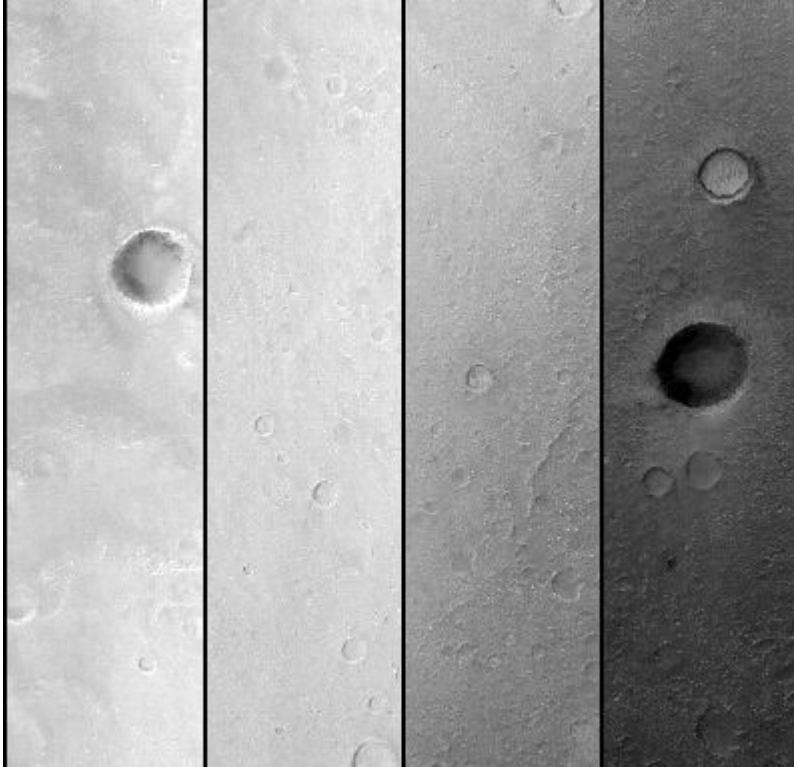


Figure A-43. E09-02804 - Northwestern Herschel Crater floor survey

Ancillary data for MOC narrow-angle image E09-02804

Acquisition parameters

Image ID (picno): E09-02804
 Image start time: 2001-11-01T00:36:28.64 SCET
 Image width: 512 pixels
 Image height: 8064 pixels
 Line integration time: 0.4821 millisecc
 Pixel aspect ratio: 0.93
 Crosstrack summing: 4
 Downtrack summing: 4
 Compression type: MOC-PRED-X-5
 Gain mode: 8A (hexadecimal)
 Offset mode: 46 (decimal)

Derived values

Longitude of image center: 232.41°W
 Latitude of image center: 13.66°S
 Scaled pixel width: 5.99 meters
 Scaled image width: 3.06 km
 Scaled image height: 46.51 km
 Solar longitude (Ls): 263.40°
 Local True Solar Time: 13.98 decimal hours
 Emission angle: 18.21°
 Incidence angle: 30.29°
 Phase angle: 40.79°
 North azimuth: 93.09°
 Sun azimuth: 336.56°
 Spacecraft altitude: 380.53 km
 Slant distance: 398.42 km



Figure A-44. E10-00272 - Dunes in eastern Herschel Basin

Ancillary data for MOC narrow-angle image E10-00272	
Acquisition parameters	Derived values
Image ID (picno): E10-00272	Longitude of image center: 228.39°W
Image start time: 2001-11-03T01:39:31.23 SCET	Latitude of image center: 15.26°S
Image width: 1024 pixels	Scaled pixel width: 2.99 meters
Image height: 5376 pixels	Scaled image width: 3.06 km
Line integration time: 0.7231 millisecc	Scaled image height: 23.94 km
Pixel aspect ratio: 1.49	Solar longitude (Ls): 264.69°
Crosstrack summing: 2	Local True Solar Time: 13.97 decimal hours
Downtrack summing: 2	Emission angle: 17.99°
Compression type: MOC-PRED-X-5	Incidence angle: 29.39°
Gain mode: 4A (hexadecimal)	Phase angle: 39.32°
Offset mode: 38 (decimal)	North azimuth: 93.07°
	Sun azimuth: 338.80°
	Spacecraft altitude: 379.94 km
	Slant distance: 397.35 km

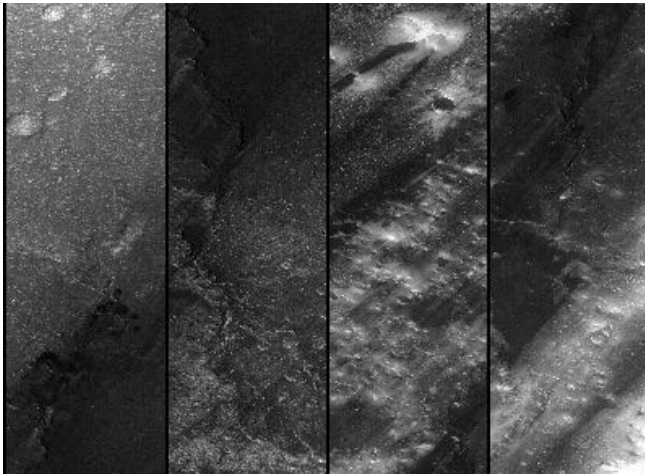


Figure A-45. E10-01396 - Dark material in eastern Herschel Basin

Ancillary data for MOC narrow-angle image E10-01396

Acquisition parameters

Image ID (picno): E10-01396
 Image start time: 2001-11-10T06:20:51.93 SCET
 Image width: 1024 pixels
 Image height: 12160 pixels
 Line integration time: 0.7231 millisecc
 Pixel aspect ratio: 1.49
 Crosstrack summing: 2
 Downtrack summing: 2
 Compression type: MOC-PRED-X-5
 Gain mode: 4A (hexadecimal)
 Offset mode: 36 (decimal)

Derived values

Longitude of image center: 229.47°W
 Latitude of image center: 14.26°S
 Scaled pixel width: 2.98 meters
 Scaled image width: 3.05 km
 Scaled image height: 54.19 km
 Solar longitude (Ls): 269.23°
 Local True Solar Time: 13.88 decimal hours
 Emission angle: 17.98°
 Incidence angle: 28.74°
 Phase angle: 39.27°
 North azimuth: 93.07°
 Sun azimuth: 336.34°
 Spacecraft altitude: 379.75 km

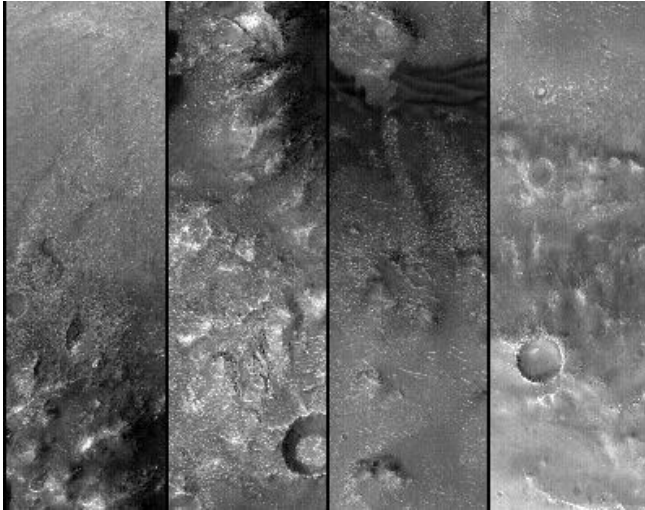


Figure A-46. E11-00157 - Dunes in crater on southwest rim of Herschel Basin

Ancillary data for MOC narrow-angle image E11-00157	
Acquisition parameters	Derived values
Image ID (picno): E11-00157	Longitude of image center: 231.91°W
Image start time: 2001-12-01T20:23:04.09 SCET	Latitude of image center: 16.68°S
Image width: 672 pixels	Scaled pixel width: 4.45 meters
Image height: 8704 pixels	Scaled image width: 2.99 km
Line integration time: 0.4821 millisc	Scaled image height: 38.80 km
Pixel aspect ratio: 1.00	Solar longitude (Ls): 282.71°
Crosstrack summing: 3	Local True Solar Time: 13.66 decimal hours
Downtrack summing: 3	Emission angle: 17.91°
Compression type: MOC-PRED-X-5	Incidence angle: 24.63°
Gain mode: 4A (hexadecimal)	Phase angle: 34.74°
Offset mode: 42 (decimal)	North azimuth: 93.11°
	Sun azimuth: 340.37°
	Spacecraft altitude: 378.13 km
	Slant distance: 395.31 km

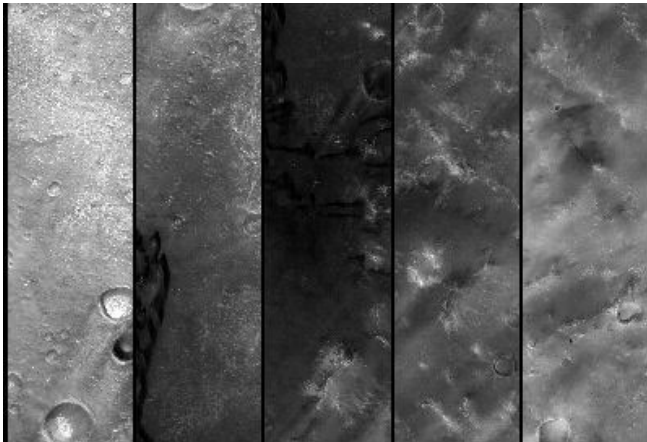


Figure A-47. E11-00527 - Southeastern floor of Herschel Crater

Ancillary data for MOC narrow-angle image E11-00527

Acquisition parameters

Image ID (picno): E11-00527
 Image start time: 2001-12-03T21:26:50.73 SCET
 Image width: 512 pixels
 Image height: 8960 pixels
 Line integration time: 0.4821 millisec
 Pixel aspect ratio: 1.00
 Crosstrack summing: 4
 Downtrack summing: 4
 Compression type: MOC-PRED-X-5
 Gain mode: 6A (hexadecimal)
 Offset mode: 38 (decimal)

Derived values

Longitude of image center: 228.24°W
 Latitude of image center: 15.47°S
 Scaled pixel width: 5.95 meters
 Scaled image width: 3.04 km
 Scaled image height: 53.27 km
 Solar longitude (Ls): 283.97°
 Local True Solar Time: 13.63 decimal hours
 Emission angle: 17.94°
 Incidence angle: 24.75°
 Phase angle: 35.37°
 North azimuth: 93.08°
 Sun azimuth: 338.04°
 Spacecraft altitude: 378.85 km
 Slant distance: 396.12 km

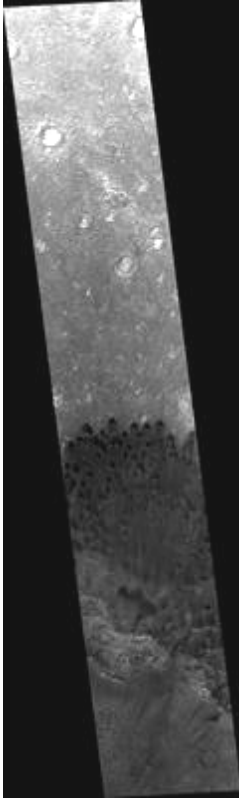


Figure A-48. E11-01859 - Dark material in Herschel Basin

Ancillary data for MOC narrow-angle image E11-01859	
Acquisition parameters	Derived values
Image ID (picno): E11-01859	Longitude of image center: 229.36°W
Image start time: 2001-12-11T02:08:21.33 SCET	Latitude of image center: 13.68°S
Image width: 1024 pixels	Scaled pixel width: 2.99 meters
Image height: 3968 pixels	Scaled image width: 3.06 km
Line integration time: 0.7231 millisecc	Scaled image height: 17.68 km
Pixel aspect ratio: 1.49	Solar longitude (Ls): 288.40°
Crosstrack summing: 2	Local True Solar Time: 13.56 decimal hours
Downtrack summing: 2	Emission angle: 17.93°
Compression type: MOC-PRED-X-5	Incidence angle: 24.41°
Gain mode: 6A (hexadecimal)	Phase angle: 35.66°
Offset mode: 28 (decimal)	North azimuth: 93.06°
	Sun azimuth: 335.06°
	Spacecraft altitude: 379.97 km

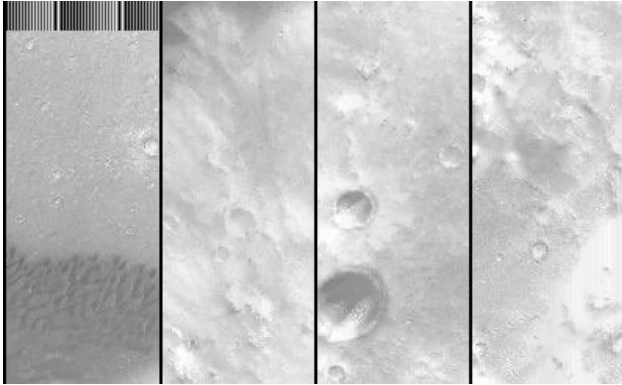


Figure A-49. E16-01318 - Light material and knobs on Herschel Crater floor

Ancillary data for MOC narrow-angle image E16-01318

Acquisition parameters

Image ID (picno): E16-01318
 Image start time: 2002-05-19T08:26:00.21 SCET
 Image width: 672 pixels
 Image height: 7424 pixels
 Line integration time: 0.4821 millisecc
 Pixel aspect ratio: 0.99
 Crosstrack summing: 3
 Downtrack summing: 3
 Compression type: MOC-PRED-X-5
 Gain mode: 2A (hexadecimal)
 Offset mode: 38 (decimal)

Derived values

Longitude of image center: 229.23°W
 Latitude of image center: 13.95°S
 Scaled pixel width: 4.48 meters
 Scaled image width: 3.01 km
 Scaled image height: 33.05 km
 Solar longitude (Ls): 14.93°
 Local True Solar Time: 13.60 decimal hours
 Emission angle: 17.89°
 Incidence angle: 31.36°
 Phase angle: 23.24°
 North azimuth: 93.08°
 Sun azimuth: 41.76°
 Spacecraft altitude: 380.56 km
 Slant distance: 397.80 km

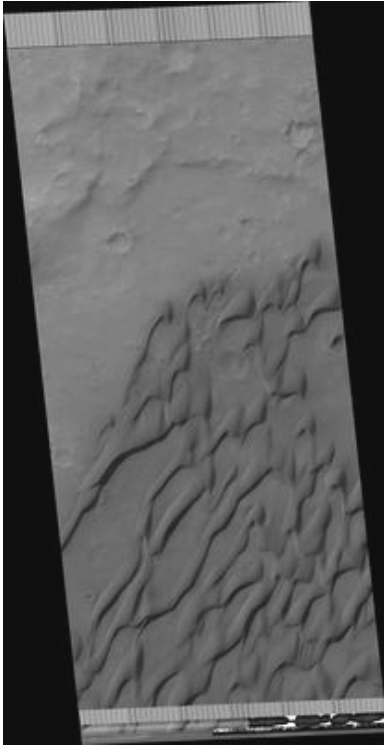


Figure A-50. R01-01236 - Stereo with M00-03222 Herschel Basin groove-surfaced dunes

Ancillary data for MOC narrow-angle image R01-01236	
Acquisition parameters	Derived values
Image ID (picno): R01-01236	Longitude of image center: 228.45°W
Image start time: 2003-01-25T01:13:41.98 SCET	Latitude of image center: 15.34°S
Image width: 1536 pixels	Scaled pixel width: 1.81 meters
Image height: 5376 pixels	Scaled image width: 2.79 km
Line integration time: 0.7231 millisecond	Scaled image height: 13.34 km
Pixel aspect ratio: 1.37	Solar longitude (Ls): 127.78°
Crosstrack summing: 1	Local True Solar Time: 14.42 decimal hours
Downtrack summing: 1	Emission angle: 28.62°
Compression type: MOC-PRED-X-5	Incidence angle: 50.09°
Gain mode: 0A (hexadecimal)	Phase angle: 72.23°
Offset mode: 22 (decimal)	North azimuth: 92.36°
	Sun azimuth: 45.54°
	Spacecraft altitude: 377.51 km
	Slant distance: 423.83 km



Figure A-51. R03-00358 - Attempt repeat of image M02-00612 dunes in Herschel basin

Ancillary data for MOC narrow-angle image R03-00358	
Acquisition parameters	Derived values
Image ID (picno): R03-00358	Longitude of image center: 230.16°W
Image start time: 2003-03-07T03:57:59.00 SCET	Latitude of image center: 14.23°S
Image width: 1280 pixels	Scaled pixel width: 1.49 meters
Image height: 4224 pixels	Scaled image width: 1.91 km
Line integration time: 0.7231 millisecond	Scaled image height: 9.40 km
Pixel aspect ratio: 1.49	Solar longitude (Ls): 148.04°
Crosstrack summing: 1	Local True Solar Time: 14.75 decimal hours
Downtrack summing: 1	Emission angle: 17.91°
Compression type: MOC-PRED-X-5	Incidence angle: 49.20°
Gain mode: 2A (hexadecimal)	Phase angle: 40.98°
Offset mode: 6 (decimal)	North azimuth: 93.09°
	Sun azimuth: 34.83°
	Spacecraft altitude: 379.71 km
	Slant distance: 396.94 km

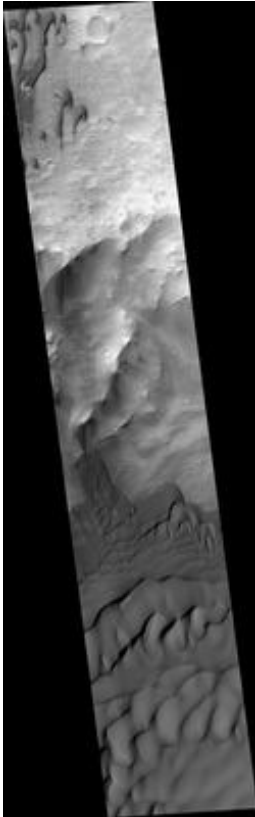


Figure A-52. R04-00598 - Dune field in FHA-01381 in crater at 14.4 S 231.5 W

Ancillary data for MOC narrow-angle image R04-00598	
Acquisition parameters	Derived values
Image ID (picno): R04-00598	Longitude of image center: 231.75°W
Image start time: 2003-04-10T02:02:15.23 SCET	Latitude of image center: 14.38°S
Image width: 1024 pixels	Scaled pixel width: 3.36 meters
Image height: 5632 pixels	Scaled image width: 3.44 km
Line integration time: 0.4821 millisecc	Scaled image height: 18.66 km
Pixel aspect ratio: 0.99	Solar longitude (Ls): 165.81°
Crosstrack summing: 2	Local True Solar Time: 15.01 decimal hours
Downtrack summing: 2	Emission angle: 23.84°
Compression type: MOC-PRED-X-5	Incidence angle: 49.38°
Gain mode: 2A (hexadecimal)	Phase angle: 29.10°
Offset mode: 18 (decimal)	North azimuth: 93.63°
	Sun azimuth: 24.86°
	Spacecraft altitude: 377.45 km
	Slant distance: 408.69 km

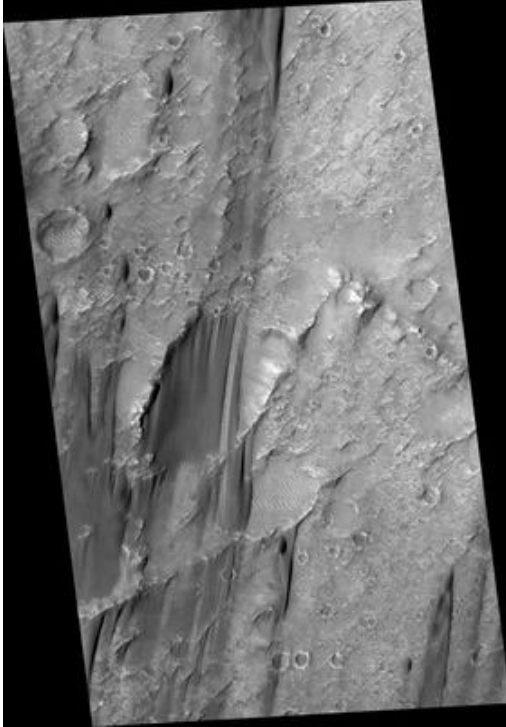


Figure A-53. R05-00941 - Grooved dunes in Herschel Basin

Ancillary data for MOC narrow-angle image R05-00941	
Acquisition parameters	Derived values
Image ID (picno): R05-00941	Longitude of image center: 230.60°W
Image start time: 2003-05-10T21:34:55.80 SCET	Latitude of image center: 14.28°S
Image width: 2048 pixels	Scaled pixel width: 1.49 meters
Image height: 3456 pixels	Scaled image width: 3.05 km
Line integration time: 0.4821 millisecc	Scaled image height: 5.13 km
Pixel aspect ratio: 1.00	Solar longitude (Ls): 182.88°
Crosstrack summing: 1	Local True Solar Time: 14.89 decimal hours
Downtrack summing: 1	Emission angle: 17.76°
Compression type: MOC-PRED-X-5	Incidence angle: 44.93°
Gain mode: 2A (hexadecimal)	Phase angle: 43.36°
Offset mode: 0 (decimal)	North azimuth: 93.23°
	Sun azimuth: 16.18°
	Spacecraft altitude: 379.65 km
	Slant distance: 396.59 km

APPENDIX B

DIRECTIONAL DATA FROM IMAGES.

MSSS#	Dunes	Deg. Photoshop	Deg Azimuth	Streaks or shadows	Deg. Photoshop	Deg Azimuth	Overall I	Notes
SP36506								No Eolian Features seen

MSSS#	Dunes	Deg. Photoshop	Deg Azimuth	Streaks	Deg. Photoshop	Deg Azimuth	Overall I	Notes
SP36507	1	-81.0	171.0					Barchan, Barchanoid and possibly Seif dunes. Possibly multiple wind directions but Image Quality too low to tell for certain. It appears "blurry" especially in the southern half of the FOV
	2	-77.5	167.5					
	3	-79.0	169.0					
	4	-79.4	169.4					
	5	-80.1	170.1					
	6	-82.6	172.6					
	7	-81.0	171.0					
	8	-78.0	168.0					
	9	-88.7	178.7					
	10	-81.8	171.8					
	11	-80.9	170.9					
	12	-76.1	166.1					
	13	-74.1	164.1					
	14	-74.4	164.4					
	15	-74.3	164.3					
<i>Mean:</i>		-79.3	169.3				169.3	
<i>Std Dev:</i>			3.8				3.8	

MSSS#	Dunes	Deg. Photoshop	Deg Azimuth	Streaks	Deg. Photoshop	Deg Azimuth	Overall I	Notes
FHA00473				1	-14.3	104.3		Some dark streaks coming off of ridges. Hard to really see. Image has a lot of noise
				2	-13.6	103.6		
				3	-12.1	102.1		
				4	-11.0	101.0		
				5	-11.8	101.8		
				6	-15.4	105.4		
				7	-17.9	107.9		
<i>Mean</i>					-13.7	103.7	103.7	
<i>Std Dev:</i>						2.4	2.4	

MSSS#	Dunes	Deg. Photoshop	Deg Azimuth	Streaks	Deg. Photoshop	Deg Azimuth	Overall I	Notes
FHA00583								No Eolian Features seen

MSSS#	Dunes	Deg. Photoshop	Deg Azimuth	Streaks	Deg. Photoshop	Deg Azimuth	Overall I	Notes
FHA00914								No Eolian Features seen

MSSS#	Dunes	Deg. Photoshop	Deg Azimuth	Streaks	Deg. Photoshop	Deg Azimuth	Overall I	Notes
FHA03181	1	-56.6	146.6	1	-82.8	172.8		There appears to be a "N-S" texture in this image. At least some of this has to do with image quality. In the northern part of the image there are certainly some "N-S" wind streaks. It appears in the south of the
	2	-57.7	147.7	2	-85.8	175.8		
	3	-60.4	150.4	3	-86.3	176.3		
	4	-60.3	150.3	4	-84.9	174.9		
	5	-85.6	175.6	5	-68.1	158.1		
	6	-82.6	172.6	6	-75.9	165.9		
	7	-62.1	152.1					
	8	-53.5	143.5					
<i>Mean</i>		-64.9	154.9		-80.6	170.6	161.6	

								image the wind is veering off to the right (east), but I can't get any reliable forms to infer from so I won't split the image.
<i>Std Dev:</i>			12.2			7.2	12.9	

MSSS#	Dunes	Deg. Photoshop	Deg Azimuth	Streaks	Deg. Photoshop	Deg Azimuth	Overall I	Notes
M0000790				1	-107.1	197.1		After an extreme contrast enhancement I did see wind shadows and streaks good enough to get a direction from. Bright ripples abound, many in crater floors. As usual they don't line up and are over ridden by darker streaks. Sand shadows inside craters. Follows Greeley's model for "back vortex" piling sand up on the lee inter-crater wall. Image was split once because the northern half has consistently different wind directions than the south.
				2	-112.5	202.5		
				3	-108.1	198.1		
				4	-109.0	199.0		
				5	-104.6	194.6		
				6	-101.5	191.5		
				7	-101.0	191.0		
<i>Mean</i>					-106.3	196.3	196.3	
<i>Std Dev:</i>						4.2	4.2	
				8	-95.7	185.7		
				9	-95.7	185.7		
				10	-97.3	187.3		
				11	-92.2	182.2		
				12	-92.0	182.0		
<i>Mean</i>					-94.6	184.6	184.6	
<i>Std Dev:</i>						2.4	2.4	

MSSS#	Dunes	Deg. Photoshop	Deg Azimuth	Streaks	Deg. Photoshop	Deg Azimuth	Overall I	Notes
M003222	1	-114.2	204.2	1	-110.6	200.6		The streaks in this case are more like dune grooves. Generally they follow the wind direction. The dunes in this image appear to be between barchanoidal
	2	-84.6	174.6	2	-103.6	193.6		
	3	-102.5	192.5	3	-94.7	184.7		
	4	-97.2	187.2	4	-123.7	213.7		
	5	-118.5	208.5	5	-110.9	200.9		
	6	-103.6	193.6	6	-105.7	195.7		
	7	-103.9	193.9	7	-109.6	199.6		
				8	-112.4	202.4		
				9	-109.7	199.7		
				10	-112.3	202.3		
				11	-114.9	204.9		

								and seif. Making determination s very difficult.
<i>Mean</i>		-103.5	193.5		-109.8	199.8	197.4	
<i>Std Dev:</i>			11.1			7.2	9.2	

MSSS#	Dunes	Deg. Photoshop	Deg Azimuth	Streaks	Deg. Photoshop	Deg Azimuth	Overall I	Notes
M0103831								Bad image. Largest image file 270K - not high enough res to see anything.

MSSS#	Dunes	Deg. Photoshop	Deg Azimuth	Streaks	Deg. Photoshop	Deg Azimuth	Overall I	Notes
M0200612	1	-98.7	188.7					South part of image has features - barchan. Image split once.
	2	-97.2	187.2					
	3	-94.5	184.5					
	4	-95.4	185.4					
	5	-95.2	185.2					
	6	-93.6	183.6					
	7	-93.9	183.9					
<i>Mean</i>		-95.5	185.5				185.5	
<i>Std Dev:</i>			1.8				1.8	

MSSS#	Dunes	Deg. Photoshop	Deg Azimuth	Streaks	Deg. Photoshop	Deg Azimuth	Overall I	Notes
M0201996								Asymmetric barchanoidal dunes. Grooves present. Mainly in north of image. Image split to reflect this on the final map. There are enough other forms present to avoid using the grooves for a determination. Grooves coincident with the other forms.
	1	-128.7	218.7	1	-122.1	212.1		
	2	-118.8	208.8	2	-114.2	204.2		
	3	-114.5	204.5	3	-119.7	209.7		
	4	-115.5	205.5	4	-120.7	210.7		
	5	-120.5	210.5					
	6	-113.0	203.0					
<i>Mean</i>		-118.5	208.5		-119.2	209.2	208.8	
<i>Std Dev:</i>			5.7			3.5	4.7	

MSSS#	Dunes	Deg. Photoshop	Deg Azimuth	Streaks	Deg. Photoshop	Deg Azimuth	Overall I	Notes
M0201998				1	-36.3	126.3		Lots of small crater in image. Under extreme contrast able to see crater wind streaks. Generally all to the SSE. There is one small crater with a streak to the SSW,
				2	-36.5	126.5		
				3	-38.7	128.7		
				4	-39.8	129.8		
				5	-38.0	128.0		
				6	-30.2	120.2		
				7	-47.0	137.0		
				8	-42.2	132.2		
				9	-41.5	131.5		
				10	-40.4	130.4		
				11	-40.3	130.3		
				12	-45.0	135.0		

								but it may be ejecta as the crater has a halo. There are bright linear land forms that maybe eolian or may not. They were not measured.
<i>Mean</i>					-39.7	129.7	129.7	
<i>Std Dev:</i>						4.3	4.3	

MSSS#	Dunes	Deg. Photoshop	Deg Azimuth	Streaks	Deg. Photoshop	Deg Azimuth	Overall I	Notes
M0202819	1	-56.3	146.3					A number of immature barchans. Very interesting image as there appear to be parabolic dunes in it (?). There are also very acute barchan apexes. Formative winds are variable. Topographic effects from the dunes themselves. I am taking extra measurement s to get a good average.
	2	-46.6	136.6					
	3	-75.4	165.4					
	4	-39.9	129.9					
	5	-50.5	140.5					
	6	-60.1	150.1					
	7	-64.1	154.1					
	8	-57.1	147.1					
	9	-48.1	138.1					
	10	-63.9	153.9					
	11	-51.1	141.1					
	12	-65.6	155.6					
	13	-62.2	152.2					
	14	-59.8	149.8					
	15	-53.7	143.7					
	16	-45.3	135.3					
	17	-36.1	126.1					
	18	-32.6	122.6					
	19	-47.2	137.2					
	20	-45.0	135.0					
<i>Mean</i>		-53.0	143.0				143.0	
<i>Std Dev:</i>			10.8				10.8	

MSSS#	Dunes	Deg. Photoshop	Deg Azimuth	Streaks	Deg. Photoshop	Deg Azimuth	Overall I	Notes
M0203305				1	123.9	326.1		
				2	133.0	317.0		
				3	134.0	316.0		
				4	133.4	316.6		
				5	135.0	315.0		
				6	130.4	319.6		
				7	132.6	317.4		
				8	131.6	318.4		
				9	129.5	320.5		
				10	119.0	331.0		
				11	124.4	325.6		
				12	119.4	330.6		
				13	126.5	323.5		
				14	120.0	330.0		
				15	125.7	324.3		
				16	139.1	310.9		
				17	131.3	318.7		
				18	132.0	318.0		
				19	133.5	316.5		
<i>Mean</i>					129.2	320.8	320.8	
<i>Std Dev:</i>				#DIV/0!		5.7	5.7	

MSSS#	Dunes	Deg. Photoshop	Deg Azimuth	Streaks	Deg. Photoshop	Deg Azimuth	Overall I	Notes
M03-02054								Very interesting image. There are bright linear forms that almost look fluvial. Maybe they are just very large mega-ripples. There is a lobate splash crater as well. Yet, no sand and no crater streaks that I can see. No measurements

MSSS#	Dunes	Deg. Photoshop	Deg Azimuth	Streaks	Deg. Photoshop	Deg Azimuth	Overall I	Notes
M03-03634				1	-55.6	145.6		Bright ripples (not measured) and rayed craters. A few crater streaks found under heavy contrast.
				2	-58.5	148.5		
				3	-55.5	145.5		
				4	-53.5	143.5		
				5	-51.3	141.3		
				6	-57.6	147.6		
				7	-51.9	141.9		
				8	-52.4	142.4		
				9	-53.2	143.2		
<i>Mean</i>					-54.4	144.4	144.4	
<i>Std Dev:</i>						2.5	2.5	

MSSS#	Dunes	Deg. Photoshop	Deg Azimuth	Streaks	Deg. Photoshop	Deg Azimuth	Overall I	Notes
M04-02035								Bright ripples only. No measurements

MSSS#	Dunes	Deg. Photoshop	Deg Azimuth	Streaks	Deg. Photoshop	Deg Azimuth	Overall I	Notes
M04-03624								No measurements - no features of interest in this study.

MSSS#	Dunes	Deg. Photoshop	Deg Azimuth	Streaks	Deg. Photoshop	Deg Azimuth	Overall I	Notes
M09-00699								No measurements - no features of interest in this study.

MSSS#	Dunes	Deg. Photoshop	Deg Azimuth	Streaks	Deg. Photoshop	Deg Azimuth	Overall I	Notes
M07-02974	1	-89.2	179.2	1	-85.3	175.3		Very complex wind regime. Measurements not consistent
	2	-58.1	148.1					
	3	-119.5	209.5					
	4	-131.8	221.8					
	5	-137.2	227.2					

6	-142.2	232.2						enough to split the image.
7	-149.2	239.2						
8	-152.1	242.1						
9	-158.0	248.0						
10	-171.4	261.4						
11	-146.7	236.7						
12	-114.5	204.5						
13	-122.2	212.2						
<i>Mean</i>	-130.2	220.2			-85.3	175.3	217.0	
<i>Std Dev:</i>		30.4				NA	31.6	

MSSS#	Dunes	Deg. Photoshop	Deg Azimuth	Streaks	Deg. Photoshop	Deg Azimuth	Overall I	Notes
M07-01919	1	-116.7	206.7	1	-110.8	200.8		Poor Image quality
	2	-117.4	207.4					
	3	-109.9	199.9					
	4	-114.8	204.8					
<i>Mean</i>		-114.7	204.7		-110.8	200.8	203.9	
<i>Std Dev:</i>			3.4			0.0	3.4	

MSSS#	Dunes	Deg. Photoshop	Deg Azimuth	Streaks	Deg. Photoshop	Deg Azimuth	Overall I	Notes
M07-05959	1	-99.6	189.6	1	-113.9	203.9		Very long image, I was going to split it based on this, but the directions do not vary enough and most measurements were made in the center of the image. Should be OK on the overall map.
	2	-109.0	199.0	2	-113.9	203.9		
				3	-112.7	202.7		
				4	-106.0	196.0		
				5	-94.5	184.5		
				6	-105.9	195.9		
				7	-98.5	188.5		
				8	-96.8	186.8		
<i>Mean</i>		-104.3	194.3		-105.3	195.3	195.1	
<i>Std Dev:</i>			6.6			7.9	7.3	

MSSS#	Dunes	Deg. Photoshop	Deg Azimuth	Streaks	Deg. Photoshop	Deg Azimuth	Overall I	Notes
M08-03208								

MSSS#	Dunes	Deg. Photoshop	Deg Azimuth	Streaks	Deg. Photoshop	Deg Azimuth	Overall I	Notes
M08-06611	1	-82.2	172.2					
	2	-85.8	175.8					
	3	-84.3	174.3					
	4	-76.8	166.8					
	5	-83.7	173.7					
	6	-84.5	174.5					
	7	-84.2	174.2					
	8	-84.2	174.2					
	9	-85.2	175.2					
	10	-84.3	174.3					
	11	-84.8	174.8					
	12	-93.9	183.9					
	13	-91.0	181.0					
	14	-92.0	182.0					
	15	-86.8	176.8					
	16	-89.8	179.8					
<i>Mean</i>		-85.8	175.8				175.8	
<i>Std Dev:</i>			4.2				4.2	

MSSS#	Dunes	Deg. Photoshop	Deg Azimuth	Streaks	Deg. Photoshop	Deg Azimuth	Overall I	Notes
M10-01789								Not enough to infer directions from

MSSS#	Dunes	Deg. Photoshop	Deg Azimuth	Streaks	Deg. Photoshop	Deg Azimuth	Overall I	Notes
M11-02107	1	-66.2	156.2					Bi Directional winds. I went ahead and split the image although its not exactly representative its better than not doing it at all.
	2	-58.4	148.4					
	3	-59.3	149.3					
	4	-59.5	149.5					
	5	-64.9	154.9					
	6	-69.3	159.3					
	7	-61.1	151.1					
	8	-148.4	238.4					
	9	-139.5	229.5					
	9B	-147.2	237.2					
	10	-147.4	237.4					
	11	-149.3	239.3					
	<i>Mean</i>	-97.5	187.5				187.5	
	<i>Std Dev:</i>		43.3				43.3	
	12	-145.7	235.7					
	13	165.1	284.9					
	14	167.4	282.6					
	15	-174.1	264.1					
	16	-136.5	226.5					
	17	-179.3	269.3					
	<i>Mean</i>	-50.5	260.5				260.5	
	<i>Std Dev:</i>		24.3				24.3	

MSSS#	Dunes	Deg. Photoshop	Deg Azimuth	Streaks	Deg. Photoshop	Deg Azimuth	Overall I	Notes
M12-00672				1	-123.3	213.3		A few very faint streaks
				2	-121.5	211.5		
				3	-114.3	204.3		
				4	-121.5	211.5		
				5	-123	213.0		
				<i>Mean</i>	-120.7	210.7	210.7	
				<i>Std Dev:</i>		3.7	3.7	

MSSS#	Dunes	Deg. Photoshop	Deg Azimuth	Streaks	Deg. Photoshop	Deg Azimuth	Overall I	Notes
M13-00630				1	-113.4	203.4		A few faint crater streaks under heavy contrast adjustment
				2	-112.8	202.8		
				3	-118.5	208.5		
				4	-120.0	210.0		
				5	-118.0	208.0		
				<i>Mean</i>	-116.5	206.5	206.5	
				<i>Std Dev:</i>		3.2	3.2	

MSSS#	Dunes	Deg. Photoshop	Deg Azimuth	Streaks	Deg. Photoshop	Deg Azimuth	Overall I	Notes
M14-00754				1	-87.6	177.6		Again, A few faint crater streaks under heavy contrast adjustment
				2	-86.5	176.5		
				3	-90.0	180.0		
				4	-90.0	180.0		
				5	-93.5	183.5		
				6	-92.8	182.8		
				<i>Mean</i>	-90.1	180.1	180.1	
				<i>Std Dev:</i>		2.8	2.8	

MSSS#	Dunes	Deg. Photoshop	Deg Azimuth	Streaks	Deg. Photoshop	Deg Azimuth	Overall I	Notes
-------	-------	----------------	-------------	---------	----------------	-------------	-----------	-------

M15-01486	Image not map oriented and has no indicators of use
-----------	---

MSSS#	Dunes	Deg. Photoshop	Deg Azimuth	Streaks	Deg. Photoshop	Deg Azimuth	Overall I	Notes
M18-00644	1	-92.9	182.9	1	-96.0	186.0		
				2	-97.9	187.9		
				3	-96.7	186.7		
				4	-102.4	192.4		
				5	-98.2	188.2		
				6	-92.3	182.3		
				7	-92.6	182.6		
<i>Mean</i>		-92.9	182.9		-96.6	186.6	186.1	
<i>Std Dev:</i>			0.0			3.5	3.5	

MSSS#	Dunes	Deg. Photoshop	Deg Azimuth	Streaks	Deg. Photoshop	Deg Azimuth	Overall I	Notes
M19-00489								Image very noisy. Saw two faint crater streaks in what appears to be a topographic low. Not measured because I can be sure they are representative of the area.

MSSS#	Dunes	Deg. Photoshop	Deg Azimuth	Streaks	Deg. Photoshop	Deg Azimuth	Overall I	Notes
M20-01590								nothing - bad image

MSSS#	Dunes	Deg. Photoshop	Deg Azimuth	Streaks	Deg. Photoshop	Deg Azimuth	Overall I	Notes
M21-00018	1	-75.6	165.6					Nice Image Wind direction is different in bottom half of image than in top. South half of image had to be split a second time.
	2	-75.1	165.1					
	3	-75.7	165.7					
	4	-73.1	163.1					
	5	-76.3	166.3					
	6	-72.1	162.1					
	7	-74.9	164.9					
	8	-73.8	163.8					
	9	-73.8	163.8					
	10	-75.9	165.9					
	11	-79.5	169.5					
	12	-77.0	167.0					
	13	-78.7	168.7					
<i>Mean</i>		-75.5	165.5				165.5	
<i>Std Dev:</i>							2.1	
	14	-75.3	165.3					
	15	-68.7	158.7					
	16	-84.1	174.1					
	17	-70.3	160.3					
	18	-69.0	159.0					
	19	-69.8	159.8					
	20	-67.6	157.6					
	21	-44.2	134.2					

22	-71.1	161.1		
23	-56.5	146.5		
24	-59.3	149.3		
25	-66.7	156.7		
<i>Mean</i>	-66.9	156.9		156.9
<i>Std Dev:</i>		10.0	#DIV/0!	10.0
26	-42.8	132.8		
27	-38.5	128.5		
28	-36.4	126.4		
29	-70.5	160.5		
30	-65.7	155.7		
31	-57.1	147.1		
32	-56.6	146.6		
33	-46.1	136.1		
34	-48.9	138.9		
35	-52.5	142.5		
36	-51.4	141.4		
37	-45.3	135.3		
38	-53.3	143.3		
39	-46.0	136.0		
<i>Mean</i>	-50.8	140.8		140.8
<i>Std Dev:</i>		9.6	#DIV/0!	9.6

MSSS#	Dunes	Deg. Photoshop	Deg Azimuth	Streaks	Deg. Photoshop	Deg Azimuth	Overall I	Notes
M22-02419								nothing

MSSS#	Dunes	Deg. Photoshop	Deg Azimuth	Streaks	Deg. Photoshop	Deg Azimuth	Overall I	Notes
M23-00263	1	-74.4	164.4					Good image. A bit less than a 10 degree variation from north to south, so no split
	2	-73.8	163.8					
	3	-72.6	162.6					
	4	-75.8	165.8					
	5	-71.9	161.9					
	6	-66.0	156.0					
	7	-69.5	159.5					
	8	-69.0	159.0					
	9	-70.3	160.3					
	10	-68.0	158.0					
	11	-68.3	158.3					
	12	-68.6	158.6					
	13	-69.5	159.5					
	14	-65.7	155.7					
	15	-67.1	157.1					
	16	-68.0	158.0					
	17	-64.9	154.9					
	18	-68.3	158.3					
	19	-70.8	160.8					
	20	-69.6	159.6					
	21	-69.7	159.7					
	22	-74.1	164.1					
	23	-70.9	160.9					
	24	-69.8	159.8					
	25	-66.9	156.9					
	26	-70.1	160.1					
	27	-59.8	149.8					
	28	-61.8	151.8					
	29	-65.6	155.6					
	30	-64.3	154.3					
	31	-59.4	149.4					
	32	-66.2	156.2					
<i>Mean</i>		-68.5	158.5				158.5	

<i>Std Dev:</i>	3.9	#DIV/0!	3.9
-----------------	-----	---------	-----

MSSS#	Dunes	Deg. Photoshop	Deg Azimuth	Streaks	Deg. Photoshop	Deg Azimuth	Overall I	Notes
M23-00825	1	-91.3	181.3					
	2	-69.0	159.0					
	3	-82.8	172.8					
	4	-56.3	146.3					
	5	-109.2	199.2					
	6	-123.4	213.4					
	7	-128.3	218.3					
	8	-124.1	214.1					
	9	-125.5	215.5					
	10	-178.1	268.1					
	11	172.3	277.7					
	12	168.7	281.3					
	13	159.1	290.9					
	14	172.9	277.1					
	15	172.2	277.8					
	16	-157.4	247.4					
	17	-144.4	234.4					
	18	-131.2	221.2					
	19	-134.1	224.1					
	20	-122.0	212.0					
	21	-121.2	211.2					
<i>Mean</i>		-50.1	225.9				225.9	
<i>Std Dev:</i>			41.7				41.7	

MSSS#	Dunes	Deg. Photoshop	Deg Azimuth	Streaks	Deg. Photoshop	Deg Azimuth	Overall I	Notes
E01-01967								not map oriented and only have bright ripples. Not used

MSSS#	Dunes	Deg. Photoshop	Deg Azimuth	Streaks	Deg. Photoshop	Deg Azimuth	Overall I	Notes
E01-02211								not map oriented and only have bright ripples. Not used

MSSS#	Dunes	Deg. Photoshop	Deg Azimuth	Streaks	Deg. Photoshop	Deg Azimuth	Overall I	Notes
E02-00602	1	-115.0	205.0					Nice image. barchans and barchanoidal ridges
	2	-117.9	207.9					
	3	-110.2	200.2					
	4	-115.1	205.1					
	5	-121.3	211.3					
	6	-115.6	205.6					
	7	-114.6	204.6					
	8	-114.9	204.9					
	9	-114.2	204.2					
	10	-116.0	206.0					
	11	-115.7	205.7					
	12	-118.1	208.1					
	13	-116.6	206.6					
	14	-117.4	207.4					
	15	-114.4	204.4					
	16	-117.8	207.8					
	17	-120.0	210.0					
<i>Mean</i>		-116.2	206.2				206.2	

<i>Std Dev:</i>	2.5	2.5
-----------------	-----	-----

MSSS#	Dunes	Deg. Photoshop	Deg Azimuth	Streaks	Deg. Photoshop	Deg Azimuth	Overall I	Notes
E02-02816				1	-115.5	205.5		
				2	-117.5	207.5		
				3	-114.9	204.9		
				4	-113.8	203.8		
				5	-117.4	207.4		
				6	-124.9	214.9		
<i>Mean</i>					-117.3	207.3	207.3	
<i>Std Dev:</i>						4.0	4.0	

MSSS#	Dunes	Deg. Photoshop	Deg Azimuth	Streaks	Deg. Photoshop	Deg Azimuth	Overall I	Notes
E09-02803	1	-142.3	232.3					Image was not map oriented but appears to be projected properly. I realigned it. Appears to be some undeveloped barchans in the north, but I didn't risk the measurement because its not clear. Mainly barchanoidal ridges. I think the average will be OK but I won't trust one measurement alone. Dunes mainly in the North.
	2	-141.7	231.7					
	3	-150.1	240.1					
	4	-152.2	242.2					
	5	-152.9	242.9					
	6	-142.3	232.3					
	7	-142.8	232.8					
	8	-149.3	239.3					
	9	-138.3	228.3					
	10	-165.3	255.3					
	11	-155.3	245.3					
	12	-176.2	266.2					
	13	-174.8	264.8					
<i>Mean</i>		-152.6	242.6				242.6	
<i>Std Dev:</i>			12.5				12.5	

MSSS#	Dunes	Deg. Photoshop	Deg Azimuth	Streaks	Deg. Photoshop	Deg Azimuth	Overall I	Notes
E09-02804								There is a general NNW texture in the image - but no specific features I trust as good indicators.

MSSS#	Dunes	Deg. Photoshop	Deg Azimuth	Streaks	Deg. Photoshop	Deg Azimuth	Overall I	Notes
E10-00272	1	-105.9	195.9	1	-107.1	197.1		Nice image. The average for the dunes will be good, but the small barchan/barchanoid field is under topographic influence from a good sized crater.
	2	-100.2	190.2	2	-107.9	197.9		
	3	-97.8	187.8	3	-110.0	200.0		
	4	-97.1	187.1					
	5	-101.1	191.1					
	6	-103.4	193.4					
	7	-105.3	195.3					
	8	-107.7	197.7					
	9	-108.7	198.7					
	10	-110.4	200.4					
	11	-112.8	202.8					

12	-114.7	204.7			
13	-106.3	196.3			
14	-104.9	194.9			
15	-104.4	194.4			
16	-105.1	195.1			
17	-107.4	197.4			
<i>Mean</i>	-105.5	195.5	-108.3	198.3	195.9
<i>Std Dev:</i>		4.8		1.5	4.5

Measured a few crater streaks.

MSSS#	Dunes	Deg. Photoshop	Deg Azimuth	Streaks	Deg. Photoshop	Deg Azimuth	Overall I	Notes
E10-01396								Image contains some nice features. However, even after re-orientating it, its very obviously not map projected and oblique. No measurements taken

MSSS#	Dunes	Deg. Photoshop	Deg Azimuth	Streaks	Deg. Photoshop	Deg Azimuth	Overall I	Notes
E11-00157								Not Map oriented. Some transverse dunes in the image - but I can't tell which direction is the formative on. Image does appear to be map projected.

MSSS#	Dunes	Deg. Photoshop	Deg Azimuth	Streaks	Deg. Photoshop	Deg Azimuth	Overall I	Notes
E11-00527	1	-109.0	199.0	1	-113.1	203.1		Not oriented but projected (I think). I realigned. A few nice dunes and streaks. I stayed away from some seif dunes. There are bright ripples in craters. Wind variable but basically unidirectional
	2	-111.8	201.8	2	-115.7	205.7		
	3	-115.6	205.6	3	-118.2	208.2		
	4	-106.9	196.9	4	-119.7	209.7		
	5	-109.2	199.2	5	-120.8	210.8		
	6	-112.4	202.4					
	7	-108.9	198.9					
	8	-98.6	188.6					
<i>Mean</i>		-109.1	199.1		-117.5	207.5	202.3	
<i>Std Dev:</i>			5.0			3.1	6.0	

MSSS#	Dunes	Deg. Photoshop	Deg Azimuth	Streaks	Deg. Photoshop	Deg Azimuth	Overall I	Notes
E11-01859	1	-87.7	177.7	1	-112.7	202.7		Streaks in the southern
	2	-92.1	182.1	2	-124.1	214.1		

3	-98.2	188.2	3	-107.1	197.1	
4	-89.6	179.6				
5	-91.3	181.3				
6	-92.8	182.8				
7	-97.6	187.6				
8	-87.5	177.5				
9	-89.0	179.0				
10	-84.5	174.5				
11	-89.6	179.6				
12	-93.0	183.0				
13	-84.3	174.3				
<i>Mean</i>	-90.6	180.6		-114.6	204.6	185.1
<i>Std Dev:</i>		4.3			8.7	10.9

extreme a bit different than dune indications. Average should be OK though.

MSSS#	Dunes	Deg. Photoshop	Deg Azimuth	Streaks	Deg. Photoshop	Deg Azimuth	Overall I	Notes
E16-01318	1	-133.6	223.6	1	-146.5	236.5		Image appear map projected but not oriented. I oriented it.
	2	-142.5	232.5	2	-145.5	235.5		
	3	-135.0	225.0	3	-124.5	214.5		
	4	-134.0	224.0	4	-128.7	218.7		
	5	-136.8	226.8	5	-139.8	229.8		
	6	-127.4	217.4	6	-126.8	216.8		
	7	-134.0	224.0	7	-135.0	225.0		
	8	-133.8	223.8					
	9	-128.1	218.1					
	10	-153.9	243.9					
<i>Mean</i>		-135.9	225.9		-135.3	225.3	225.6	
<i>Std Dev:</i>			7.6			9.0	7.9	

MSSS#	Dunes	Deg. Photoshop	Deg Azimuth	Streaks	Deg. Photoshop	Deg Azimuth	Overall I	Notes
R01-01236								This is the same image as M00-03222. So its not analyzed for wind direction.

MSSS#	Dunes	Deg. Photoshop	Deg Azimuth	Streaks	Deg. Photoshop	Deg Azimuth	Overall I	Notes
R03-00358								This is basically the same image as M02-00612. So its not analyzed for wind direction.

MSSS#	Dunes	Deg. Photoshop	Deg Azimuth	Streaks	Deg. Photoshop	Deg Azimuth	Overall I	Notes
R04-00598								Again, basically the same image as FHA-03181 and not analyzed for direction

MSSS#	Dunes	Deg. Photoshop	Deg Azimuth	Streaks	Deg. Photoshop	Deg Azimuth	Overall I	Notes
R05-00941	1	-96.1	186.1	1	-97.1	187.1		Barchans and sand shadows/strea
	2	-97.0	187.0	2	-96.1	186.1		
	3	-97.2	187.2	3	-98.5	188.5		

	4	-99.8	189.8	4	-97.4	187.4		ks mainly
<i>Mean</i>		-97.5	187.5		-97.3	187.3	187.4	
<i>Std Dev:</i>			1.6			1.0	1.2	

	Dunes	Streaks	total obs.	Overall I	
Ttl. Cnts.	291	141	432	101.1	Degrees

APPENDIX C

ANNOTATED MSSS MOC NA IMAGES.

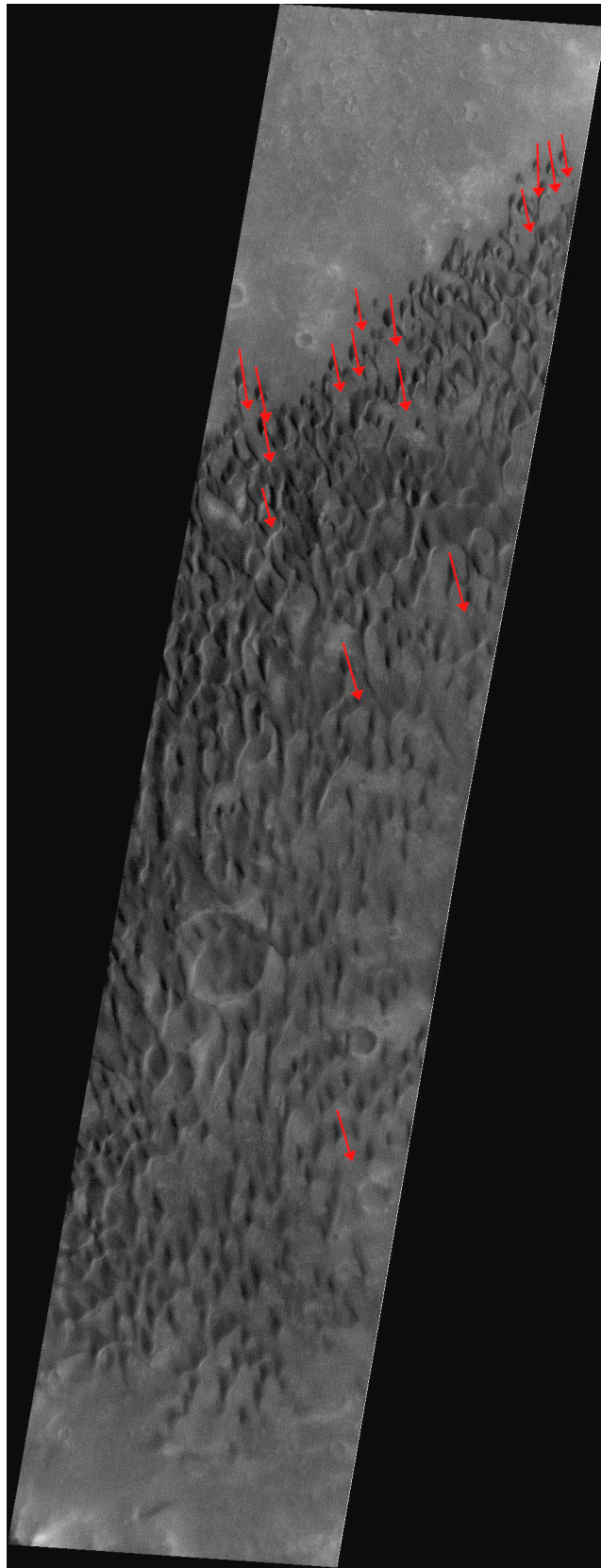


Figure C-1. MSSS MOC NA image SP36507 annotated

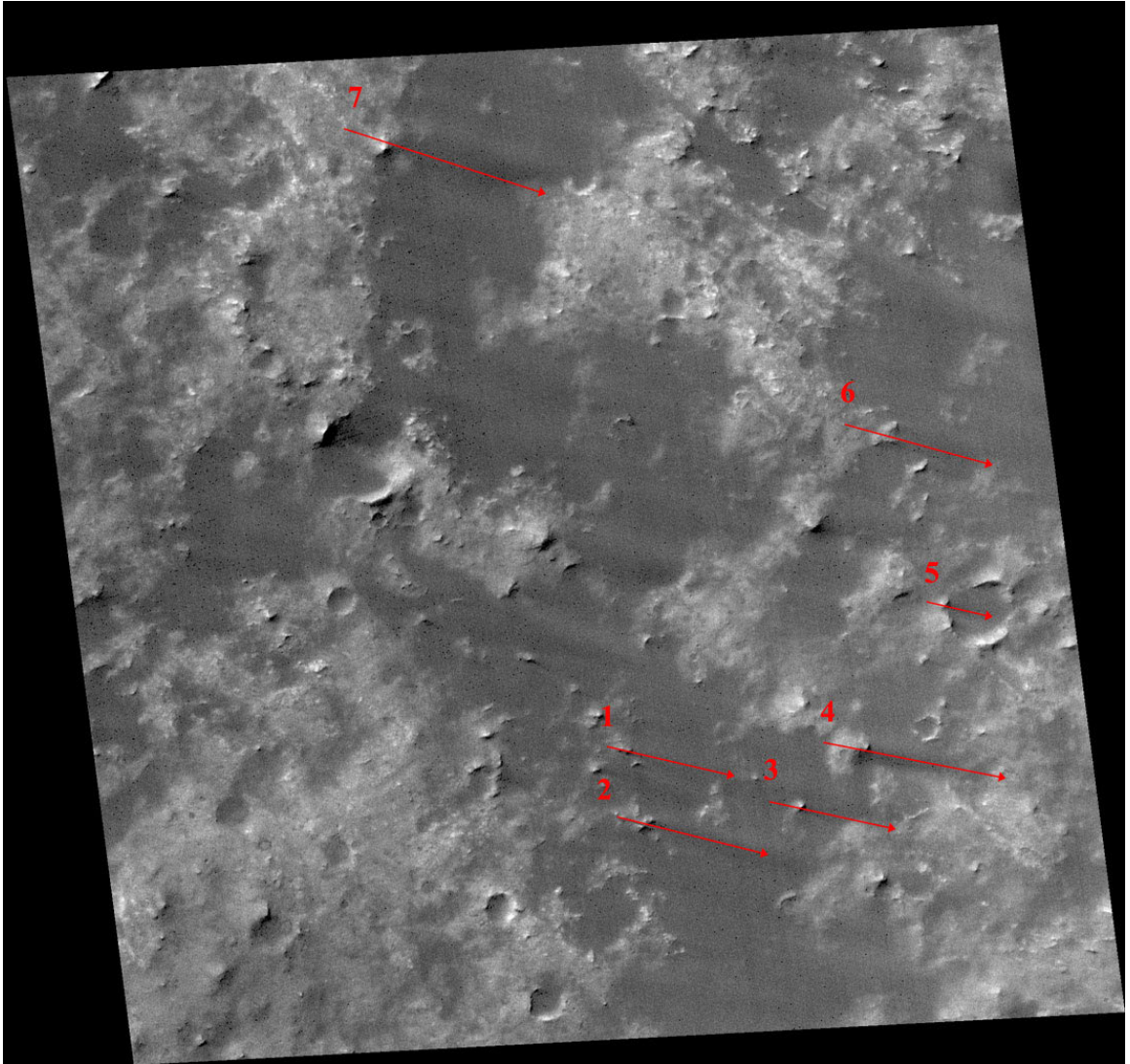


Figure C-2. MSSS MOC NA image FHA00473 annotated

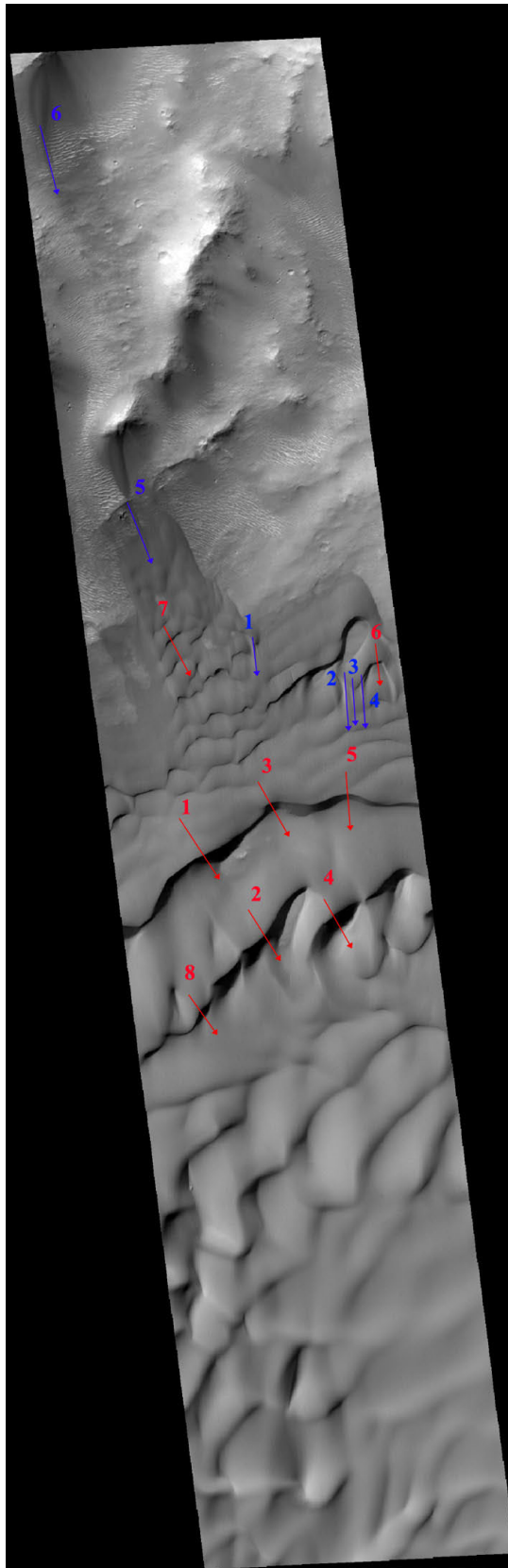


Figure C-3. MSSS MOC NA image FHA01381 annotated

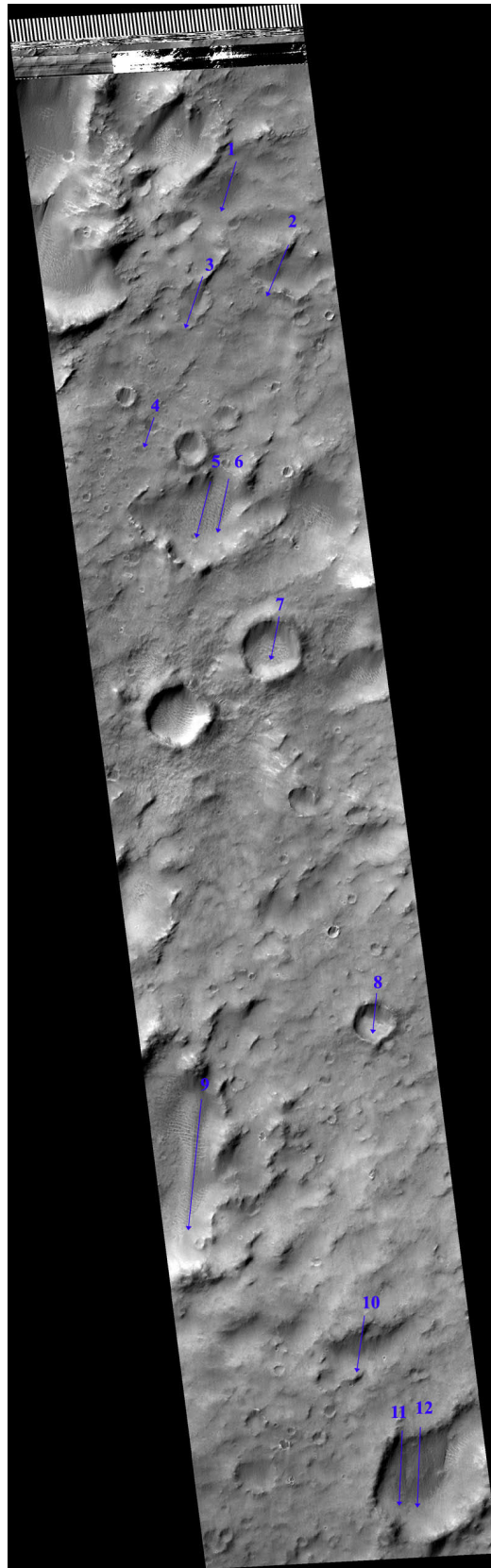


Figure C-4. MSSS MOC NA image M0000790 annotated

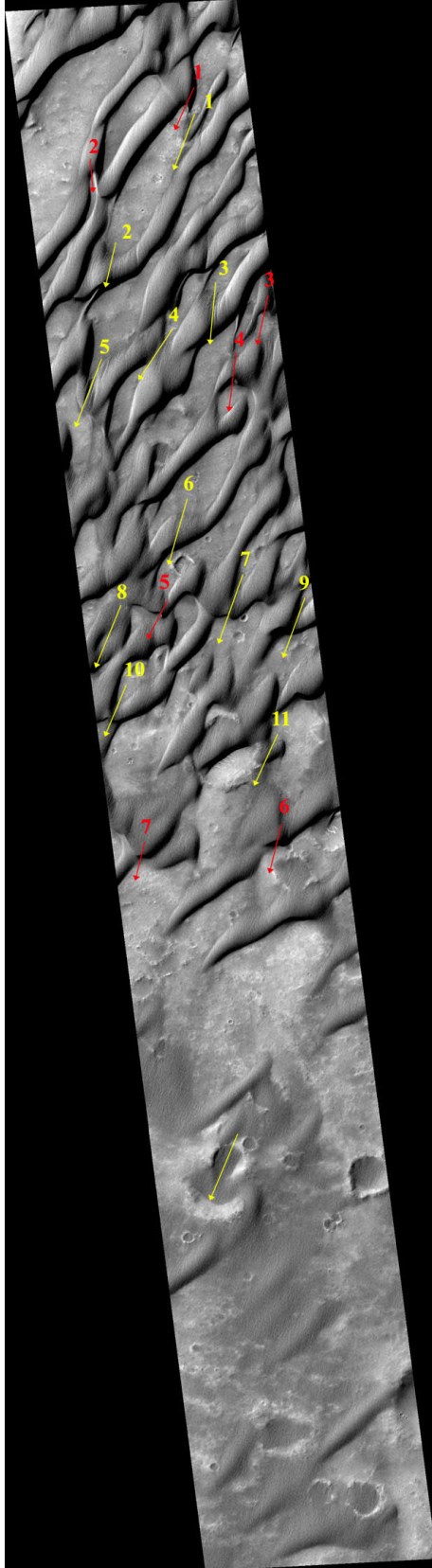


Figure C-5. MSSS MOC NA image M0003228 annotated

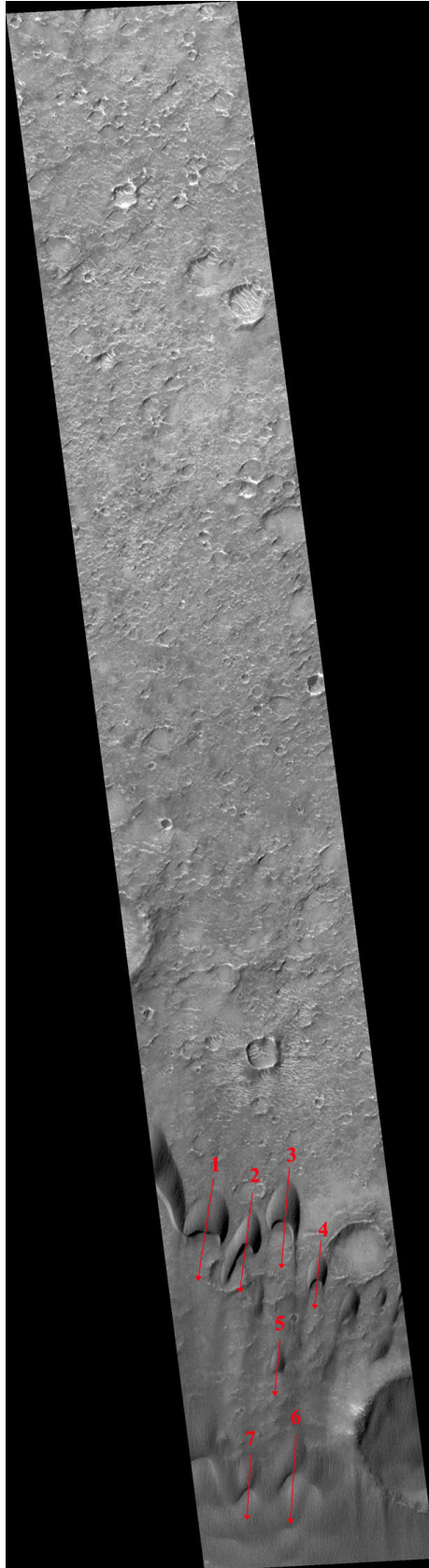


Figure C-6. MSSS MOC NA image M0200612 annotated

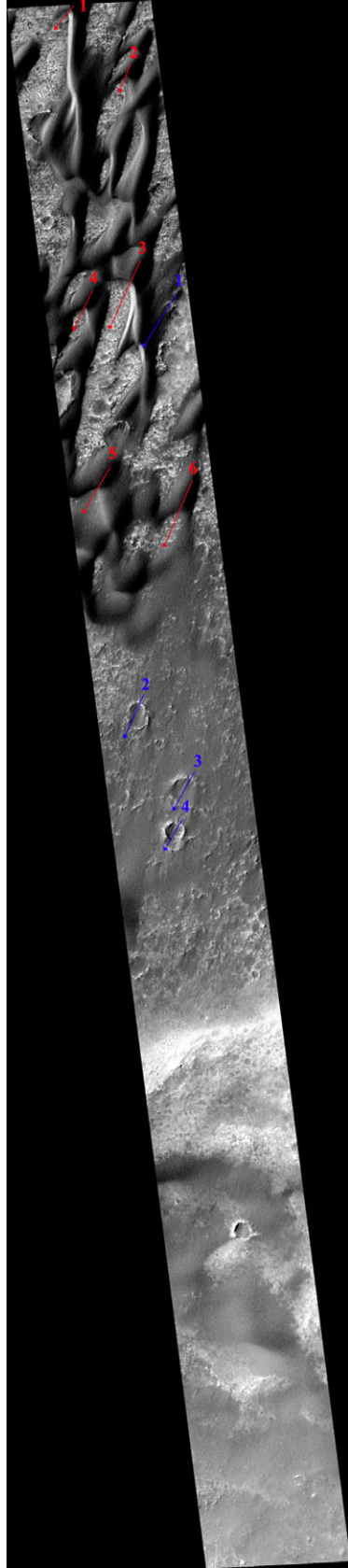


Figure C-7. MSSS MOC NA image M0201996 annotated

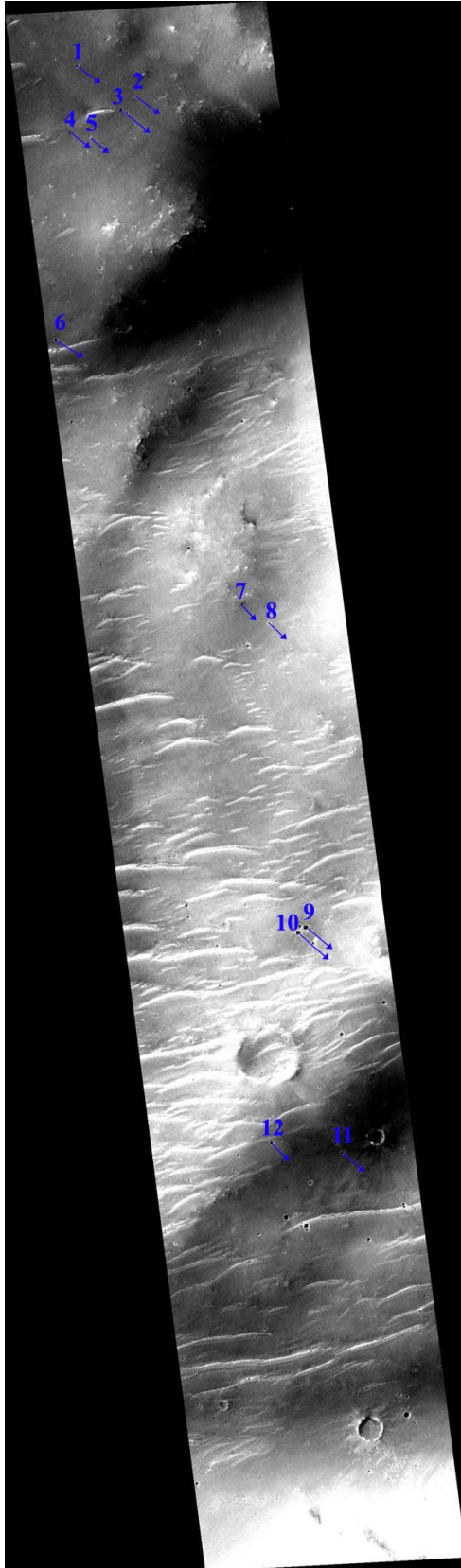


Figure C-8. MSSS MOC NA image M0201998 annotated

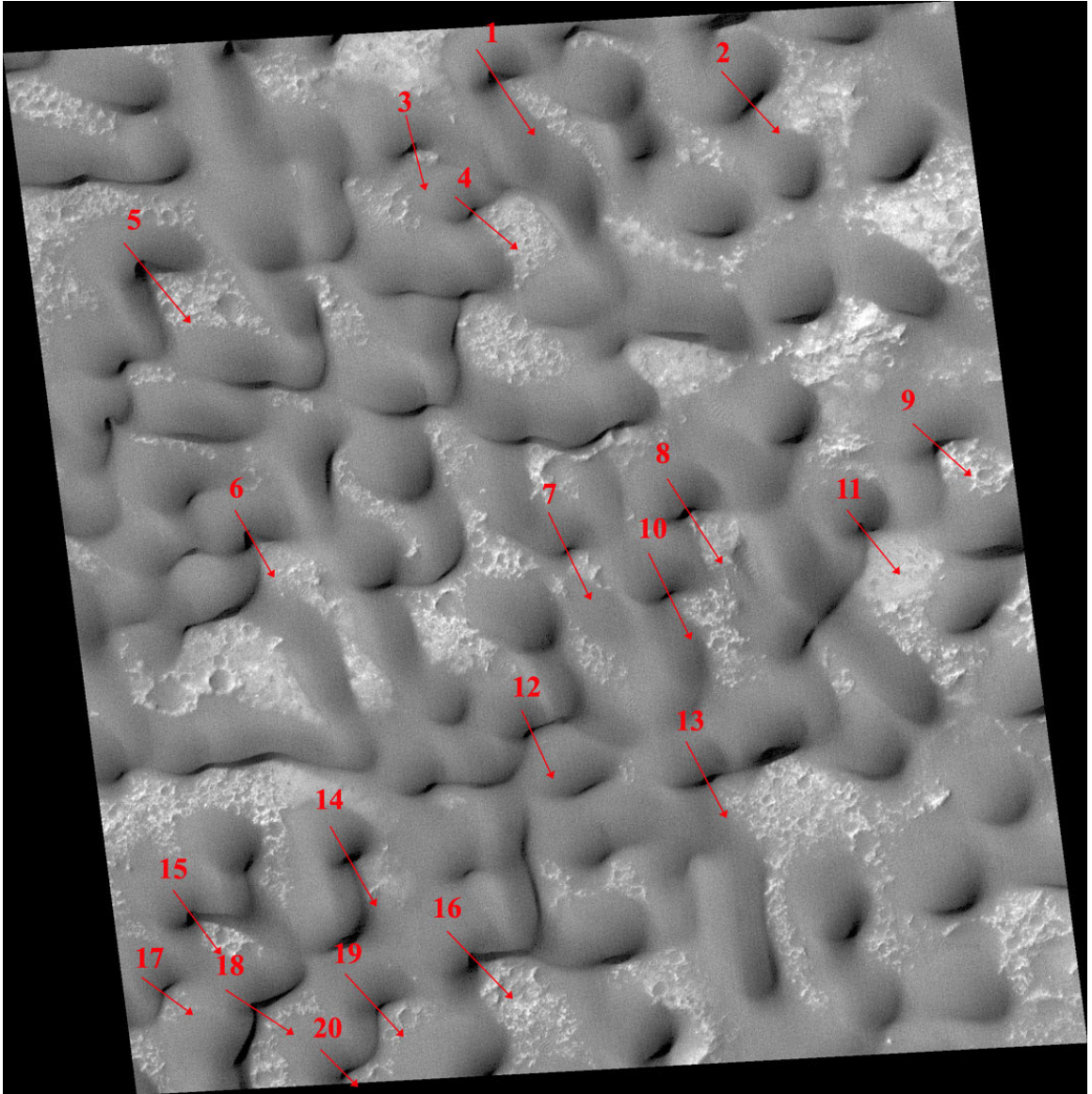


Figure C-9. MSSS MOC NA image M0202819 annotated

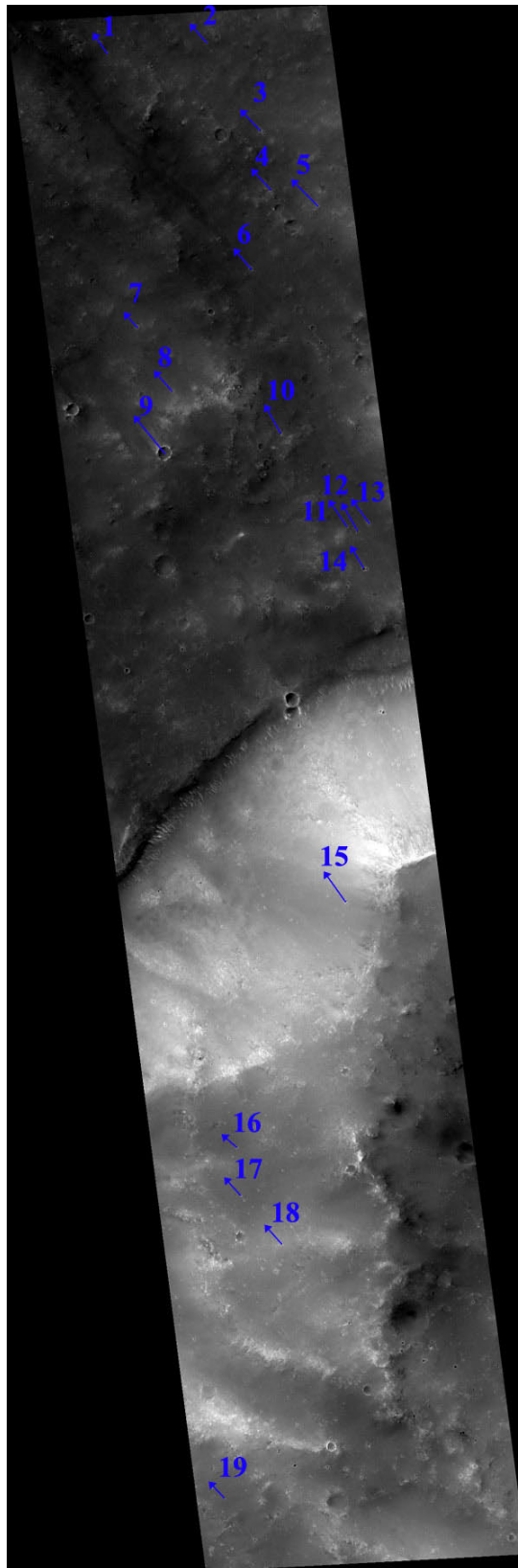


Figure C-10. MSSS MOC NA image M0203305 annotated

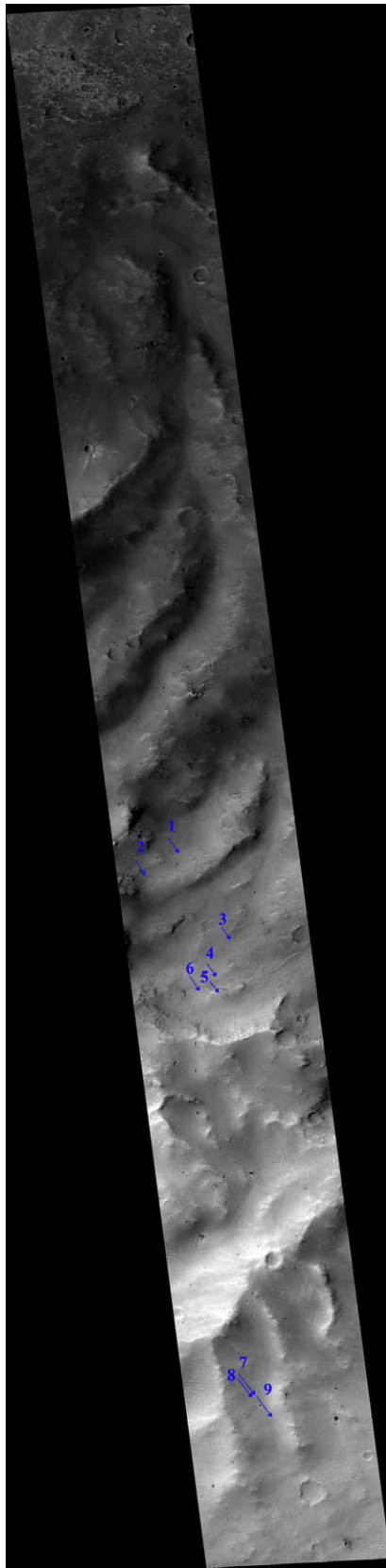


Figure C-11. MSSS MOC NA image M0303634 annotated

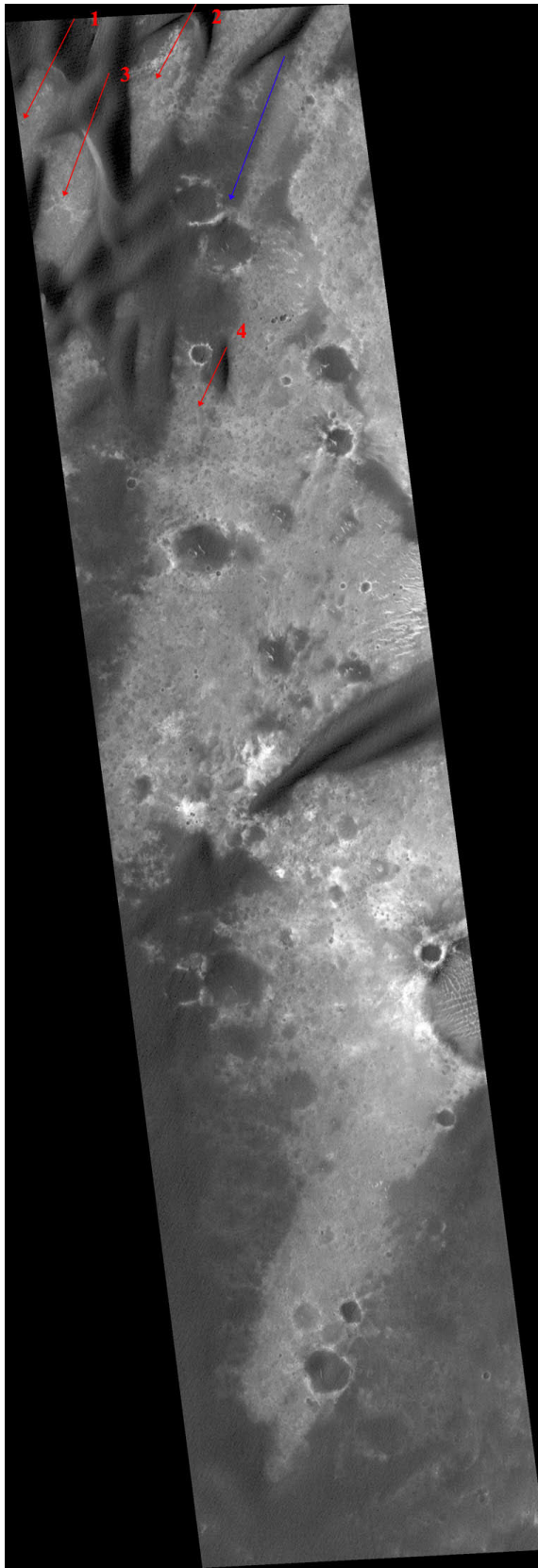


Figure C-12. MSSS MOC NA image M0701919 annotated

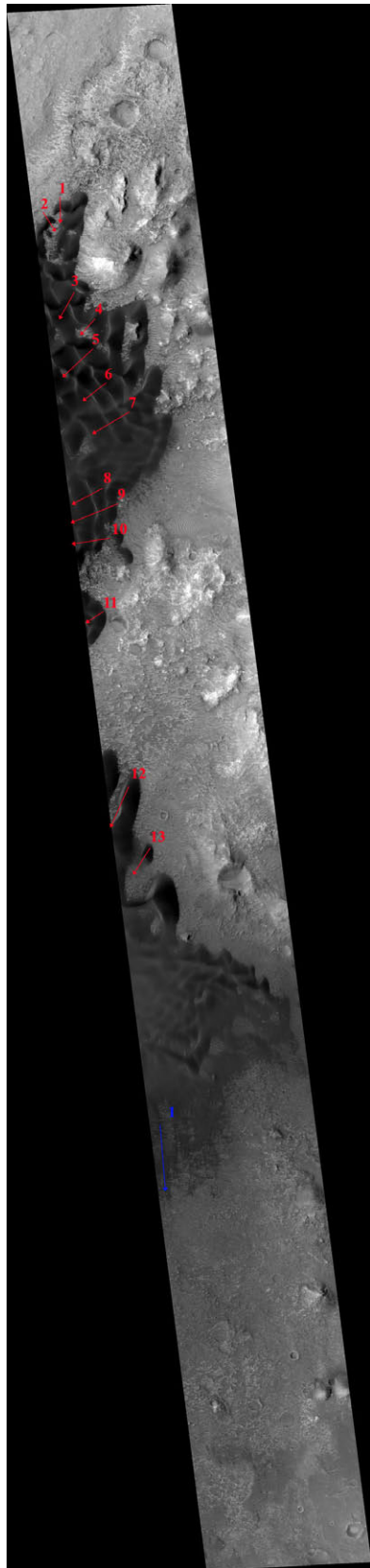


Figure C-13. MSSS MOC NA image M0702974 annotated

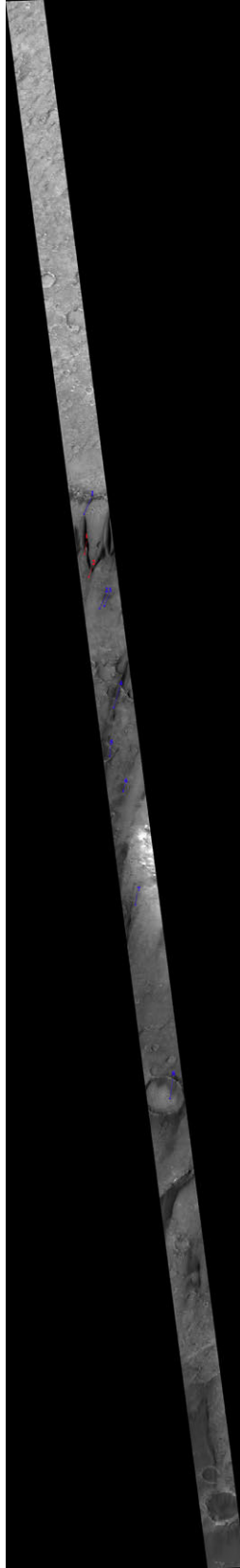


Figure C-14. MSSS MOC NA image M0705959 annotated

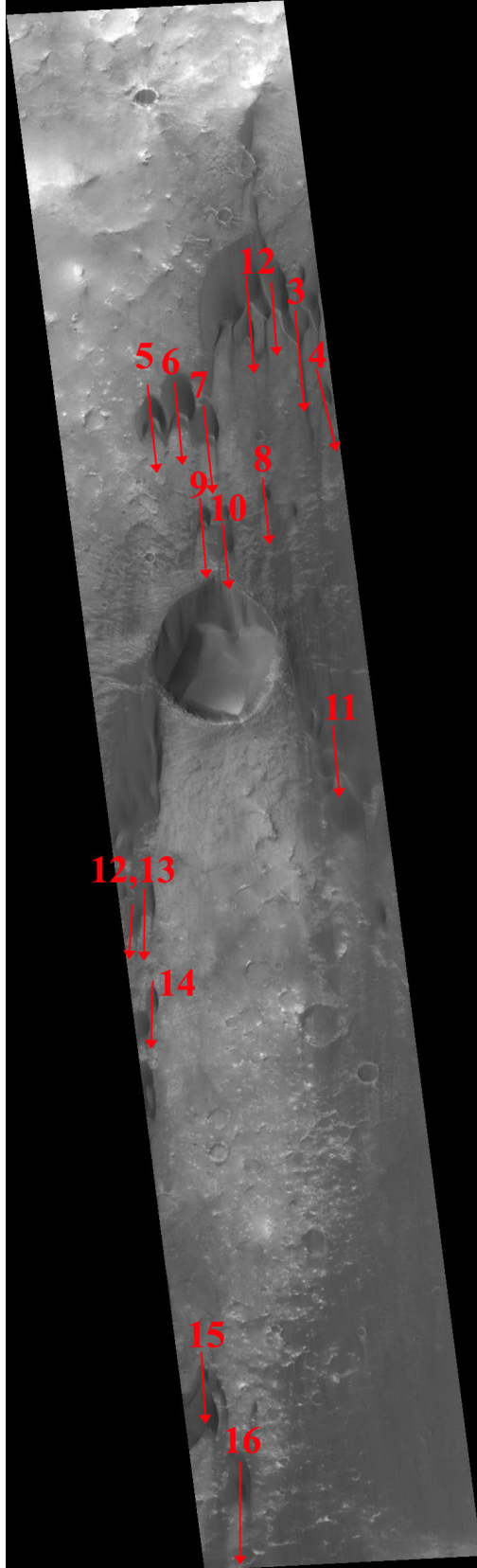


Figure C-15. MSSS MOC NA image M0806611 annotated

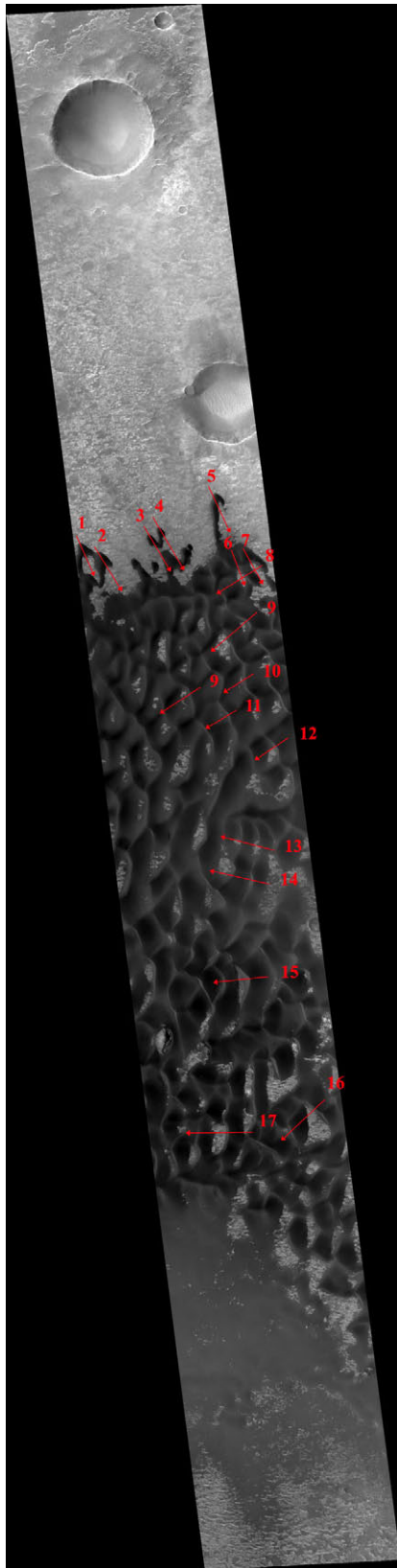


Figure C-16. MSSS MOC NA image M1102107 annotated

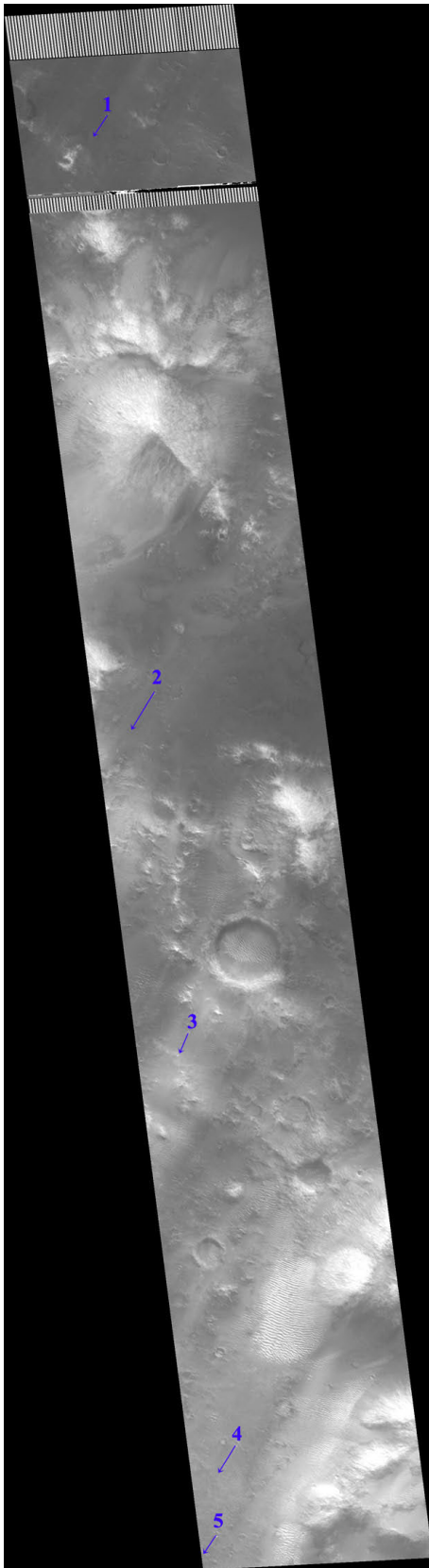


Figure C-17. MSSS MOC NA image M1200672 annotated

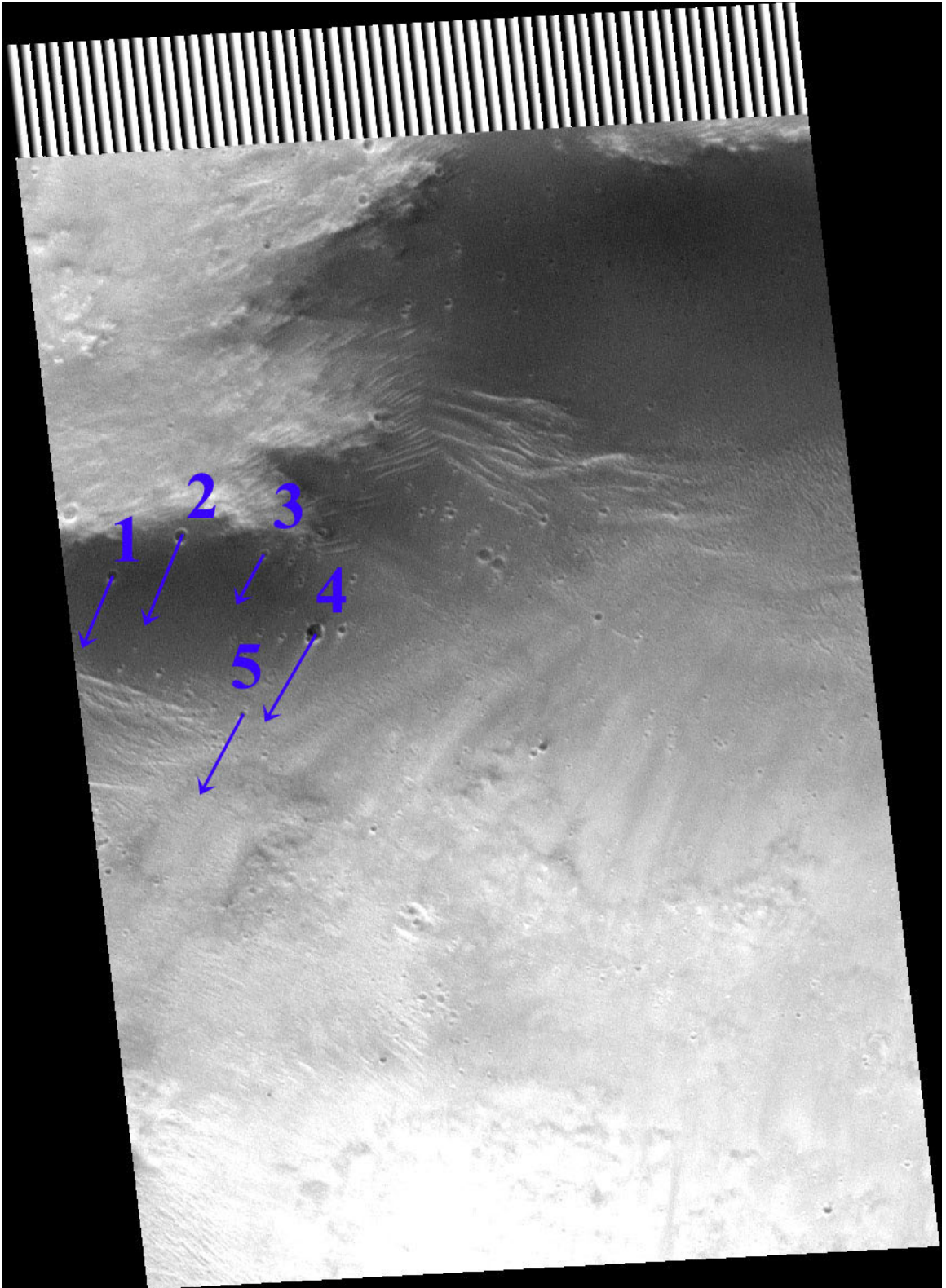


Figure C-18. MSSS MOC NA image M1300630 annotated

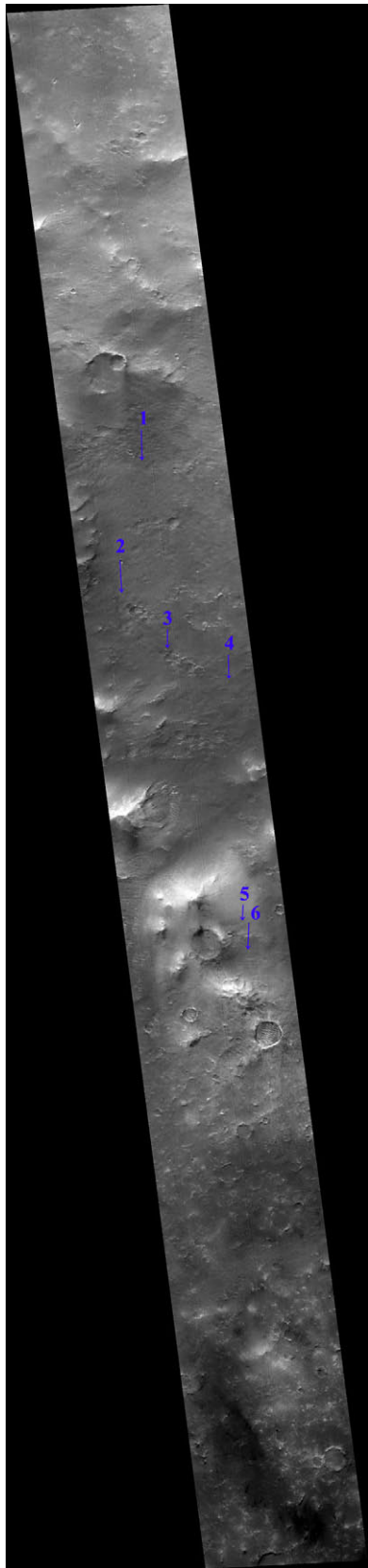


Figure C-19. MSSS MOC NA image M1400754 annotated

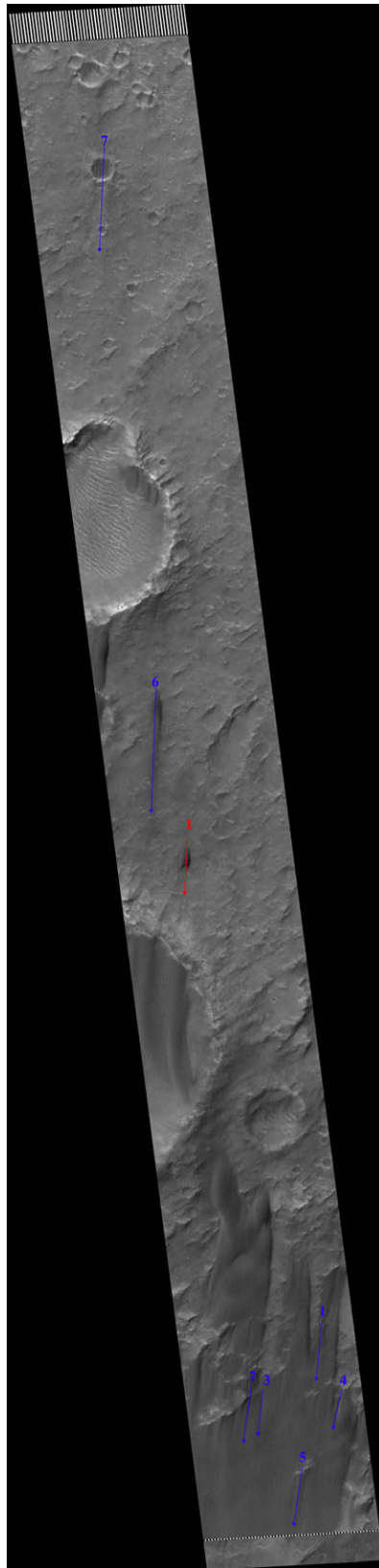


Figure C-20. MSSS MOC NA image M1800644 annotated

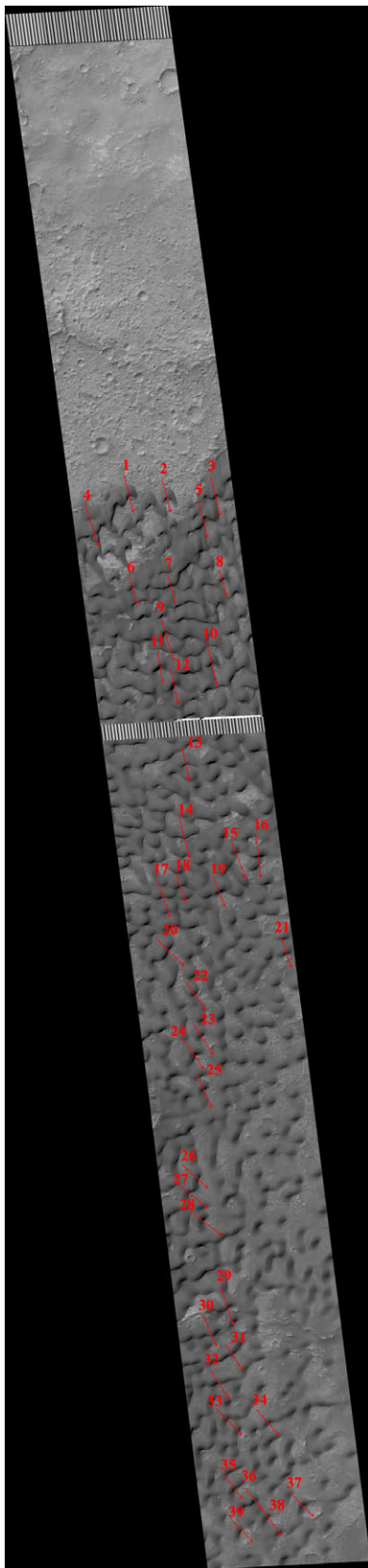


Figure C-21. MSSS MOC NA image M2100018 annotated

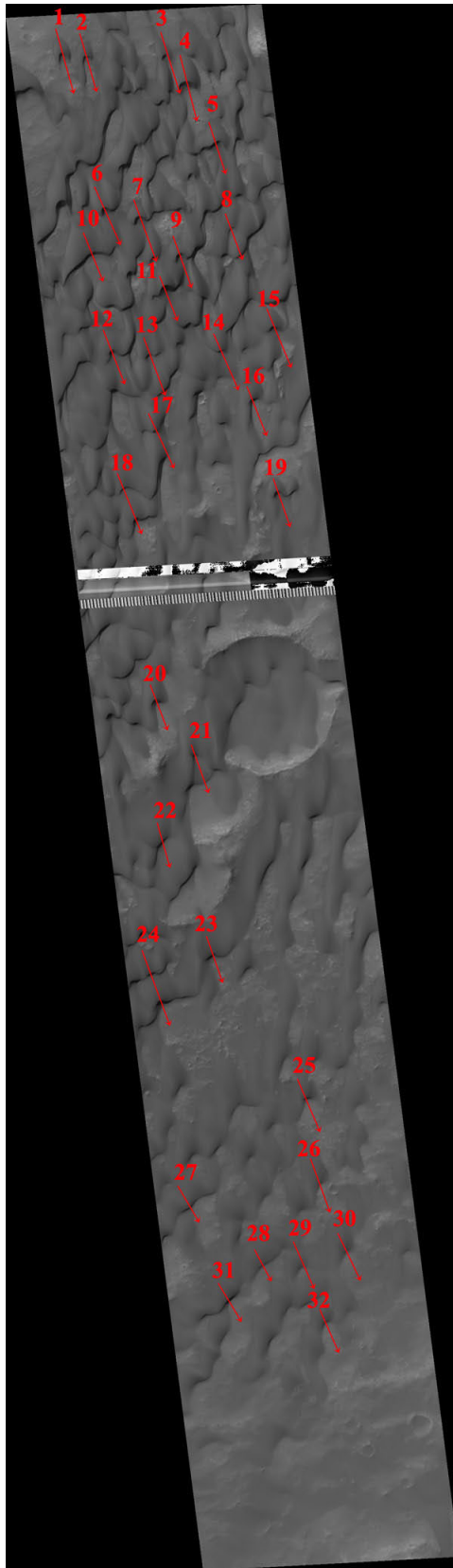


Figure C-22. MSSS MOC NA image M2300263 annotated

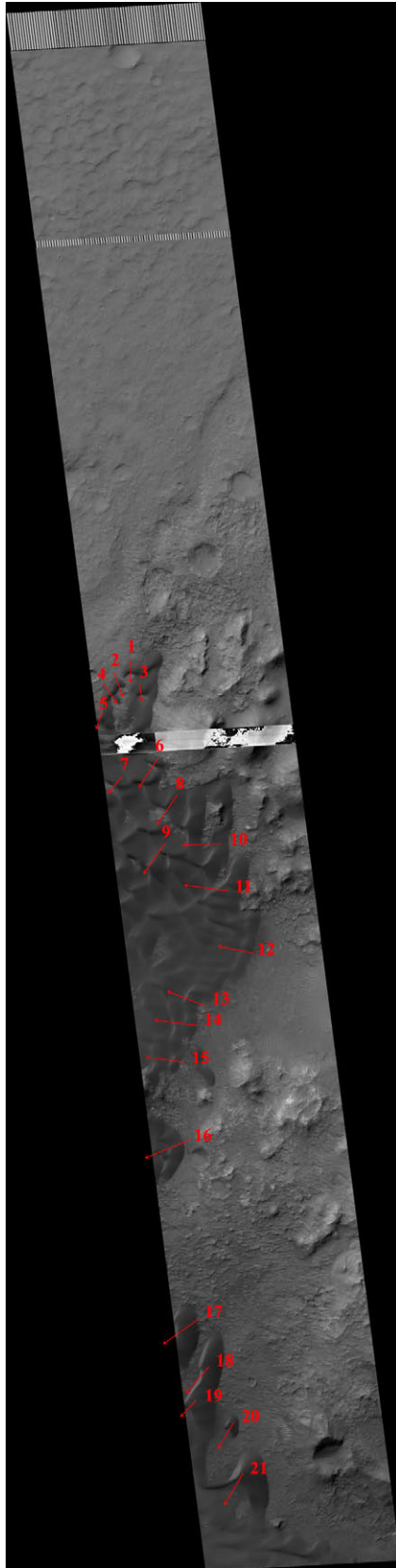


Figure C-23. MSSS MOC NA image M2300825 annotated

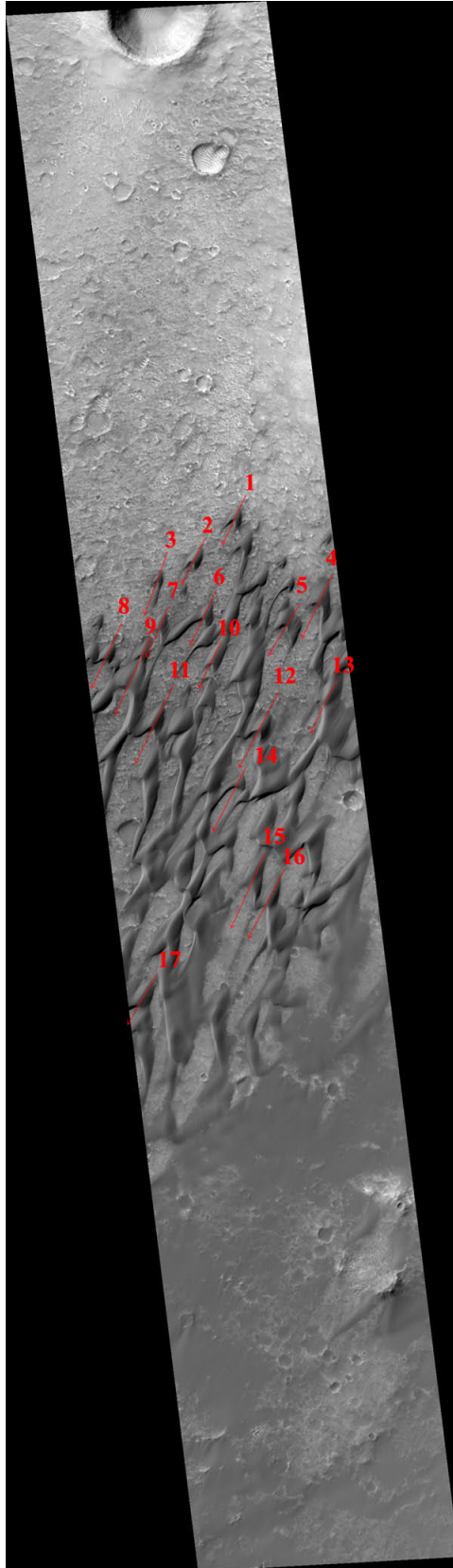


Figure C-24. MSSS MOC NA image E0200602 annotated

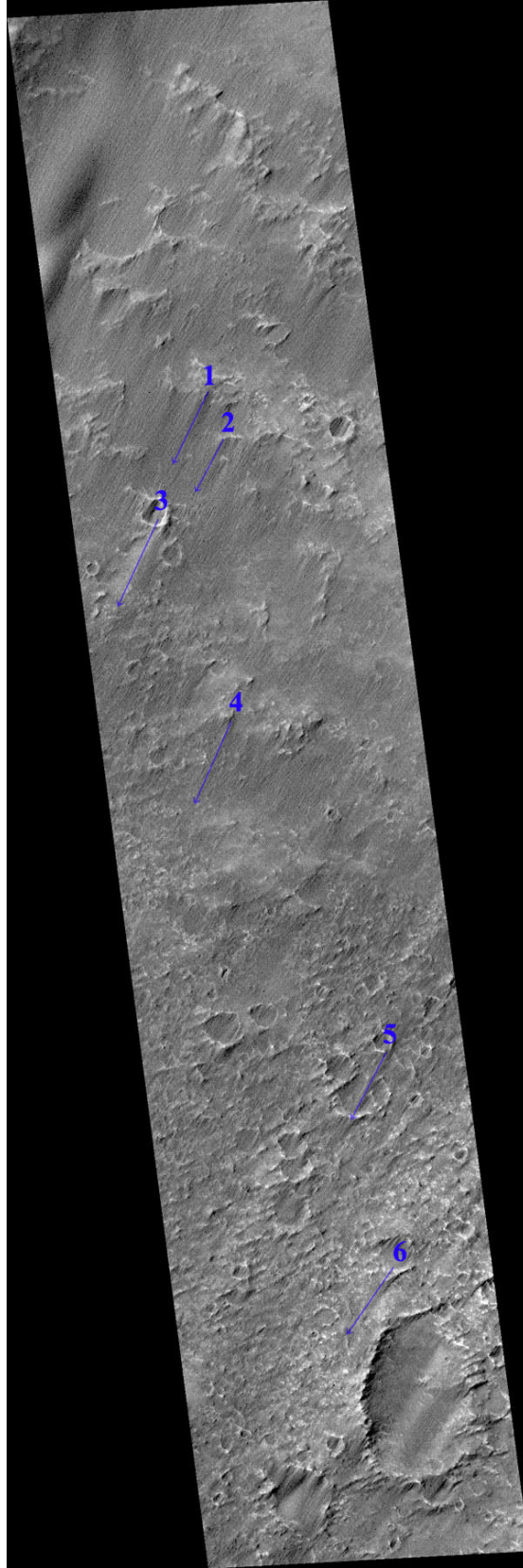


Figure C-25. MSSS MOC NA image E0202816 annotated



Figure C-26. MSSS MOC NA image E0902803 annotated

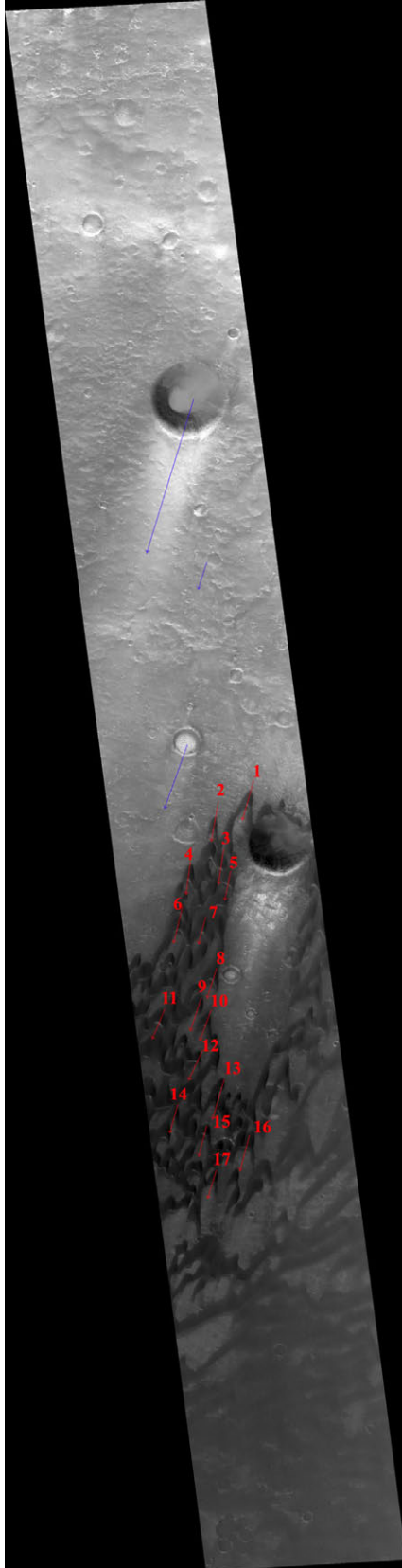


Figure C-27. MSSS MOC NA image E1000272 annotated

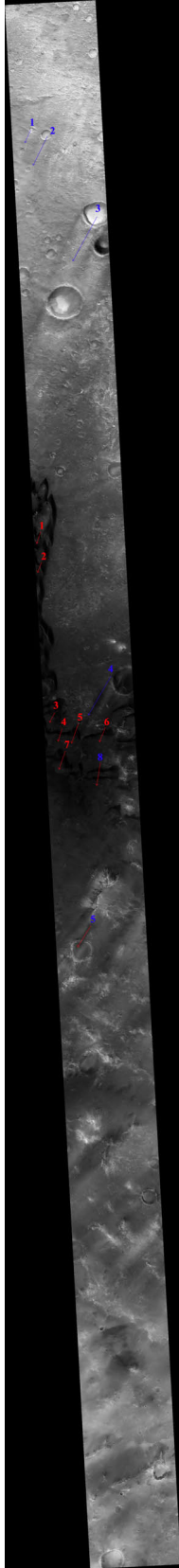


Figure C-28. MSSS MOC NA image E1100527 annotated

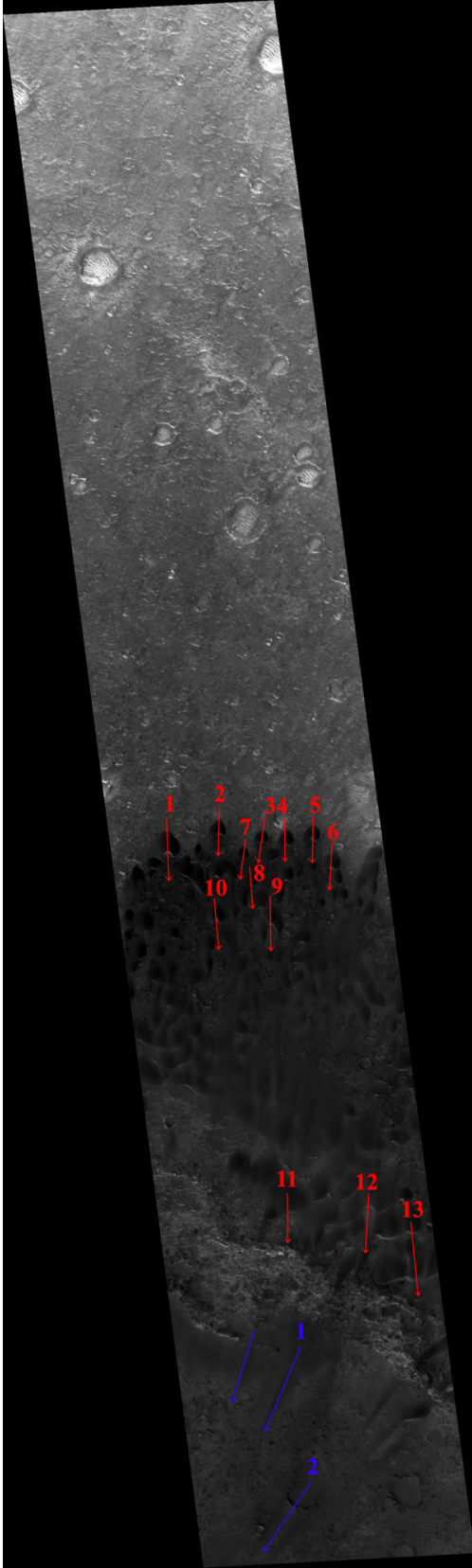


Figure C-29. MSSS MOC NA image E1101359 annotated

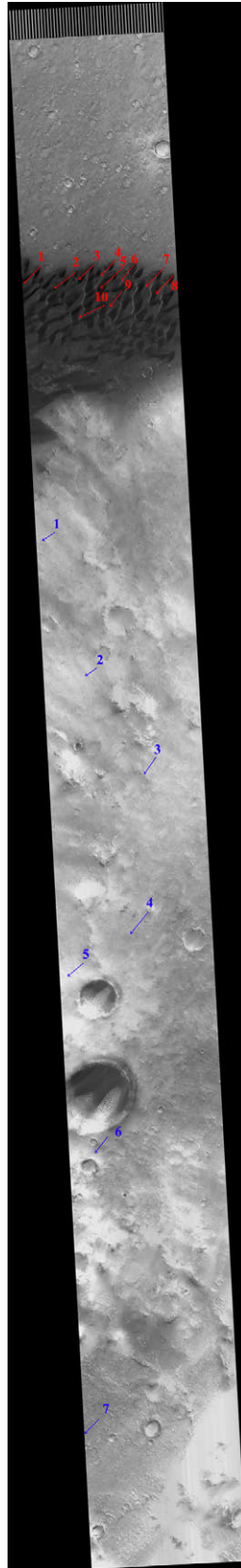


Figure C-30. MSSS MOC NA image E1601318 annotated

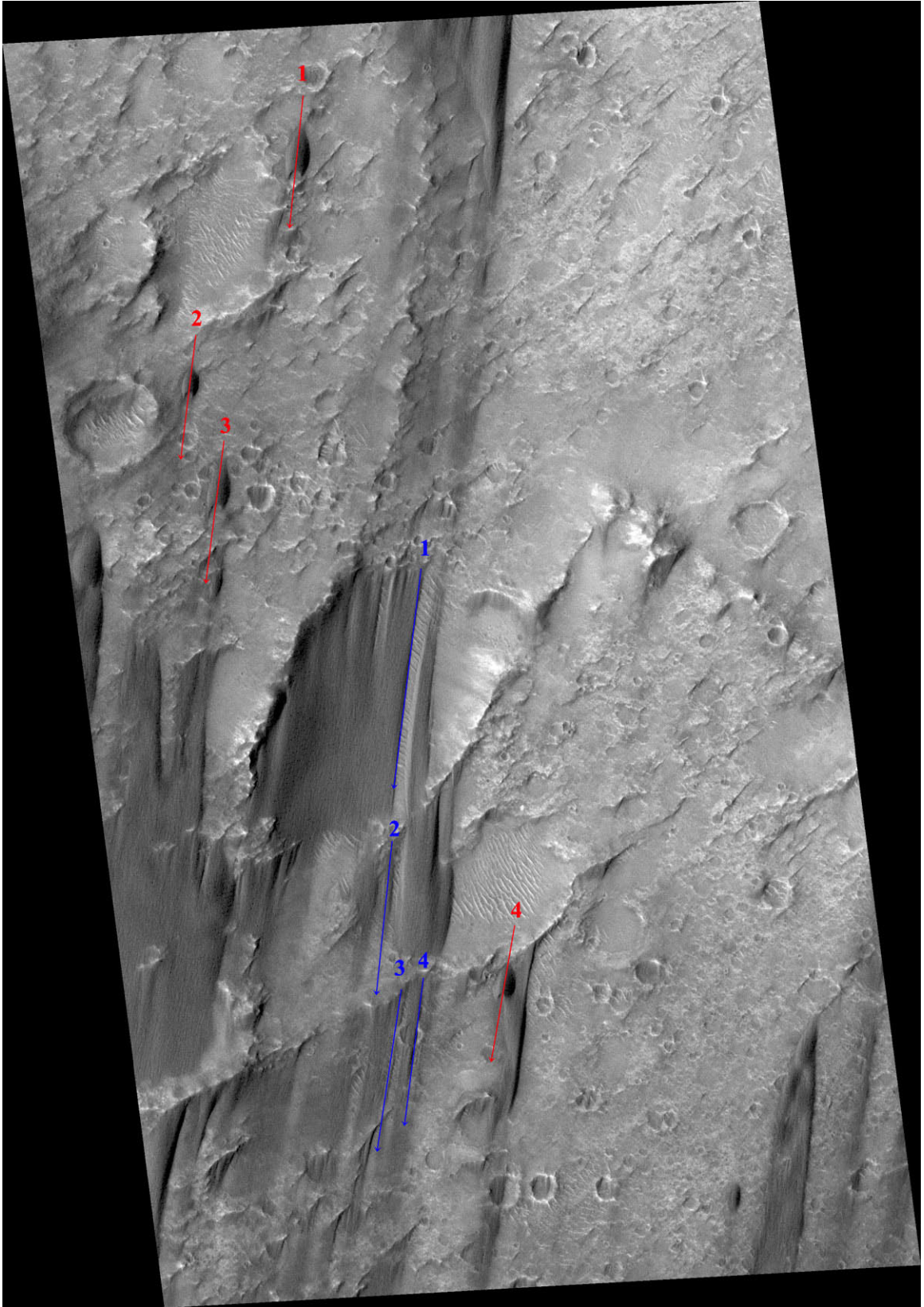


Figure C-31. MSSS MOC NA image R0500941 annotated

VITA

Christopher T. Adcock

Candidate for the Degree of Master of Science

Thesis: Determining Formative Winds Through Geomorphology: Herschel Crater, Mars.

Major Field: Geology

Education

B. S., Earth and Planetary Sciences, University of New Mexico, Albuquerque, 1995

Graduate course work in Planetary Sciences, University of New Mexico, Albuquerque, 1996-97

Completed the requirements for the degree of Master of Science in Geology at Oklahoma State University, Stillwater, December 2004

Advisor: Dr. Richard Marston

Grants, Honors, and Awards

OSU

Rumsey Bissell Marston Scholarship, 2004

Oklahoma Space Grant Consortium NASA Fellowship, 2004

Invited Attendee of the NASA/JPL Planetary Science Summer School, 2004

Departmental Outstanding Teaching Award, 2003-2004

Member of the Phi Kappa Phi Honors Society, 2004

Graduate member of the Sigma Gamma Epsilon Honorary Society, 2003-2004

UNM

Recipient of the Harry and Mabel Leonard Scholarship, 1994

Recipient of the General Thomas Campell Award, 1993

Work Experience

Sandia National Laboratories, Senior Technician, 1/01 through 8/02 (Contracted to SNL by OnSite Engineering)

Responsibilities: Electron / Optical Microscopy, Data management, Data Server administration. Electron Microprobe development and operations documentation.

Isonics Corporation (formerly CMRI), Senior Research Technician, 6/00-1/01

Responsibilities: Development of chlorine handling systems and high purity metal extraction methods. Focused on the recovery of zinc and other metals from waste products.

Colorado Mineral Research Institute (CMRI), Metallurgical Laboratory Research

Technician, 6/99-5/00 (Contracted to CMRI by GeoTemps)

Responsibilities: Pilot plant operation, research and development of solvent extraction techniques, as well as research of in situ extraction of subterranean mineral bodies, and experimental design.

University of New Mexico Institute of Meteoritics, Physical Sciences Research Technician,

5/93-4/99

Responsibilities: Operation, maintenance, new user training and upgrade of Scanning Electron Microscope (SEM), Electron Microprobe (EMP), and numerous peripheral analytical equipment. Selected research activities included NASA's ongoing Microbeam Studies of Planetary Materials project. Research focus on meteorites and glasses in Apollo Mission lunar samples, requiring the development of an automated modal/seek-find-quantify software package for both the SEM and EMP.

University of New Mexico, Research Assistant for Y. Asmerom Ph.D, 4/95-11/95

Responsibilities: Preparing volcanic basalts for geochemical analysis

Other Training and Computer Experience

Radiation Safety Training from University of New Mexico Occupational Safety / Radiation Safety.

Software Experience includes HTML, Telnet, Gopher, Veronica/Archie, FTP, most Adobe products, most Macromedia products, ImagePro (Image Analysis Suite), MS/PC DOS, MS Windows (all versions), Mac OS (all versions), Tracor/Northern/Noran and Oxford EDS systems, Oxford Genie & Lemas, as well as ISIS, JEOL JXA interface MS Office applications (Word, Excel, etc.), PFS Softkey/IBM WinWorks, WordPerfect, Grapher, and numerous DOS/Windows scientific and general applications.

Programming Experience includes FORTRAN, BASIC, JAVA Scripting, Python and some Visual Basic.